2022

Microwave Enhanced Electron Energy Distribution Functions

John Samuel McKee
West Virginia University, jsmckee@gmail.com

Microwave Enhanced Electron Energy Distribution Functions

John S. McKee

Dissertation submitted to the Eberly College of Arts and Sciences
at West Virginia University
In partial fulfillment of the requirements for the degree of

Doctor of Philosophy
in
Physics

Earl E. Scime, Ph.D., Chair
Paul Cassak, Ph.D.
Weichao Tu, Ph.D.
William Amatucci, Ph.D.
Amy M. Keesee, Ph.D.

Department of Physics and Astronomy

Morgantown, West Virginia
2022

Keywords: electron heating, wave damping, helicon plasma

Abstract

Microwave Enhanced Electron Energy Distribution Functions

John S. McKee

The use of two (or more) radio frequency (RF) sources at different frequencies is a common technique in the plasma processing industry to control ion energy characteristics separately from plasma generation. A similar approach is presented here with the focus on modifying the electron population in argon and helium plasmas. The plasma is generated by a helicon source at a frequency $f_0 = 13.56$ MHz. Microwaves of frequency $f_1 = 2.45$ GHz are then injected into the helicon source chamber perpendicular to the background magnetic field. The microwaves damp on the electrons via R-mode (anti-parallel to the background magnetic field B_0) and X-mode (perpendicular to B_0) Electron Cyclotron Resonance (ECR) heating, providing additional energy input into the electrons. The effects of this secondary-source heating on electron density, temperature, and energy distribution function are examined and compared to helicon-only single source plasmas as well as numerical models suggesting that the heating is not evenly distributed but spatially localized. Optical Emission Spectroscopy (OES) is used to examine the impact of the energetic tail of the electron distribution on ion and neutral species via collisional excitation. Large enhancements of neutral spectral lines are observed with little to no enhancement of ion lines via X-mode ECR heating while R-mode damping shows significant enhancement of ion line emission.

Acknowledgements

How can I possibly thank everyone I know?
The greatest gift Physics has given me are incredible friends that will be part of my life far beyond classrooms and laboratories.

From my hometown – You've kept me humble. Maybe too humble. Maybe ease up on the humble-keeping.

From Ed's lab and Auburn – War Eagle, buddies!

From Earl's lab and Morgantown – Thanks for helping me make a home away from home.

For my advisors Earl Scime and Ed Thomas – You have been so much more than advisors. You've taught me not only what kind of scientist I want to be but what kind of man I want to be.

Thank you everyone. If it weren't for you, I wouldn't have done this.

Contents

List of Figures

List of Tables

Abbreviations

ADAS	Atomic Data and Analysis Structure
CA	Conventional Langmuir Analysis
CCD	Charge-Coupled Device
CHEWIE	Compact HElicon for Waves and Instabilities Experiment
CL	Child-Langmuir Floating Point Analysis
CR	Collisional-Radiative Model
ECR	Electron Cyclotron Resonance
EEDF	Electron Energy Distribution Function
EEPF	Electron Energy Probability Function
EVDF	Electron Velocity Distribution Function
IVDF	Ion Velocity Distribution Function
LIF	Laser Induced Fluorescence
LTE	Local Thermodynamic Equilibrium
OES	Optical Emission Spectroscopy
OML	Orbital Motion Limited Theory
RF	Radio Frequency
TALIF	Two-photon Absorption Laser-Induced Fluorescence

Dedicated to my parents

You've given me unending love and support usually only seen in Norman Rockwell paintings and 80's sitcoms.

You encouraged every dream I wanted to follow.

You were there for every leap I've taken to catch me when I fell and swell with pride when I flew.

I am grateful beyond words.

Chapter 1

Introduction

Manipulation and control of the particle energy distribution is an effective way of affecting chemical processes and the population of excited electronic states of neutrals and ions in a plasma. One example of chemical process control was a series of atmospheric pressure dielectric barrier discharge experiments performed at West Virginia University in which a resonant driving frequency was used in combination with electrodes coated with a catalyst to shift the electron energy distribution out of local thermodynamic equilibrium (LTE) and enhance the disassociation of carbon dioxide into free carbon and carbon monoxide by as much as 20%.[1] In industrial plasmas, dual-frequency capacitively coupled and inductively coupled plasmas are a common method of separately controlling the plasma density and the ion energy distribution to optimize and improve dry etch processing.[2–7] In fusion plasmas, Electron Cyclotron Resonance (ECR) heating is often used to drive current by enhancing a portion of the high energy tail of the electron velocity distribution through wave-particle interactions.[8]

In this work, the high-energy portion of the electron energy distribution function (EEDF) of a helicon plasma is enhanced by ECR via the injection of R- and X-waves from a microwave source for the targeted enhancement of specific excited electronic states. The R-wave is an

electromagnetic wave that propagates parallel to the local magnetic field, is right-circularly polarized, and has a resonance (is absorbed) at the electron cyclotron frequency, $\omega_{ce} = eB/m_e$, the frequency at which electrons gyrate around a magnetic field. B is the magnetic field strength and m_e is the electron mass. The X-wave propagates perpendicular to the magnetic field and for heavy ions it has a resonance at $\omega \approx \omega_h = \sqrt{\omega_{ce}^2 + \omega_{pe}^2}$. $\omega_{pe}^2 = 4\pi n_e e^2/m_e$ is the electron plasma frequency, n_e is the electron density, and e is the electric charge. These excited electronic states are of interest because they are necessary for the use of diagnostic techniques for ions and neutrals that rely on the absorption or emission of line radiation, e.g., laser-induced fluorescence (LIF) and two-photon laser-induced fluorescence (TALIF).

The plasmas used in this study are created in a helicon plasma source. Helicon discharges are magnetized radio frequency (RF) discharges sustained by launching a $\approx$ 10 MHz electromagnetic wave from an antenna wrapped around the outside of a dielectric (typically glass) tube. While helicons have been studied both theoretically and experimentally since the 1960s, they have become popular plasma sources since the work of Boswell in the 1980s.[9] Helicons characteristically produce high density ($n_e \approx 10^{11}$ to 10^{14} cm^3), low temperature ($T_e \leq 10$ eV, $T_i \leq 1$ eV) plasmas with a few hundred watts of RF power and with a few hundred Gauss axial magnetic field.[10] In recent years, considerable evidence has emerged that plasma production and particle heating (both electron and ion) are dependent on the strong absorption of slow mode waves at the plasma edge.[11–14] The density and temperature range of helicon plasmas are well suited to measurements of the ion velocity distribution function (IVDF) by LIF and the neutral velocity distribution function by TALIF. LIF and TALIF employ a laser tuned to a specific atomic or molecular transition to pump electrons to higher energy states. Fluorescent emission arising from the relaxation of the excited state is then measured by a photodetector.

During an LIF or TALIF measurement, the fluorescent emission as a function of the

wavelength of a narrow linewidth tunable laser provides a direct measure of the velocity distribution function of an electronic state of the target species. Typically, the electronic state selected is metastable to optimize the signal-to-noise ratio of the measurement. The quality of the measured signal depends on the plasma density, electron temperature, and background neutral density (through the effects of collisional quenching of the target state by neutrals). While LIF and TALIF techniques have been demonstrated in low temperature plasmas for hydrogen, deuterium, oxygen, nitrogen, xenon, and krypton neutrals, and argon and xenon ions, no LIF technique has been successfully demonstrated for helium ions. Diagnosing helium flow velocities and ion temperatures in plasmas would contribute significantly to our understanding of plasma dynamos,[15] plasma boundaries,[16] magnetic reconnection,[17] and Alfvén waves.[18] The main difficulties are helium's relatively high ionization energy of 24.58 eV and the 40.8 eV energy difference between the lowest level ion metastable state (the $2s$ state) and the helium ion ground state. These factors result in helium ion metastable populations that are too small to diagnose by LIF for most experiments and applications.[19]

Demonstrating helium LIF or TALIF in a helicon source is particularly difficult given helium's relatively high ionization energy of 24.58 eV and the 40.8 eV energy difference between the lowest level ion metastable state (the 2S state) and the helium ion ground state. The typical electron temperature in a helicon source, a few eV, is too small to sufficiently populate such energetic states so that LIF or TALIF on helium ions is feasible. The ultimate goal of this work is to demonstrate that is possible to modify the EEDF in a helium helicon plasma such that the enhanced high-energy electron population is sufficient to excite helium ions from the ground state to the 2S metastable state at levels that make it possible to perform TALIF measurements of the helium IVDF.

This dissertation begins with a review of the experimental facility and the diagnostic methods in Chapters 2 and 3, respectively. The effects of R-Wave injection on helium and

argon EEDFs in a helicon source are examined in Chapter 4. The effects of X-Wave injection on helium and argon EEDFs in a helicon source are examined in Chapter 5. A discussion of the results and suggestions for future work are presented in Chapter 6.

Chapter 2

Experimental Apparatus

The Compact HElicon for Waves and Instabilities Experiment (CHEWIE) is, as its name suggests, a relatively small helicon plasma source which serves as a test bed for diagnostic development. Unlike most other linear helicon devices,[9,11,20] CHEWIE is oriented vertically with the plasma source above an expansion chamber. CHEWIE has been used for studies of nitrogen ion production,[16] neutral depletion in krypton,[21] and neutral hydrogen density profiles.[22]

2.1 CHEWIE Chamber

The CHEWIE source produces plasma in a 61 cm long Pyrex^{TM} tube with inner diameter of 5 cm and outer diameter of 6 cm. The top of the tube is capped with a 6 inch stainless steel flange to which a 2 3/4 inch Conflat^{TM} window is attached. A hole was drilled in the side of the 6 inch flange to accommodate a gas feed through which the Ar or He gas enters the chamber. The bottom of the tube is mated to one of two expansion chambers, depending on the type of electromagnetic wave being injected into the system for electron heating.

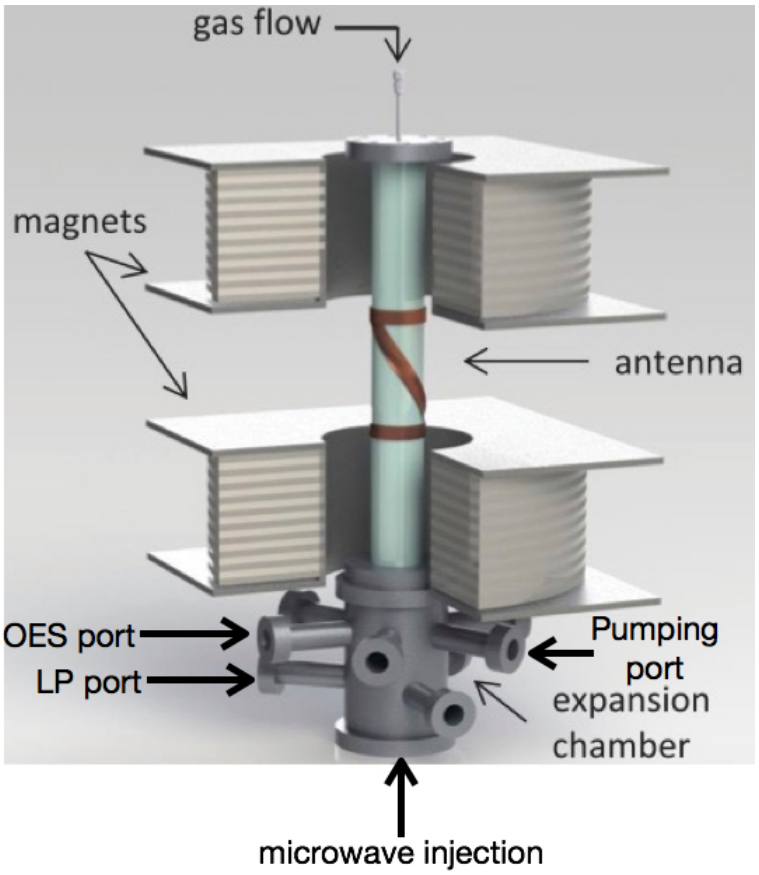

FIGURE 2.1: Schematic of CHEWIE with R-Wave injection chamber.

2.1.1 R-Wave Injection Chamber

The expansion chamber used for coupling R-waves into the plasma, shown in figure 2.1, is a 20 cm long, 16 cm diameter stainless steel cylinder custom made by Kurt J Lesker Co. for this experiment. Diagnostic access is provided by nine 2 3/4 inch Conflat^{TM} ports; six located 4 cm axially from the top of the chamber and another three 6 cm farther down. Two of the ports were used for pressure gauges and connection to the vacuum pump. Microwaves were injected through the bottom port of the chamber as R-waves require the wave vector, $\mathbf{k}$, be parallel (or in this case, anti-parallel) to the background magnetic field, $\boldsymbol{B_0}$.

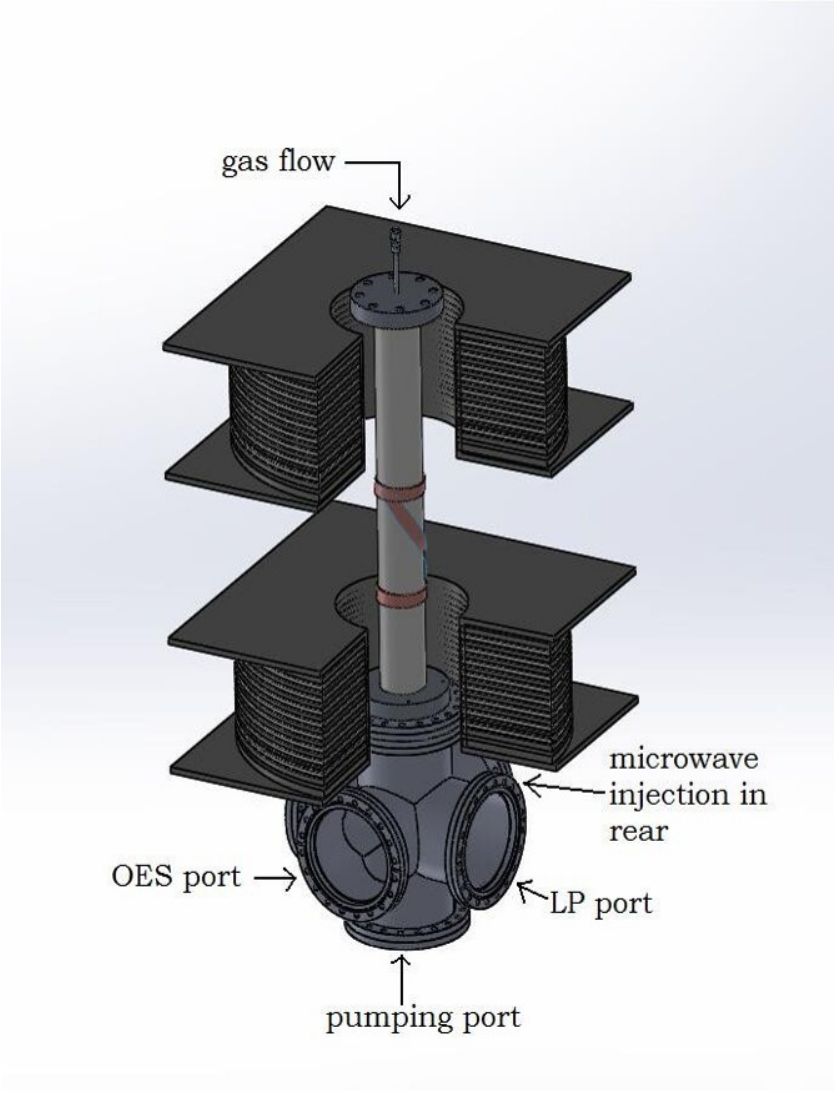

FIGURE 2.2: Schematic of CHEWIE with X-Wave injection chamber.

2.1.2 X-Wave Injection Chamber

The expansion chamber for coupling X-waves to the plasma, shown in figure 2.2, was a stock stainless steel 6-Way cross of 8 inch Conflat^{TM} ports, also from Kurt J Lesker Co., fitted with 8 inch-to-2 3/4 inch zero length reducer flanges. Diagnostic access was through two of the 2 3/4 inch reduced openings along the middle four flanges. The bottom chamber port connected to the vacuum pump through a reducing tee to which pressure gauges were attached. Microwaves were injected through a middle 8 inch port in the rear of the chamber as X-waves require the

wave vector, $\mathbf{k}$, and the electric field vector, $\mathbf{E}$, be perpendicular to the background magnetic field, $\boldsymbol{B_0}$.

2.2 Vacuum System

The typical base pressure of 10^{-7} Torr in the chamber was obtained with a Pfeiffer Vacuum TSH 521 turbomolecular drag pump backed with a MD4 diaphragm pump. Whether attached at a side port or directly to the bottom of the chamber, vibrations from the vacuum system were decoupled from the rest of the experiment with the use of a flexible bellows. A pneumatically operated gate valve, interlocked with a KJL 4500 Ion Gauge Controller, isolated the turbomolecular drag pump from the rest of the vacuum system in case of a sudden large increases in pressure. Neutral gas flow to the experiment was controlled with a MKS 1179A mass flow controller with a MKS PR4000 power supply. Typical flow rates were between 20-40 SCCM. Total gas pressure was measured with a species-independent MKS Type 626 Baratron Pressure Transducer and a MKS Type 660 power supply for values above 1 mTorr. Pressures below 1 mTorr were measured with a Granville-Phillips Series 274 Tubulated, dual tungsten filament type Ion Gauge and SRS IGC100 Controller. Typical fill pressures for these experiments were 7 mTorr for argon and 20 mTorr for helium.

2.3 Magnetic Field

Background axial magnetic fields for all experiments were created with two water cooled electromagnets constructed at West Virginia University. These are made of 1/2" square aluminum tubing wound into seven "pancake" coils, each ten turns thick and two layers wide. The seven pancake coils are stacked into a single electromagnet. Each electromagnet has dimensions of

21.6 cm high, an outer radius of 24.2 cm, and an inner radius of 9.5 cm. Current to the coils is supplied in series with an Ametek Sorensen power supply capable of producing 395 Amps at 25 Volts. 395 Amps of current produces a magnetic field strength of 1500 Gauss in the center of each solenoid and 1200 Gauss in the source region between the two electromagnets. A plot of the magnetic field versus applied current in the source region is shown in Figure 2.3. Similar plots for the port locations in the two expansion chambers, where these experiments were performed, are shown in Figure 2.4, Figure 2.5, and Figure 2.6.

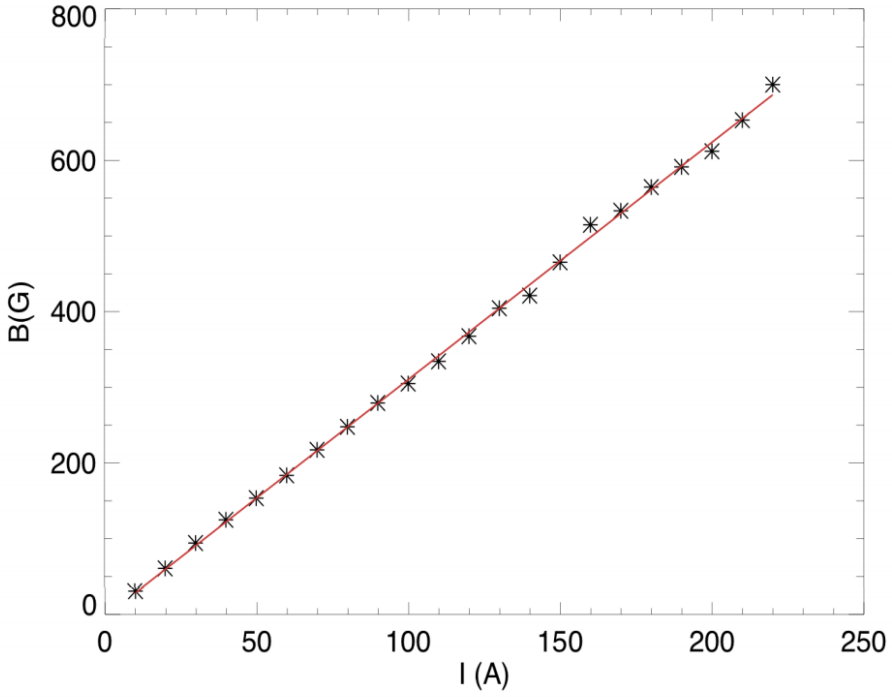

FIGURE 2.3: Magnetic field strength versus coil current in the CHEWIE source region. The slope of the linear fit is 3.14 G/A. Fig. from Ref. [23].

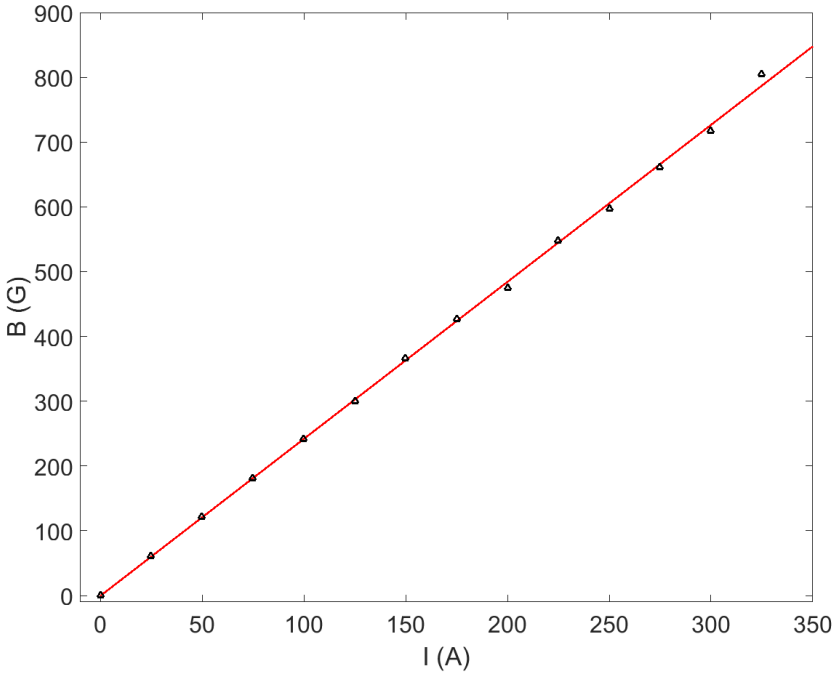

FIGURE 2.4: Magnetic field strength versus coil current for the upper tier of ports in the expansion chamber used for R-Wave injection. The slope of the linear fit is 2.42 G/A.

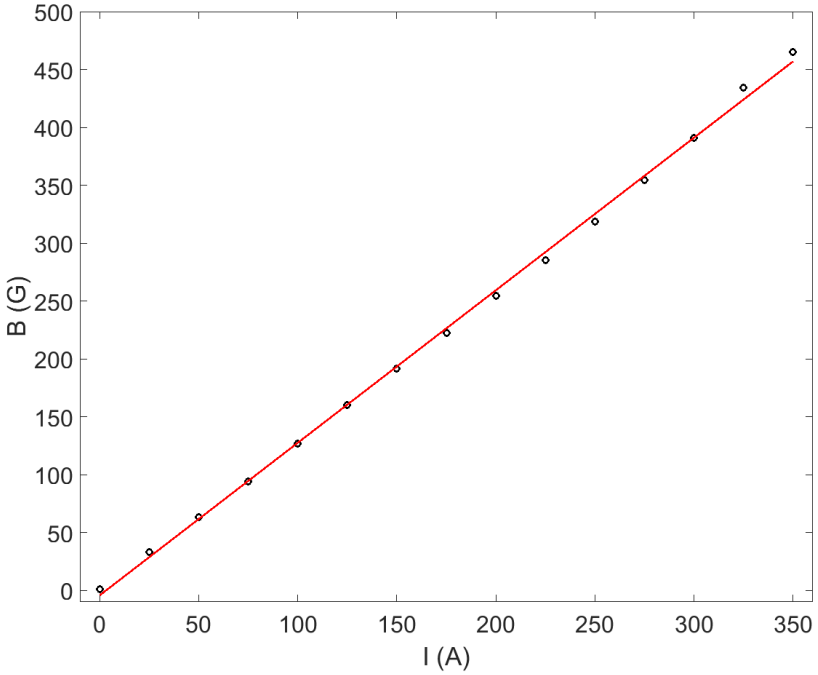

FIGURE 2.5: Magnetic field strength versus coil current for the lower tier of ports in the expansion chamber used for R-Wave injection. The slope of the linear fit is 1.32 G/A.

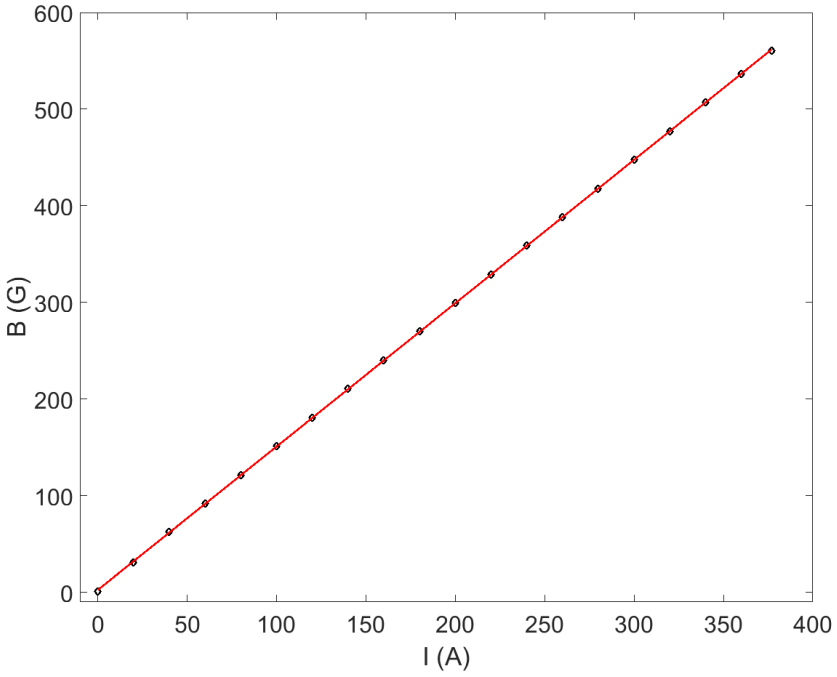

FIGURE 2.6: Magnetic field strength versus coil current in the expansion chamber used for X-Wave injection. The slope of the linear fit is 1.48 G/A.

2.4 RF Antenna and Matching Network

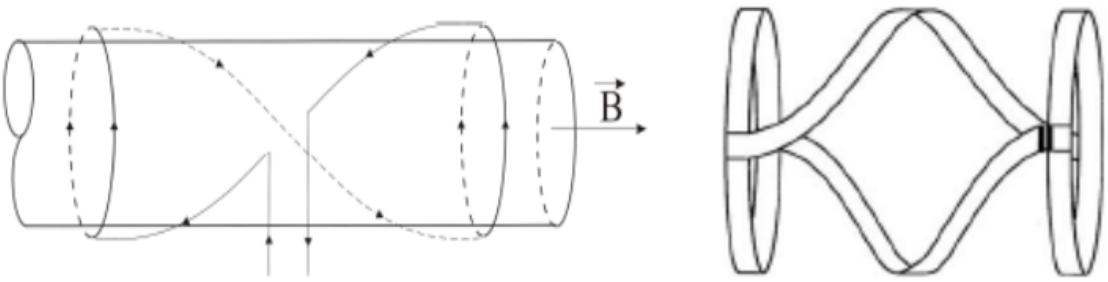

FIGURE 2.7: Diagram of the $m = +1$ helical antenna and sketch of the actual antenna. Fig. from Ref. [24].

RF power is supplied to the plasma by a Dressler Cesar Model 1350 RF power supply capable of producing 5 kW of power at a frequency of 13.56 MHz. Power is coupled into the plasma with an 18 cm long, $m = +1$, right-handed helical antenna as shown in Figure 2.7. Effective and efficient coupling of power to the plasma requires matching the real part of the impedance

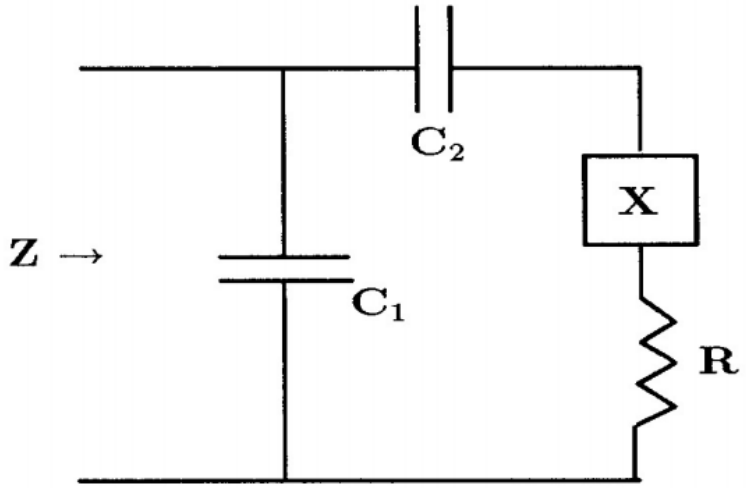

FIGURE 2.8: Matching circuit for the helicon antenna for CHEWIE. C_1 is the load capacitor and C_1 is the tuning capacitor. R and X represent the real and imaginary parts of the plasma impedance, respectively. Fig. adapted from Ref. [25].

of the antenna/plasma to the output impedance of the RF power supply and transmission line connecting the RF power supply to the antenna. At the same time, the imaginary part of the impedance for the circuit is ideally zero to eliminate reflected power back to the RF power supply[25]. To achieve these conditions, a π-type matching network was installed between the RF power supply and the antenna. The matching network consisted two Jennings high-voltage vacuum capacitors with tuning ranges of 20-2000 pF. One capacitor was placed in series with the antenna/plasma for tuning while the other was placed in parallel with all three for load adjustment. A diagram of the matching circuit is shown in Figure 2.8, where C_1 is the load capacitor and C_2 is the tuning capacitor. *Chen*[25] calculated the required load (C_1) and tuning (C_2) capacitances for an inductive load to be matched to the 50 Ω real output impedance of the RF power supply while simultaneously minimizing the imaginary part of the circuit impedance:

$$C_L = \frac{1}{2\omega R}\left[1 - \left(1 - \frac{2R}{R_0}\right)^2\right]^{\frac{1}{2}} \tag{2.1}$$

and

$$C_T = \left[\omega X - \frac{1 - \frac{R}{R_0}}{C_L}\right]^{-1}, \tag{2.2}$$

where R is the real resistance of the antenna, $R_0 = \sqrt{L/C}$ is the normalized impedance, and $X = \omega L$ is the reactive impedance of the antenna.

After the discharge is initiated, the effect of the inductive load of the plasma on the antenna must be considered. For a typical helicon plasma source in the "inductive" or "helicon" mode, Eq. 2.2 becomes

$$C_T^{-1} = \omega^2 L - \frac{\left(1 - \frac{R}{R_0}\right)}{C_L} \tag{2.3}$$

where L is the total inductance in the antenna portion of the circuit. For CHEWIE plasma source conditions, the required values of C_L and C_T fall in the range of 20-2000 pF. Therefore, during operation at RF powers of 150 to 750 W for helium and argon plasmas, it was possible to tune the matching network so that less than 3 W of power was reflected back to the RF power supply.

2.5 Microwave Injection

Microwaves were injected into CHEWIEs expansion chambers through a vacuum sealed quartz window via WR340 waveguide, which allows only the TE10 wave mode to propagate.[26] The magnetron, high-voltage transformer, and control board were taken from a Panasonic NN-SN651B household microwave oven. The magnetron produced 1.2 kW of power at 2.45 GHz in 6.4 ms pulses at 120 Hz (70% duty cycle). Impedance matching the open-air waveguide to the plasma was done through a two-stub tuner. However, two-stub tuners cannot match every load impedance,[27] which led to inefficient coupling. Reflected microwave power was isolated from the magnetron with a circulator and the excess microwave power dumped to a water cooled

dummy load, as shown in Fig 2.9 and 2.10. A fraction of the diverted reflected power was sent to a crystal diode, which converted it to a DC voltage for a measurement of the total reflected power. The diode was incapable of measuring reflected power levels in excess of 1 kW.

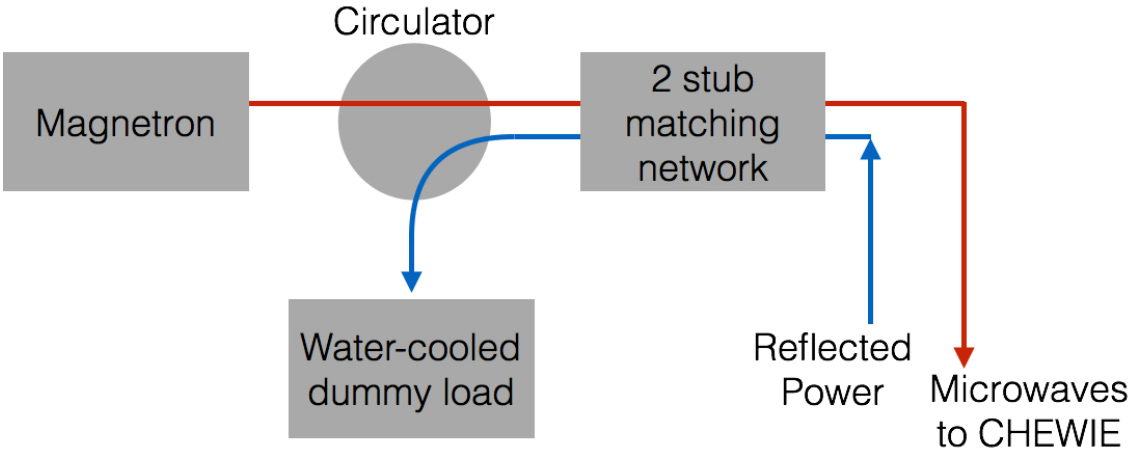

FIGURE 2.9: Diagram of the microwave injection apparatus used on CHEWIE. The 2.45 GHz magnetron provided 1.2 kW of power which was coupled into the WR340 waveguide for injection into the vacuum chamber. The waveguide-to-vacuum interface was through a vacuum sealed quartz window.

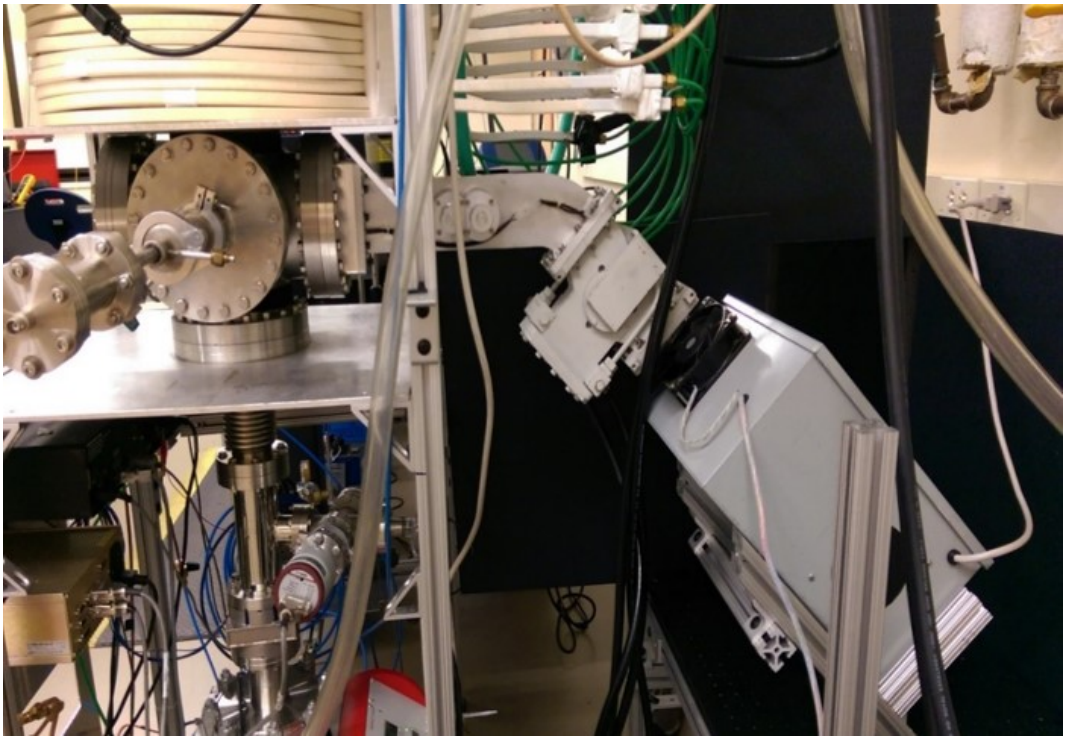

FIGURE 2.10: Photo of the microwave injection apparatus on CHEWIE. The large gray box to the far right is a RF shielded and grounded box that isolated microwave emission from the rest of the laboratory. The magnetron is inside the shielding box. Attached to the box is the circulator with the water-cooled dummy load. Following the circulator is the two-stub waveguide tuner.

2.6 Common Plasma Parameters

TABLE 2.1: Common plasma parameter values in CHEWIE

Quantity (units)	**Symbol**	**Value**
Magnetic field (Gauss)	B	700-1200 (source region)
Fill pressure (mTorr)	P	7 (Ar) 20 (He)
Density (cm^{-3})	n	10^{10} - 10^{12}
Ion temperature (eV)	T_i	$\sim$ 0.2
Electron temperature (eV)	T_e	1 - 8
Debye length for $T_e = 8$ eV (cm)	λ_D	10^{-2}
Ion gyroradius for $B = 1200$ G (cm)	ρ_i	0.24 (Ar) 0.08 (He)
Electron gyroradius for $T_e = 8$ eV (cm)	ρ_e	10^{-3}
Ion plasma frequency (rad/s)	ω_{pi}	10^8 (Ar) 10^8 (He)
Electron plasma frequency (rad/s)	ω_{pe}	10^{10}
Ion gyrofrequency (rad/s)	ω_{ci}	10^5 (Ar) 10^6 (He)
Electron gyrofrequency (rad/s)	ω_{ce}	10^9

Chapter 3

Diagnostic Methods

The principal diagnostics used in this work are a Langmuir probe and passive optical emission spectroscopy (OES).

3.1 Langmuir Probe

At its simplest, a Langmuir probe is just a conducting wire placed in the plasma. It is biased to a voltage and the current collected is recorded. However, the simplicity of the probe design and operation belies the need for careful and complex analytic techniques for all but the most basic plasma conditions. Langmuir probes are among the oldest plasma diagnostics, having been introduced by Langmuir and Mott-Smith in the mid-1920's.[28] They provide measures of the bulk quantities n_i, n_e and T_e, the ion density, electron density, and electron temperature respectively, as well as the EEDF and EEPF, the electron energy distribution function and the electron energy probability function. Despite the extensive and long-standing use of Langmuir probes, no complete probe theory exists. For decades, probe theory focused on quiescent, unmagnetized, low temperature plasmas. More recently, Langmuir probe theory has been extended

to more complex plasma regimes, such as in magnetized,[27,29–32] radio-frequency,[33,34] and high temperature plasmas.[32,35,36] Basic probe theory is covered in several excellent and instructional reviews.[24,34,37–40] Probe fabrication and analysis techniques remain an active area of research.

A plot of the collected current from a Langmuir probe, I, versus the probe potential bias, V is a characteristic graph called an *I-V characteristic* or, more commonly, an *I-V trace*. An example of such a trace is given in Figure 3.1. There are two important potentials that divide the I-V trace into three regions: the floating potential, ϕ_f, and the plasma potential, ϕ_p. The floating potential is the bias voltage at which the probe collects equal currents of electrons and ions, resulting in zero net current. The plasma potential is the electrostatic potential of the plasma relative to the grounded chamber walls. Both potentials are located near inflection points in the I-V trace (the floating potential is easily identified by the bias potential corresponding to zero net collected current). The three sections of the I-V trace separated by the two potentials are the *ion saturation region*, the *electron saturation region*, and the *transition region*.

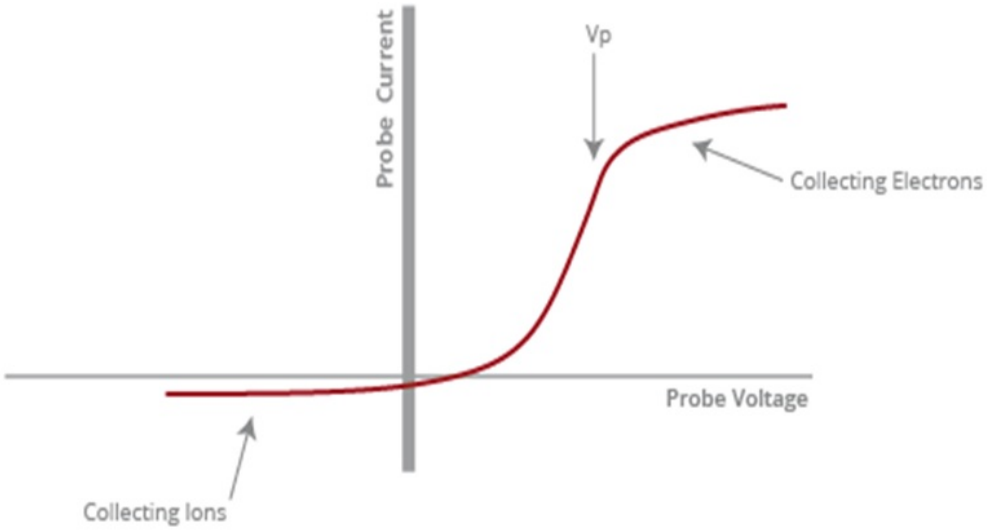

FIGURE 3.1: Idealized collected current versus applied bias obtained with a Langmuir probe. At large positive bias voltages, the collected electron current saturates. At large negative biases, the collected ion current saturates. The region between the two saturation regions includes the plasma and floating potential.

The ion saturation region occurs where $V < \phi_f$ and $V \ll \phi_p$, or the left-most region of the I-V trace. Here, ions are attracted to the probe while electrons are almost completely repelled save for those with energies large enough to overcome the bias barrier. The term "ion saturation" comes from ideal conditions in which, no matter how negatively the probe is biased, it does not collect any more current beyond a certain value. However, the term is applied to the region whether true saturation is reached or not (sheath expansion or other effects often prevent perfect saturation). The electron saturation region occurs where $V \gg \phi_f$ and $V > \phi_p$, or the right-most region of the I-V trace. Like the ion saturation region, here electrons are attracted to the probe while ions are repelled. It is again named for the ideal case where the collected current cannot increase past a certain value regardless of how positively the probe is biased. The geometry of the probe construction plays a major part in the current behavior in this region. While a planar probe may reach electron saturation, cylindrical and spherical probes cannot. The transition region is where $V > \phi_f$ and $V < \phi_p$, or the central region of the I-V trace. In the transition region, the probe is still collecting ions and repelling some electrons. However, due to the relatively small bias voltage and the greater energy and mobility of the electrons, both plasma species are collected. If the electrons are Maxwellian, the current in this region increases exponentially with increasing positive bias V.

3.1.1 Probe Design and Construction

A schematic drawing of the Langmuir probe used in these experiments is shown in Fig 3.2. The probe tip is a 0.5 mm diameter tungsten rod inserted into a 0.6 mm inner diameter alumina shaft and attached by a set screw to a copper base. A 10 nF capacitor is also connected to the copper base. This assembly is placed inside a boron nitride (BN) cap such that the probe tip extends into the plasma through a hole in the BN cap, while the opposite leg of the capacitor remains within the BN head so that it is not directly exposed to the plasma. The threaded BN cap

attaches to the stainless steel probe shaft. An RF choke chain is attached to the copper base. The RF chokes are 0.25 Watt, shielded, resonant, inductors from Lenox-Fugle International, Inc.; each designed to block a particular range of frequencies.

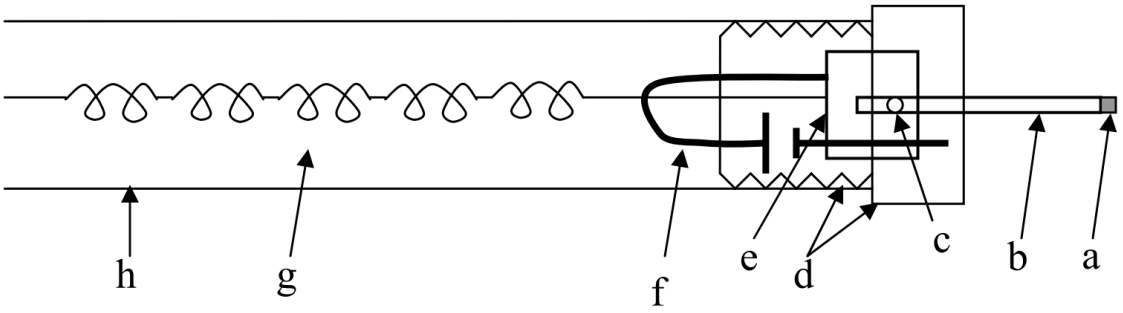

FIGURE 3.2: Schematic drawing of the Langmuir probe design including a) tungsten probe tip, b) alumina shaft, c) set screw, d) threaded boron nitride cap, e) copper base, f) capacitor, g) chain of RF chokes and h) stainless steel probe shaft. Figure obtained from Ref. [29].

Starting from the copper base, the RF chokes are placed in the sequence: 26, 53, 26, 13.2 and 6.8 MHz. The end of the RF chokes is then soldered to a shielded, coaxial probe wire that is attached to the BNC vacuum feedthrough at the far end of the probe shaft. Thermaflex tubing is used to cover the chain of RF chokes. Fig 3.3 is a photograph of the Langmuir probe head used in these experiments. Note that the majority of the probe tip is less than 1 mm in diameter and thus plasma perturbation is minimized.

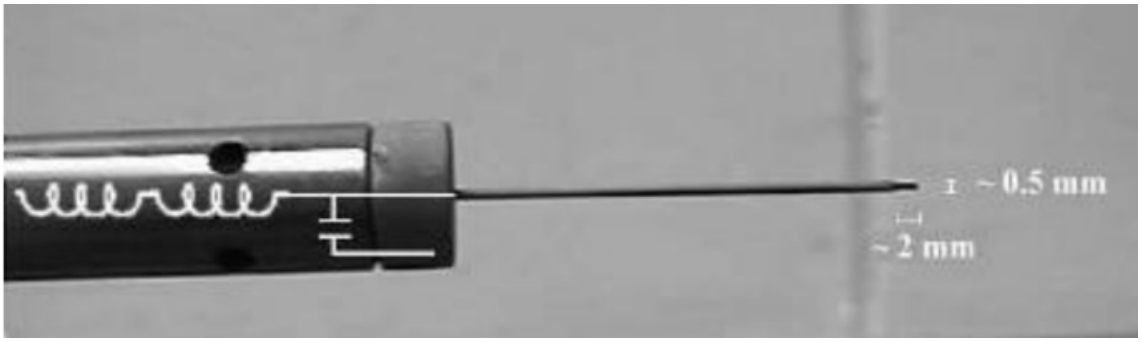

FIGURE 3.3: Photograph of the Langmuir probe head assembly used in these experiments.

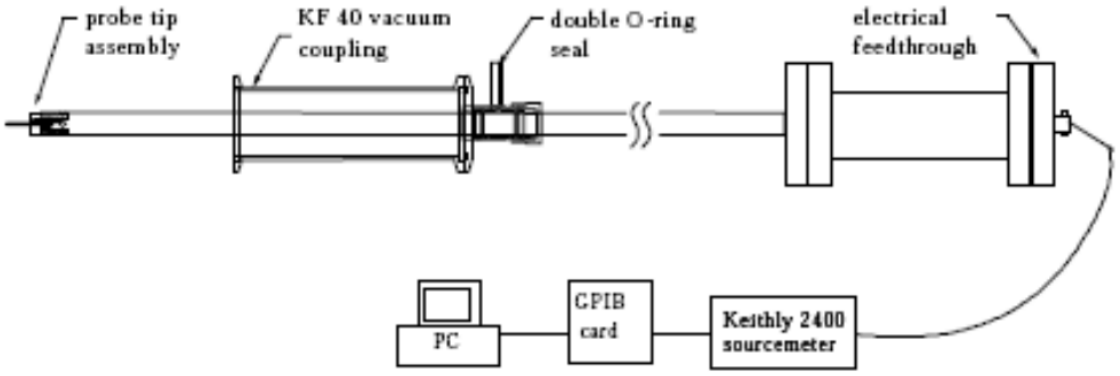

FIGURE 3.4: Schematic of the Langmuir probe measurement circuit. Figure obtained from Ref. [30].

A high-impedance Keithley 2400 SourceMeter is used to measure the Langmuir probe I-V trace. The source meter applies the bias voltage to the probe, as well as measures the collected current. The source meter is controlled via a GPIB interface by custom software created in LabWindows^{TM}. A schematic of the Langmuir probe measurement circuit is shown in Fig 3.4.

3.1.2 Langmuir Probe Analysis

From an *I-V* trace it is, ideally, possible to calculate the plasma quantities ion density, n_i, electron density, n_e, ion temperature, T_i, and electron temperature, T_e, from the characteristic values ϕ_f, ϕ_p, the ion saturation current, I_i^{sat}, and the electron saturation current, I_e^{sat}. However, things are often far from ideal. The calculation of n_e requires a measurement of I_e^{sat}, which is not possible given the cylindrical probe geometry used in these experiments. T_i is also hard to obtain accurately due to the difficulty in separating ion and electron contributions to the total current in the electron saturation region. For these reasons, the measured quantities from the Langmuir probe are limited to T_e and n_i, which through quasi-neutrality is assumed to be equal to n_e.

The first, and perhaps most important, step in analyzing an *I-V* trace is separating the contributions of ions and electrons to the current in the ion saturation region, such that

$I = I_e + I_i$. Facilitating such a separation requires models for I_e and I_i. The electron contribution is given as

$$I_e(V) = I_p \exp\left[-q(\phi_p - V)/k_B T_e\right] \tag{3.1}$$

where q is the elementary charge, k_B is Boltzmann's constant, and I_p is the electron current at the plasma potential. Thus,

$$T_e = \frac{k_B}{q}\left[\frac{d \ln I_e(V)}{dV}\right]^{-1}. \tag{3.2}$$

That is, T_e is the inverse slope of the semilog plot of $I_e = I - I_i$ in the ion saturation and transition regions.[41] Determining I_i, and thus n_i, is more difficult. The rest of this section provides brief overviews of three different methods for determining n_i.

3.1.2.1 Conventional Langmuir Analysis (CA)

The conventional analysis approach developed Langmuir and Mott-Smith[28] assumes that the electrons in the bulk plasma far away from the probe are isotropic and that the charged particles in the plasma approach the probe surface along radial trajectories with Maxwellian energy distributions. Following the derivations of *Chen*[42] and *Hershkowitz*[41], the current I_σ is the particle flux to the probe surface such that $J_\sigma = n_\sigma e v_\sigma = I_\sigma / A_p$, where J_σ is the current density at the probe surface, n_σ is the charged particle density, $A_p = \pi r_p^2 + 2\pi r_p l_p$ is the exposed area of the cylindrical probe, with r_p and l_p being the probe radius and exposed length, respectively, v_σ is the velocity of the incident particles, and σ denotes the particle species, either electron or ion. If the total particle fluxes are constant in the saturation regions, the electrons reach the probe at their thermal velocity, $v_{th} = \sqrt{8T_e/\pi m_e}$, and the ions at the Bohm velocity, $v_{Bi} = \sqrt{k_B T_e / m_i}$, with m_i and m_e being the ion and electron masses. The saturation current is related to the plasma parameters through

$$I_i^{sat} = \alpha n_i q A_p \left(\frac{k_B T_e}{m_i} \right)^{1/2} \tag{3.3}$$

where α is a multiplicative factor that accounts for the difference in the ion density measured at the probe surface and the ion density in the plasma bulk far from the perturbation region around the probe. α depends on the geometry of the probe and the local Debye length λ_D via the empirical relation [100]:

$$\alpha = 0.607 + 2432/\exp[7.01(r_p/\lambda_D)^{0.096}] \tag{3.4}$$

where

$$\lambda_D = \sqrt{\frac{\epsilon_0 k_B/q^2}{n_e/T_e + n_i/T_i}} \tag{3.5}$$

with ϵ_0 being the permittivity of free space. α is often estimated as $\alpha = \exp(-1/2) \approx 0.61$. In the more complicated magnetized plasma of a helicon source, α may be larger. In CHEWIE, Eq. (3.4) and the typical plasma quantities give $\alpha \approx 0.75$. I_i is determined from a linear fit to the *I-V* trace in the ion saturation region. I_i^{sat} is the value of that linear fit extrapolated to the floating potential. The density is then computed by rewriting Eq.(3.6) as

$$n_i = \frac{m_i^{1/2}}{\alpha q A_p} \frac{I_i^{sat}}{(k_B T_e)^{1/2}}. \tag{3.6}$$

3.1.2.2 Orbital Motion Limited Theory (OML)

OML is also based on early work by Mott-Smith and Langmuir.[28] Here the discussion of OML is based on the analysis of *Chen et al.*[43]. Whereas the CA method assumed particles approach the probe radially, ignoring any angular momentum, OML theory assumes that ions with large amounts of angular momentum will pass the probe and will not be collected. Ions with small

enough angular momentum are attracted to the probe and collected. With these assumptions, the ion saturation current is[43]

$$I_i(V) = A_p n_i e \frac{\sqrt{2}}{\pi} \left[\frac{e(\phi_p - V)}{m_i} \right]^{1/2}. \tag{3.7}$$

From this expression, I_i scales as $\sqrt{V}$ for large values of V. Thus, I_i^{sat} is determined from a linear fit of I^2 versus V and evaluating the fit at the floating potential, ϕ_f. In other words, $I_i^{sat} = I_i(\phi_f)$. Rearranging Eq. (3.7) and evaluating it at $V = \phi_f$ gives

$$n_i = n_{\mathrm{OML}} = \frac{\pi}{A_p} \sqrt{\frac{m_i}{2e^3}} \frac{I_i^{sat}}{\sqrt{\phi_p - \phi_f}}, \tag{3.8}$$

A major benefit of the OML method is that the density given in Eq. (3.8) does not require a measurement of T_e. However, OML theory is only valid for large sheaths, i.e., when the ratio of the probe radius, r_p, to the Debye length is much smaller than one, $\xi_p = r_p/\lambda_D << 1$, when collisions are neglected, and possibly only for plasma densities below $\sim 10^{11}$ cm^{-3}.[43]

3.1.2.3 Child-Langmuir Floating Point Analysis (CL)

Hoping to relax the $\xi_p << 1$ requirement of OML, *Chen et al.* proposed the Child-Langmuir method (CL).[44] The CL method arose from an observation that in systems with plasma densities in the range $n \sim 10^{10} - 10^{12}$ cm^{-3}, the ion saturation current of cylindrical probes tended to follow a $V \propto I^{4/3}$ relation, similar to the Child-Langmuir law for planar electrodes. This is the same plasma density range of the CHEWIE plasma source. *Chen et al.* then proposed that the Child-Langmuir law holds for cylindrical probes in RF plasmas, regardless of geometry. This assumption is equivalent to arguing that the collection area of the probe is not its surface area, A_p, but the area of a sheath that expands as a function of a power of the applied voltage, $A_{sh} \propto V^{3/4}$. With this assumption, the collected ion current is then given by the Bohm criterion,

as in CA, with A_p replaced with A_{sh}

$$I_i = \alpha_0 n_i q A_{sh} \left(\frac{k_B T_e}{m_i} \right)^{1/2}, \tag{3.9}$$

giving density

$$n_i = \frac{I_i}{\alpha_0 q A_{sh}} \sqrt{\frac{m_i}{k_B T_e}}, \tag{3.10}$$

which, like the CA method, requires knowledge of T_e.

Finding I_i^{sat} and T_e is accomplished in the same manner as the CA and OML methods: with a linear fit to I_i in the ion saturation region, which is then extrapolated to ϕ_f so that the ion current contribution can be subtracted from the total current. Then the inverse slope of $\ln(I_e)$ yields the electron temperature. The only difference is that the I-V curve is a graph of $I^{4/3}$ versus V graph instead of I versus V or I^2 versus V.

Calculating A_{sh} is different from calculating A_p in two ways. First, the current collected by the flat end of a cylindrical probe is assumed to be $< 5\%$ of the total and neglected. Second, the probe radius, r_p is replaced with the sheath radius, $r_{sh} = r_p + d$, where[44]

$$d = \frac{1}{3}\sqrt{\frac{2}{\alpha_0}}(2\eta_f)^{3/4}\lambda_D = \frac{1}{3}\sqrt{\frac{2}{\alpha_0}}(2\eta_f)^{3/4}\left(\frac{\epsilon_0 k_B T_e}{e^2}\right)^{1/2} n_e^{1/2}. \tag{3.11}$$

The new quantity, η_f, is the ratio of the difference between the probe potential and the plasma potential to the thermal kinetic energy,

$$\eta(V) = -\frac{e(V - \phi_p)}{k_B T_e} \tag{3.12}$$

evaluated at the floating potential, $\eta_f = \eta(\phi_f)$.

Plugging the expression for A_{sh} back into Eq. (3.10) gives a quadratic equation in $n_i^{1/2}$, such that

$$n_i = \left(\frac{-B \pm \sqrt{B^2 + 4AC}}{2A} \right)^2, \tag{3.13}$$

where

$$A = r_p,$$

$$B = \eta_f^{3/4} \sqrt{\epsilon_0 k_B T_e / e^2}$$

$$C = \frac{m_i^{1/2}}{2\pi l_p e \alpha_0} \frac{I_i^{sat}}{k_B T_e}$$

It should be noted while *Chen et al.* found densities in RF plasmas calculated using the CL method agreed well with non-perturbative microwave measurements for a certain range of parameters, the CL method of analysis has no theoretical justification.[44]

3.1.3 EEDFs and EEPFs

Most fluid descriptions of plasmas assume that the electron energies obey a Maxwellian energy distribution (in LTE) and that the ions are also Maxwellian or are so cold that $T_i \to 0$ is a valid approximation. The assumption of a Maxwellian energy distribution is frequently invalid in many plasmas of scientific and industrial interest and therefore measurements of fluid parameters such as n and T often do not yield enough information to fully characterize important processes in the plasma. In fact, the deviations from a Maxwellian distribution often provide important insights into the underlying physics that are responsible for observed plasma behavior. A key challenge in trying to recover details of non-Maxwellian energy distributions from probe measurements is that for particles to reach the probe, they must pass through a region of plasma that is significantly disturbed by the introduction of the probe into the plasma.[45] One approach

to resolve this challenge is to use a kinetic framework and measure the full velocity or energy distribution of the particles while also accounting for the effects of the probe perturbation. We begin with the Vlasov-Boltzmann equation,

$$\frac{\partial f}{\partial t} + \mathbf{v} \cdot \nabla_r f + \frac{e}{m_e}(\mathbf{E} + \mathbf{v} \times \mathbf{B}) \cdot \nabla_v f = S, \tag{3.14}$$

where $f(\mathbf{r},\mathbf{v},\mathrm{t})$ is the electron velocity distribution function (EVDF), $\mathbf{E}$ and $\mathbf{B}$ are the electric and magnetic fields, and S represents any sources or sinks of particles in phase space. In equilibrium, the key question is how the EVDF measured at the probe surface $f(\mathbf{r}_s,\ \mathbf{v}_s)$ is related to the EVDF far from the region perturbed by the probe $f(\mathbf{r},\mathbf{v})$. With some approximations about collisions, i.e., about S, and by making assumptions about the shape of $\mathbf{E}(\mathbf{r})$, it is possible to show that the unperturbed $f(\mathbf{r},\ \mathbf{v})$ is related to $f(\mathbf{r}_s,\ \mathbf{v}_s)$ through the current density measured at the probe as a function of the repulsive potential.[45]

Although cylindrical Langmuir probes do not resolve the approach direction of the particles they collect, they do provide some information about the energies of those particles since the particle kinetic energy, ε, must be sufficient to overcome the repulsive Coulomb potential of the probe. The speed v and kinetic energy ε are related through simple kinematics, $v = \sqrt{2\varepsilon/m_e}$. Using this simple kinematic relationship, it is possible to express the EVDF in terms of the electron energy distribution function (EEDF), written $f_\epsilon(\mathbf{r},\ \varepsilon)$, or the electron energy probability function (EEPF), written $f_p(\mathbf{r},\ \varepsilon)$.

In these experiments, the Druyvesteyn method of Langmuir probe trace derivatives is used to obtain the electron temperature and the EEDF.[46] For systems where the electron gyro radius, $\rho_e (\sim 10^{-3}$ cm), is smaller than the probe radius and the probe is perpendicular to the

magnetic field, Godyak and Demidov showed that the EEDF is given by[46]

$$f(\varepsilon) = -\sqrt{e(V_p - V_B)}\frac{3m_e^2}{16\pi^2 e^3 \rho_e V_B}\ln(\pi l 4 r_p)\frac{d^2 I_e}{dV_B^2} \tag{3.15}$$

where $f(\varepsilon)$ is the EEDF, V_B is the probe bias voltage, l is the probe length, and I_e is the electron current (total probe current minus the ion contribution). The relatively large collection area of our probe makes it straightforward to perform the ion saturation current subtraction, however the resultant EEDF may lose accuracy at low energies.[46] Because we are interested in the high energy electrons for this work, the large probe approximation for the Druyvesteyn method (probe radius greater than the electron gyro radius) was used.

Once the EEDF or EEPF is determined, the fluid quantities are derived from the energy moments. The distribution is normalized to the electron density, so that the 0^{th}-moment is

$$n_e = \int_0^\infty f_\epsilon(\varepsilon)\, d\varepsilon = \int_0^\infty \varepsilon^{1/2} f_p(\varepsilon)\, d\varepsilon \tag{3.16}$$

For electron energies measured in eV, $[f_\epsilon(\varepsilon)] = \text{eV}^{-1}\text{m}^{-3}$,[46] the temperature is defined relative to the mean energy of the distribution (instead of by the distribution width for Maxwellian electrons) such that the 1^{st}-moment of the energy distribution provides the effective temperature,

$$T_{\text{eff}} = \frac{2}{3}\langle\varepsilon\rangle = \frac{2}{3}\frac{1}{n_e}\int_0^\infty \varepsilon f_\epsilon(\varepsilon)\, d\varepsilon = \frac{2}{3}\frac{1}{n_e}\int_0^\infty \varepsilon^{3/2} f_p(\varepsilon)\, d\varepsilon, \tag{3.17}$$

More detailed discussion of electron distribution functions measurements from probes can be found in Refs. [47], [46], [48], [49], and [50]. Note: many authors are casual in labeling EEDFs and EEPFs correctly and often do not declare the units in their formulae. It is easy to find examples of EEDFs, and EEPFs mislabeled or interchanged within a single paragraph in the literature. Absent or extra factors of e and m_e occur frequently in published equations. It is

advised to verify these functions by their units before using them in calculations to avoid extra factors of 10^{-19} or 10^{-31}.

3.2 Optical Emission Spectroscopy

3.2.1 Theory

Collisions between ions, neutral atoms, and electrons in a plasma constantly pump electrons to excited electronic states of the neutrals and ions (above the ground state). Those excited states with dipole allowed transitions to lower energy states will decay spontaneously or through additional collisions. The excited states that decay emit a photon of wavelength λ and energy $E_{ji} = hc/\lambda$, where h is Planck's constant, c is the speed of light, and j and i are the higher energy, excited, state and the lower state, respectively. The lifetime of the excited state is the inverse of the Einstein transition probability for spontaneous emission, A_{ji}.[51] For a known state lifetime, the number of photon emissions per time per unit volume, N_{ji}, from level j to level i is given by

$$N_{ji} = n_j A_{ji}, \tag{3.18}$$

where n_j is the number density of ions or atoms in level j. The emissivity ε_λ, the energy per volume per time per solid angle for a given transition/wavelength is then

$$\varepsilon_\lambda = \frac{1}{4\pi} E_{ji} N_{ji} = \frac{hc}{4\pi\lambda} A_{ji} n_j \tag{3.19}$$

In these experiments, light from the spontaneous decays in the plasma is collected by a series of optics and conveyed to a spectrometer with an optical fiber. This diagnostic method is known as Optical Emission Spectroscopy (OES). The intensity of the light collected from a specific

transition is

$$C_\lambda = \varepsilon_\lambda V\Omega = \frac{hc}{4\pi\lambda} A_{ji} n_j V\Omega, \tag{3.20}$$

where Ω is the solid angle over which the optics collect light and V is the plasma volume contained within Ω. The measured signal at a particular wavelength depends on the intensity of the collected light and the wavelength dependent sensitivity of the spectrometer. The spectrometer sensitivity is a product of the sensitivity of the CCD camera used for light detection, Ψ_λ, and the transmission efficiency of the spectrometer, T_λ. The CCD sensitivity, Ψ_λ, for a given wavelength, is given by:

$$\Psi_\lambda = \eta_\lambda G E_\lambda = \eta_\lambda G \frac{\lambda}{hc}, \tag{3.21}$$

where G is gain of the detector and η_λ is the quantum efficiency of the CCD, defined as the number of electrons produced per number of incident photons and having units of percent.[52] A plot of the quantum efficiency is given in Fig. 3.7. The wavelength dependent current recorded by the CCD in counts per second is therefore

$$C_p(\lambda) = \chi T_\lambda I_\lambda \Psi_\lambda = \frac{\Omega}{4\pi} A_{ji} n_j V \chi T_\lambda \eta_\lambda G., \tag{3.22}$$

where a factor of χ has been introduced to account for the transmission efficiency of the collection optics into the optical fiber and through the entrance slit of the spectrometer.

The gain, G, of the detector is provided by the manufacturer and the efficiency product $\chi T_\lambda \eta_\lambda$ is directly measurable using a source of known intensity as a function of wavelength. The efficiency product is a constant throughout the experiments in this work and all line intensity measurements are normalized to account for the wavelength dependence of the efficiency product.

OES measurements of relative changes in line intensity are not terribly difficult. However,

using OES measurements to determine the absolute density, N, or number density, n, and thus the emissivity, ϵ, of a particular excited electronic state or the electron temperature is much more difficult. For low density plasmas, generally up to 10^{10} cm^{-3}, a Coronal Model is often used to relate the measured line intensities to excited state densities (see Fig. 3.5). In a Coronal Model, the emissivity is linearly proportional to the electron density ($\epsilon_\lambda \sim n_e A_{ji} / \sum_l A_{jl}$).[53] For high density plasmas, around 10^{19} cm^{-3} and above, the plasma is in Local Thermodynamic Equilibrium and the emissivity depends on the energy of the transition and the electron temperature ($\epsilon_\lambda \sim A_{ji} e^{E_{ji}/kT_e}$).[53] Neither of these methods are appropriate for the mid-range densities characteristic of CHEWIE, around 10^{12} cm^{-3}. For mid-range densities, a Collisional-Radiative (CR) model is the most appropriate approach.[53]

A CR model is essentially a set of coupled linear differential equations describing the rate of change of the ground and all excited state populations through electron collisions, emission of photons, and absorption of photons.[29] These equations often take a general form of

$$\frac{dN_i}{dt} = n_e \sum_{j \neq i} S_{ji} N_j + \sum_{j>i} A_{ji} N_j - \sum_{j \neq i} S_{ij} N_i - \sum_{j<i} A_{ij} N_i - n_e C_i N_i \tag{3.23}$$

where S_{ji} is a collisional coefficient from the j^{th} to i^{th} state, A_{ji} is the Einstein A coefficient, C_i is the ionization coefficient of state i. Other terms, such as those accounting for collisional lifetimes or recombination effects, can be included as required by plasma conditions. These models, and indeed the real atomic populations of the plasma and their spectra, are heavily dependant on electron temperature and density.[29,54]

In some cases, the electron temperature or electron density can be determined by comparing the ratio of two spectral lines; some ratios will be sensitive to changes in temperature but insensitive to changes in density or vice versa.[54] The reader is directed to Ref. [55] for a

detailed discussion of the analytic techniques, modeling, and computational methods referred to in this work when electron temperatures are determined from ratios of specific spectral lines.

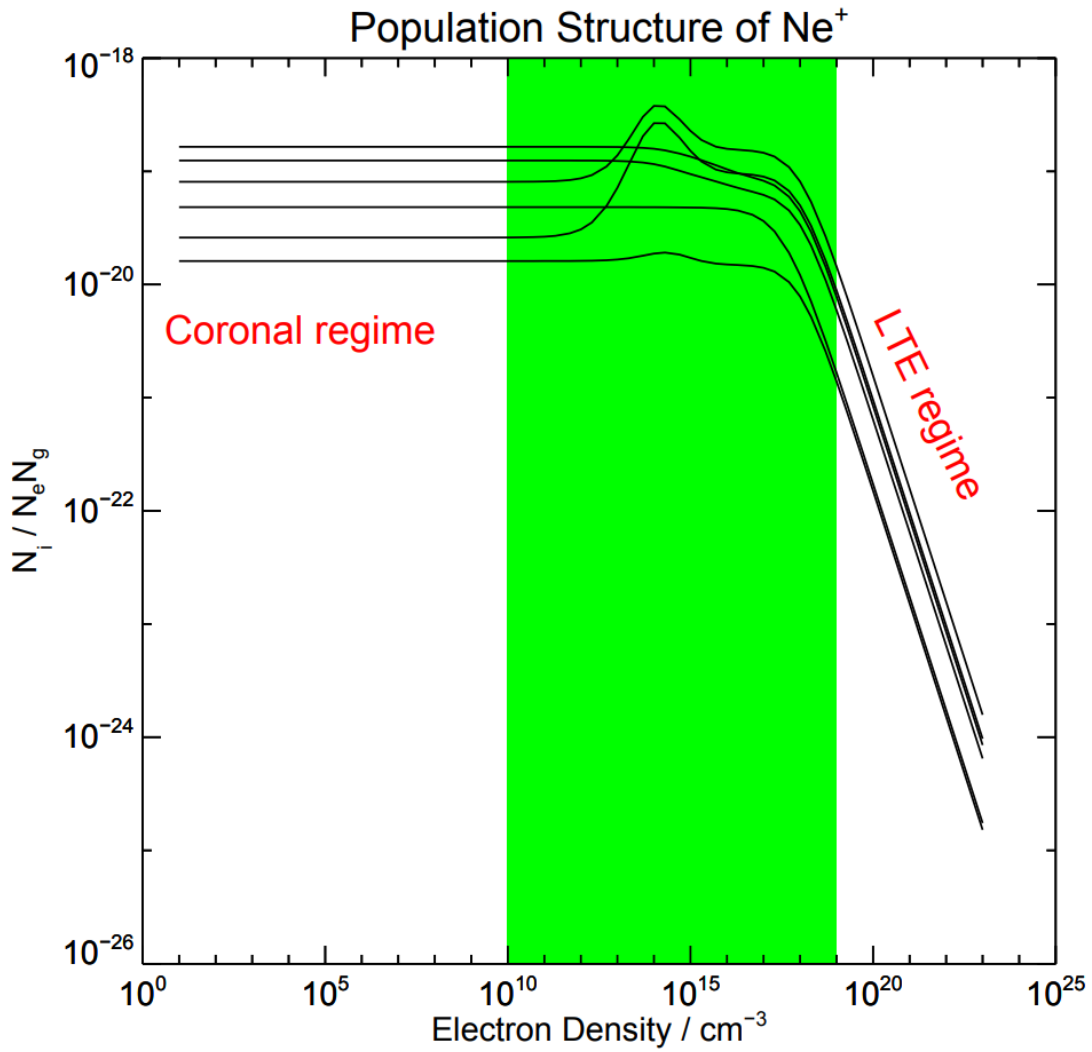

FIGURE 3.5: The electron density regimes best suited for analysis of OES measurements using Coronal Models, LTE models, and Collisional Radiative models (the green shaded region). Figure adapted from [53]

.

3.2.2 OES Instrumentation

A collimated view of line emission was collected by a series of lenses (collection optics) mounted to the front window of CHEWIE. The collected light was focused into a optical fiber. The fiber transmitted the light to another lens which focused the light onto the entrance slit of a

McPherson^{TM} Model 209 High Performance Monochromator-Spectrometer, a diagram of which is shown in Figure 3.6. The primary characteristics of the spectrometer are given in Table 3.1 (Ref.[56]). The intensity of light exiting the spectrometer was measured by an SBIG ST-8300 camera. The quantum efficiency as a function of wavelength of the camera is shown in Figure 3.7.

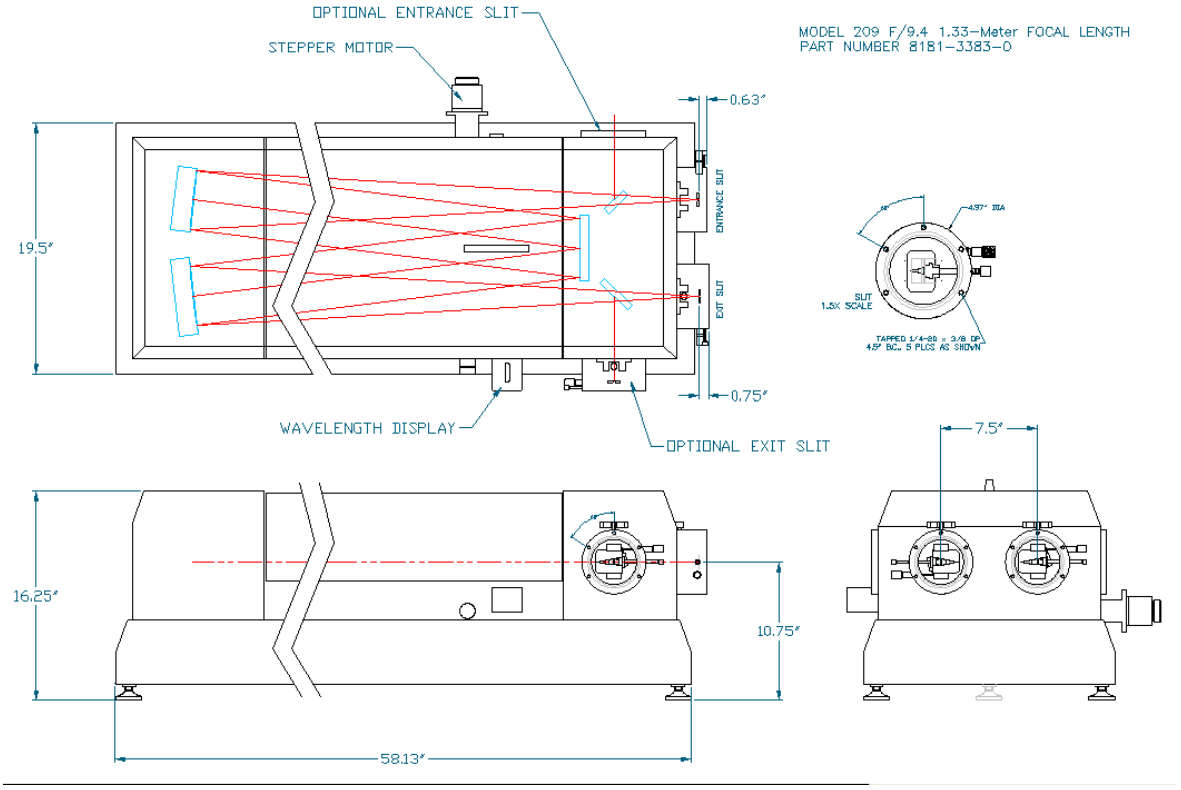

FIGURE 3.6: Schematic of a McPherson^{TM} Model 209 High Performance Monochromator-Spectrometer. Figure adapted from [57]

Grating (G/mm)	1200
Wavelength Range	185 to 650 nm
1^{st} Order Littrow Blaze	250 nm 300 nm 500 nm 750 nm 1.0 μm Holographic
Resolution (nm)	0.015
Dispersion (nm/mm)	0.62
Wavelength Range at Focal Plane (eV)	31 nm
Wavelength Accuracy (nm)	$\pm$0.05 nm
Wavelength Reproducibility (nm)	$\pm$0.005 nm
Counter Reading	actual

TABLE 3.1: Values for McPherson model 209 Monochromator-Spectrometer.

Given all the wavelength dependent effects in the optical system: the quantum efficiency of the camera (see Fig. 3.7), the reflectivity of the grating in the spectrometer, the transmission efficiency of the optical fiber, and the transmission efficiency of the lenses, it was necessary to map the combined response curve of the entire optical path using a source of known intensity as a function of wavelength. This was done using an Oriel^{TM} Quartz Tungsten Halogen Lamp Standard of Spectral Irradiance, whose irradiance levels at various wavelengths are directly calculated from NIST data. Using the same collection used for OES data, the known irradiance can be used to calculate the photon flux to the detector. This is then compared to the detector

reading. The resultant response curve is shown in Figure 3.8. The "correction curve," the inverse of the response curve, is shown in Figure 3.9. Each measured spectrum was multiplied by the correction curve to obtain the true relative emission from the plasma at each wavelength.

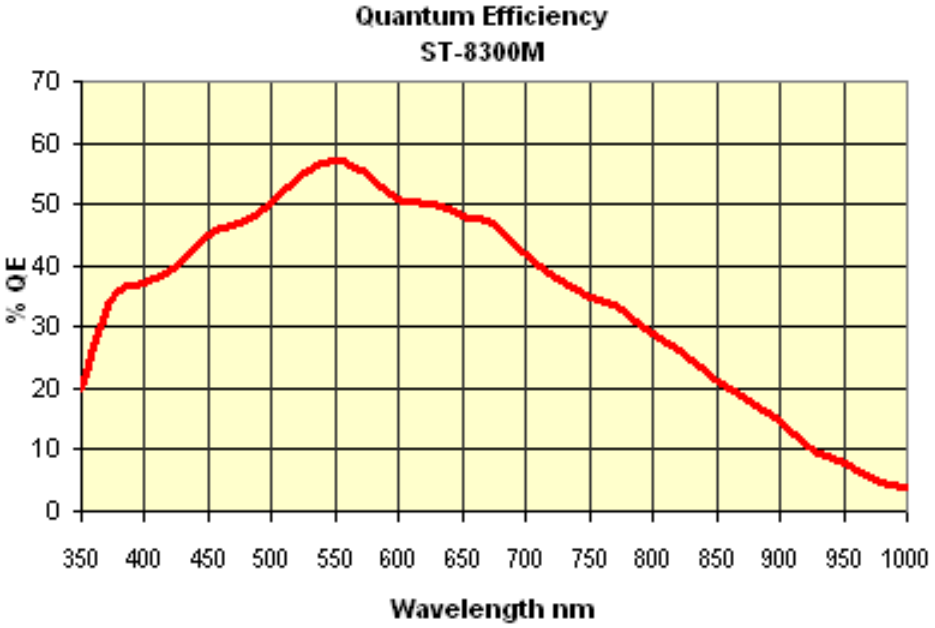

FIGURE 3.7: Quantum efficiency of the SBIG ST-8300 camera. Figure adapted from [52]

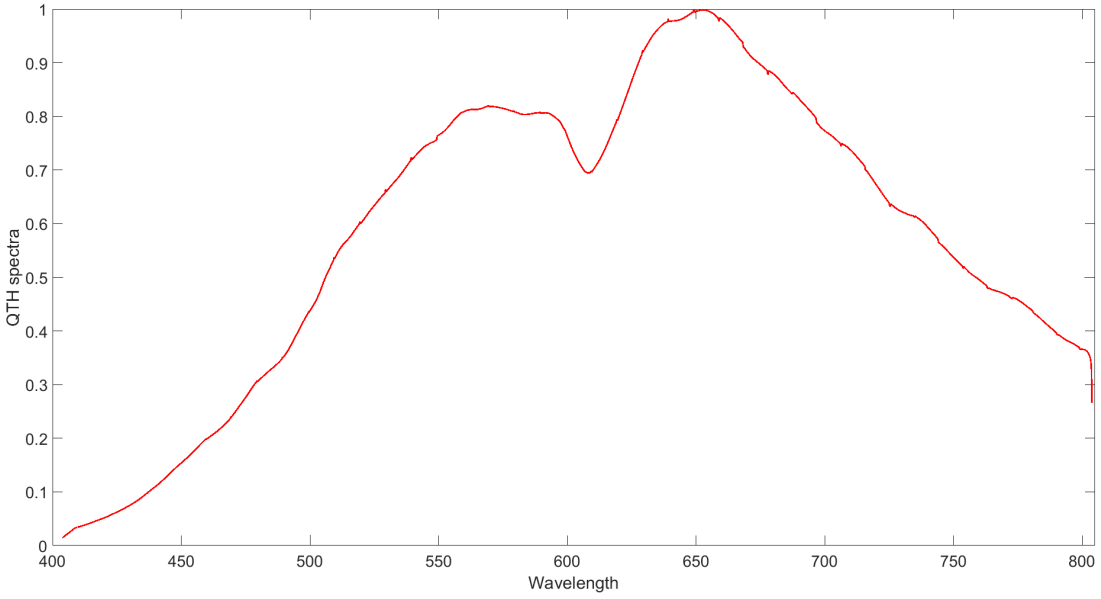

FIGURE 3.8: Overall response curve for the entire optical path including the camera, the optical fiber, and all lenses.

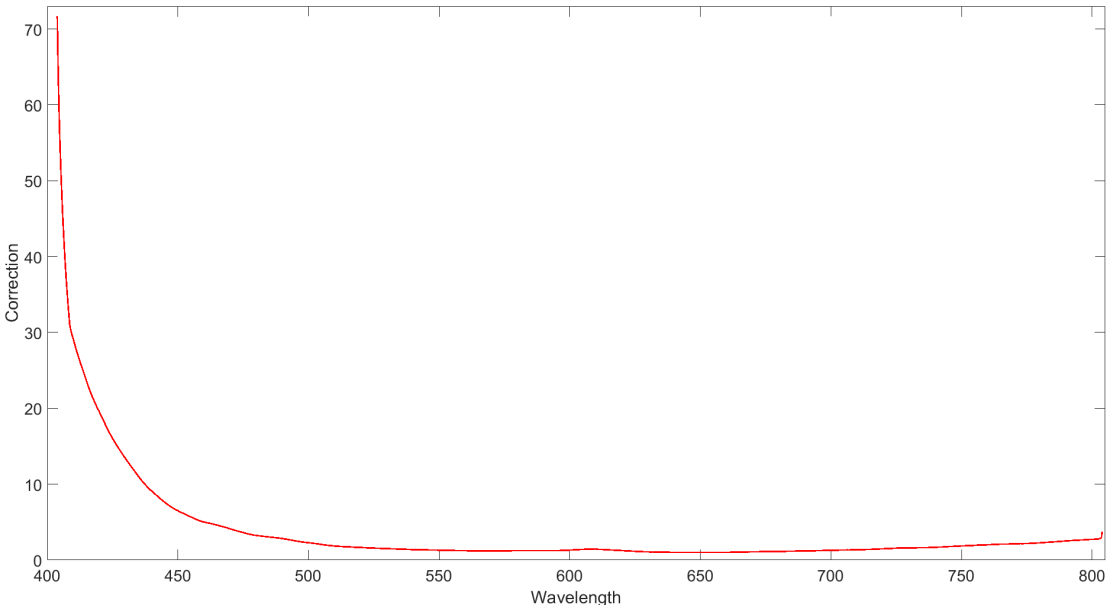

FIGURE 3.9: Correction curve for used for all spectral measurements in this work.

Chapter 4

R-wave Injection

4.1 R-wave Microwave Injection

The R-wave is a right-hand circularly polarized electromagnetic electron wave where its wave vector **k** is parallel to the background magnetic field $\boldsymbol{B_0}$. The cold plasma dispersion relation for the R-wave is given in Ref.[58] as

$$n^2 = \frac{c^2k^2}{\omega_{mw}^2} = 1 - \frac{\omega_{pe}^2}{(\omega_{mw} + i\nu)^2 - (\omega_{mw} + i\nu)\omega_{ce}}, \tag{4.1}$$

where n is the index of refraction of the R wave, c is the speed of light, k is the wave number, $\omega_{mw} = 2\pi f_{mw}$ is the microwave angular frequency, ω_{pe} is the electron plasma frequency, ω_{ce} is the electron cyclotron frequency, and ν is the collision frequency. The wave is resonant (is absorbed) in the plasma where $\omega_{mw}+i\nu = \omega_{ce}$ and has a cutoff (is reflected) at $\omega_R = \frac{1}{2}[\omega_{ce}+(\omega_{ce}^2+4\omega_{pe}^2)^{1/2}]$. In typical ECR plasma sources, microwaves are launched from the high magnetic field side into the iso-surface where the magnitude of the field causes the cyclotron frequency to match the resonant frequency of the injected wave. *Budden* showed that in this case all of the microwave energy is either transmitted through the ECR resonance point or absorbed by the plasma.[59] On

CHEWIE, it is not possible to inject the microwaves from the high magnetic field side of the system due to a lack of access. Instead, microwaves are injected into the the expansion chamber from a region of smaller magnetic field towards a region of larger magnetic field. In this case, the microwaves must tunnel through an evanescent region below ω_R, where $c^2k^2/\omega^2 < 0$, prior to reaching the resonance point. As such, the actual microwave energy accessible at the resonance point is much reduced from the initial injected energy at the quartz window. When injecting from this direction, Budden[59] showed (consistent with the treatments by *Stix*[58], *Swanson*[60], and *Lieberman*[50]) that the percentage of reflected microwave power reflected is

$$R = 1 - e^{-2\vartheta} \tag{4.2}$$

where R is the reflection coefficient, $\vartheta = \pi k_0 a/2$, k_0 is the microwave wave number in vacuum, and a is the thickness of the evanescent region in CHEWIE. Since the dispersion relation depends on the background magnetic field magnitude B_0 and the plasma density n, this requires knowledge of the entire axial density profile in CHEWIE and of the magnetic field in the expansion chamber. To understand the magnetic field structure in CHEWIE, the total magnetic field was calculated numerically based on the geometry of the two electromagnetic coils and the model validated with Gaussmeter measurements in multiple locations. The results of the magnetic field model for a coil current of 375 A are shown in Figure 4.1.

Because there are only two sets of axially distributed ports in the CHEWIE expansion chamber, it is not possible to measure the axial density profile. However, given our single point Langmuir probe measurements at the upper tier of ports in the chamber, knowledge of the magnetic field profile, and axial density profile measurements from other helicon sources, it is possible to estimate the axial density profiles in argon and helium and thereby approximate the thickness of the evanescent region, a.

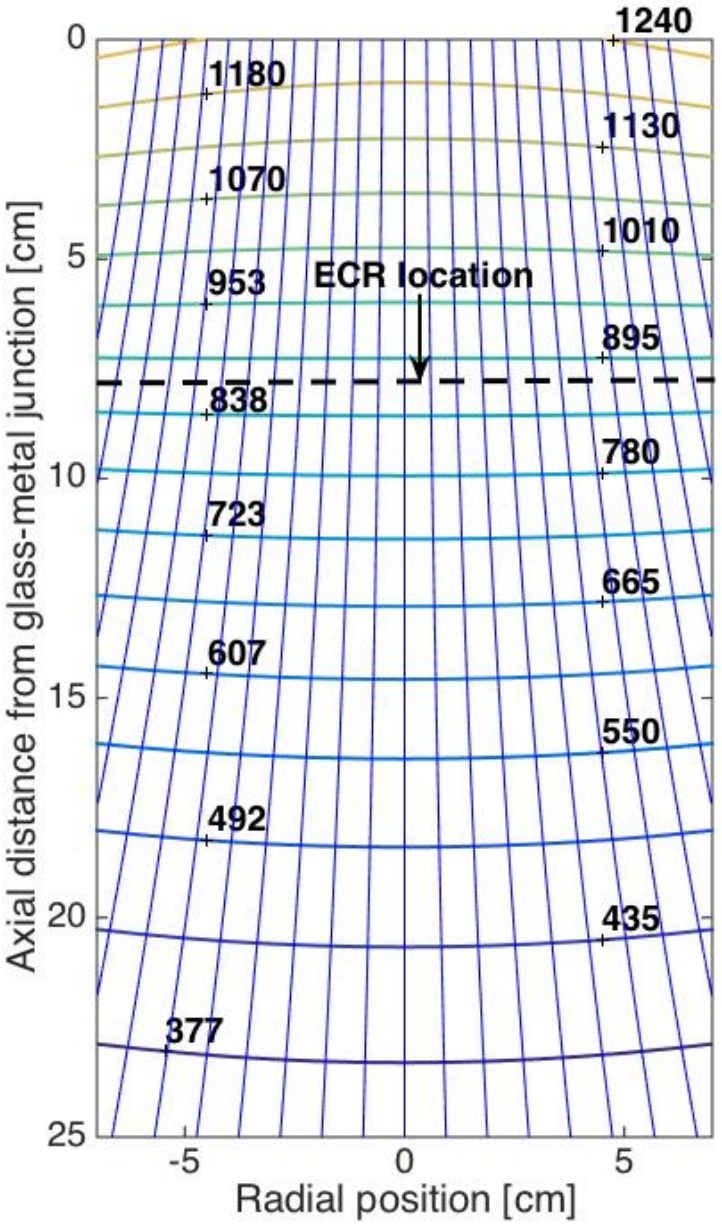

FIGURE 4.1: Magnetic field lines (color) and iso-field contours (black) in the CHEWIE expansion chamber for a solenoid current of 375 A. Iso-field contour values are given in Gauss. The dashed line shows the ECR location in the system.

Figure 4.2 shows the R wave squared index of refraction in the CHEWIE expansion chamber versus the position for argon and helium for different density profiles. The different axial density profiles are based on measurements from experiments by *Charles and Boswell*[61] on a similar small helicon apparatus called Chi-Kung at the Australian National University. Their measurements showed that in regions of rapidly expanding magnetic fields, the plasma density drops off exponentially versus position, on the same scales (magnetic and spatial) as those in CHEWIE. Based on their results, the density profiles in CHEWIE were estimated to go as

$$n_e(z) = n_0 e^{-(z-z_0)/\Lambda}, \tag{4.3}$$

where n_e is the electron density, z is the axial distance from the glass-metal junction, Λ is an exponential decay fitting factor, and n_0, z_0 are the density measured and measurement location at/of the Langmuir probe. Λ is chosen to give a reasonable density profile. For example, for a 500 W, 900 Gauss helicon source at 6 mTorr, a core density upstream of the magnetic resonant surface is 10^{13} cm^{-3} in argon, and for 20 mTorr helium $n_e = 10^{12}$ cm^{-3} is normal (see, for example, data from Ref. [45] for helium and Ref. [62] for argon). $\Lambda = 4.5$ yielded these expected densities upstream and the measured density at z_0. A density profile where n_e varied linearly with the change in magnetic field strength was also considered and is shown as the red curve in Figure 4.2. For the linear case,

$$n_e(z) = n_0 \left[1 + \frac{B(z) - B_0}{B_0}\right], \tag{4.4}$$

where $B(z)$ is the local magnetic field strength and B_0 is the magnetic field strength at z_0 (13.5 cm in Figure 4.1). The predicted density profile changes much more slowly than the exponentially varying profiles and does not yield realistic density maps when compared to results in similar experiments.

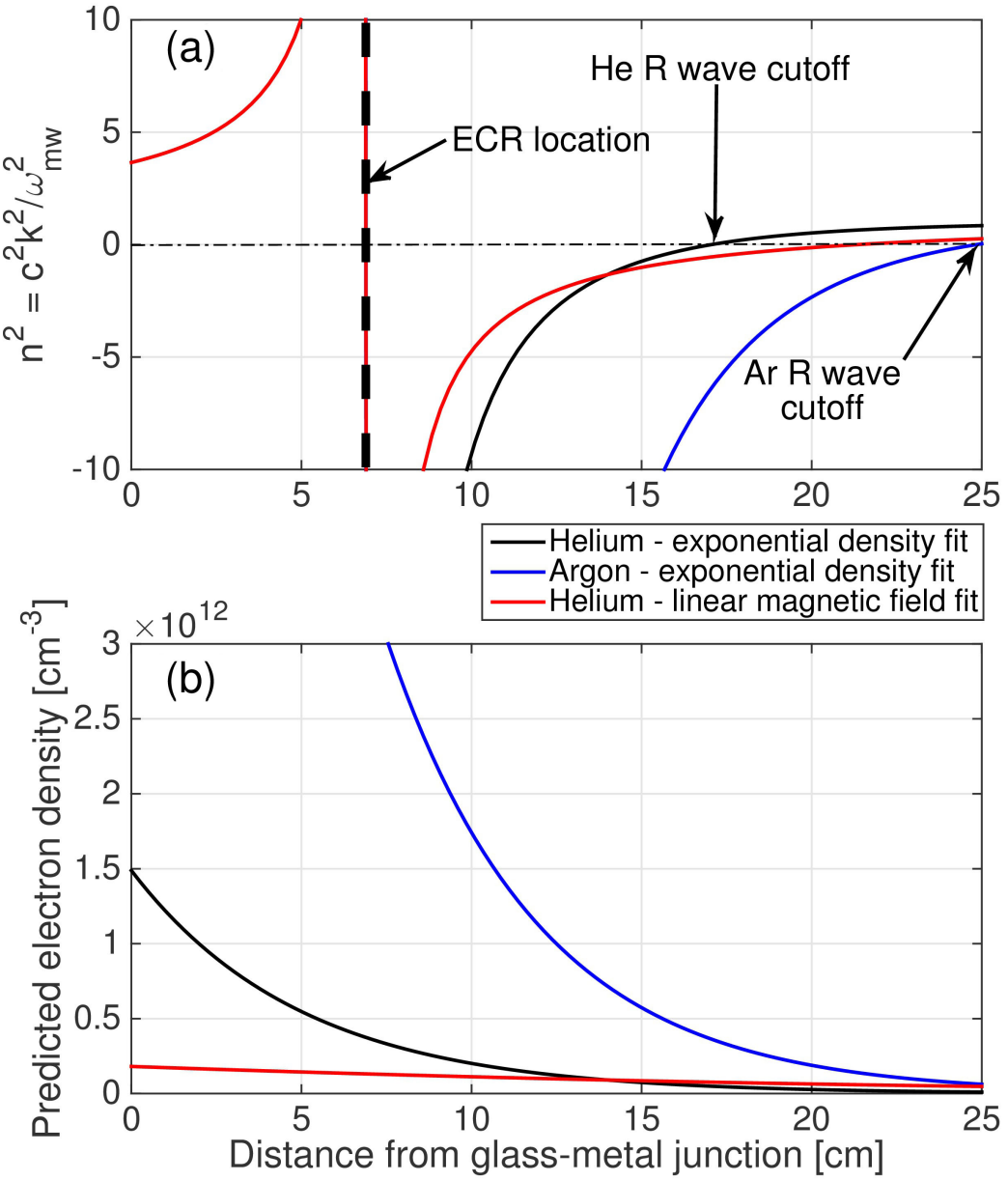

FIGURE 4.2: The a) R-wave index-of-refraction-squared, N^2 versus axial position for b) different models of the axial density profile.

Given these estimated density profiles, the thickness of the evanescent region is the distance between the ECR point (vertical dashed line in Figure 4.2(a) and where the square index of refraction $c^2k^2/\omega^2 = 0$ to the right of this point (both locations are marked in Figure 4.2 for argon and helium). Using this distance for a, the estimated microwave power transmitted to the ECR point, and presumably absorbed by the electrons there, is given by $P_{abs} = P_{in}(1 - R)$, where P_{abs} is the absorbed power, and P_{in} is the 1.2 kW input power. For helium this is calculated to be $P_{abs} \sim 300$ W and for argon $P_{abs} \sim 10$ mW from equation (4.2) and subsequent relations. However, it must be taken into account that since the microwave is initially linearly polarized prior to entering the evanescent region, only half the initial 1.2 kW of power is available to the R wave that resonates with the electrons since a linearly polarized wave is divided evenly in power between the right and left (R and L)-hand polarized waves. Thus, the amount of power available to the electrons in the resonance region is approximately 150 W in helium and only 5 mW in argon. 5 mW is very little power absorbed by argon. A second method of estimating the power absorption in argon plasmas, described in the next section, suggests the assumed axial density profile is incorrect. Nonetheless, these calculations predict that much more power is available at the ECR location in helium than in argon. At the location of the microwave window, the less dense helium plasma allows the propagation of microwaves upward into CHEWIE for several centimeters prior to being cut off. Argon, being more dense, cuts off the microwaves in the plasma much closer to the window. Because of this, in argon the R-wave evanescent region is longer than it is in helium, and thus less power is transmitted to the ECR point in argon compared to the helium plasma.

Another important point is that the microwaves propagate antiparallel to the axial magnetic field direction in CHEWIE, opposite to conventional ECR sources. Again, this is for accessibility reasons. However, even for antiparallel propagation the R-wave cold plasma dispersion relation, including its cutoffs and resonances, as shown in equation (4.1) and as presented

in basic plasma wave texts such as *Stix*[58] is still accurate.

Finally, it should be noted the microwaves in this case damp collisionlessly. The collision frequency of electrons with neutrals (ions) $\nu_{e-n,i}$ is given by $\nu_{e-n,i} = n_{n,i}\sigma_{n,i}v$, where $n_{n,i}$ is the neutral (ion) density, $\sigma_{n,i}$ is the electron-neutral (ion) collision frequency, and v is a characteristic electron speed, in this case the thermal speed given by $\sqrt{T_e/m_e}$. Given cross sections for these processes from *Lieberman*[50], $\nu_{e-n,i} \sim 10$ MHz, which is much less than the $\omega_{mw} \sim 10^{10}$ rad/second of the waves. Thus, from equation (4.1) the collisional damping of the microwaves is negligible. Furthermore, the energy relaxation length[50] for these types of collisions, estimated as $\lambda_\epsilon = \sqrt{\lambda_m \lambda_{inel}/3}$, with λ_m being the total mean free path for momentum transfer and λ_{inel} is the inelastic scattering length, is long compared to the size of the system. The mean free path length of electron collisions with neutrals (ions) is $\lambda_{n,i} = 1/n_{n,i}\sigma_{n,i}$. The cross section[50] for momentum transfer and/or inelastic collisions in CHEWIE is $\sim 10^{20}$ m^2. Given a neutral density of $n_n \sim 10^{20}$ m^{-3} yields λ_ϵ on the order of a meter, longer than the size of the expansion chamber. Thus, the measurement of EEDFs a few centimeters downstream of the ECR location faithfully represents changes to the EEDF at the ECR location.

4.2 R-wave Effects in Argon

Figures 4.3 through 4.5 show density, temperature and EEDF measurements in argon at several different magnetic field strengths for microwaves on and off. These measurements are time-averaged over many 6.4 ms long microwave pulses, so for the microwave on results the temperature results reported are a lower bound. Time-averaged results were preferred in argon plasmas due to the Keithley sourcemeters high bias voltage resolution, an important feature in resolving the EEDF. The switching noise gap in the data is caused by a brief step in the current collected by the sourcemeter as it switched from negative to positive voltages, yielding

erroneous measurements near $V_B = 0$ V. These data are removed during analysis. Without microwaves, the tail of the EEDF above the argon ionization energy was observed to fit a 1.8 eV distribution, as marked by the red line in Figure 4.3. Thus, the tail above the ionization threshold was seen to be depleted, presumably due to ionizing collisions with neutrals. With the injection of microwave energy, the EEDF fit a 2.2 eV distribution from the bulk through the tail for over five decades of collected electron current. The effect of the microwaves was to replenish the high energy electrons in the tail of the distribution above the argon ionization energy. The RF power scan confirmed the existence of the depleted tail without microwaves as in Figure 4.5. Heating of the tail is not simply due to more total input power, but rather the ECR heating with microwaves.

In the previous section, the absorbed power in argon was calculated to be ∼5 mW, due to the long evanescent region the wave must tunnel through to reach the ECR surface. It is possible to compare that prediction to the observed change in the EEDF in Figure 4.3 by calculating the energy change per ECR confinement time between the microwave on and off EEDFs cases in argon. The absorbed power is

$$P_{abs} \approx \frac{(\bar{\epsilon}_{on} - \bar{\epsilon}_{off}) n_e V}{\Delta t} \tag{4.5}$$

where $\bar{\epsilon}_{on,off}$ is the mean electron energy per particle when the microwaves are on/off, V is the approximate volume of the ECR absorption zone, and Δt is a characteristic electron ECR confinement time. *Lieberman*[50] provides an estimate for Δt as

$$\Delta t = \sqrt{\frac{2\pi}{\omega_{ce} v_e |\alpha|}} \tag{4.6}$$

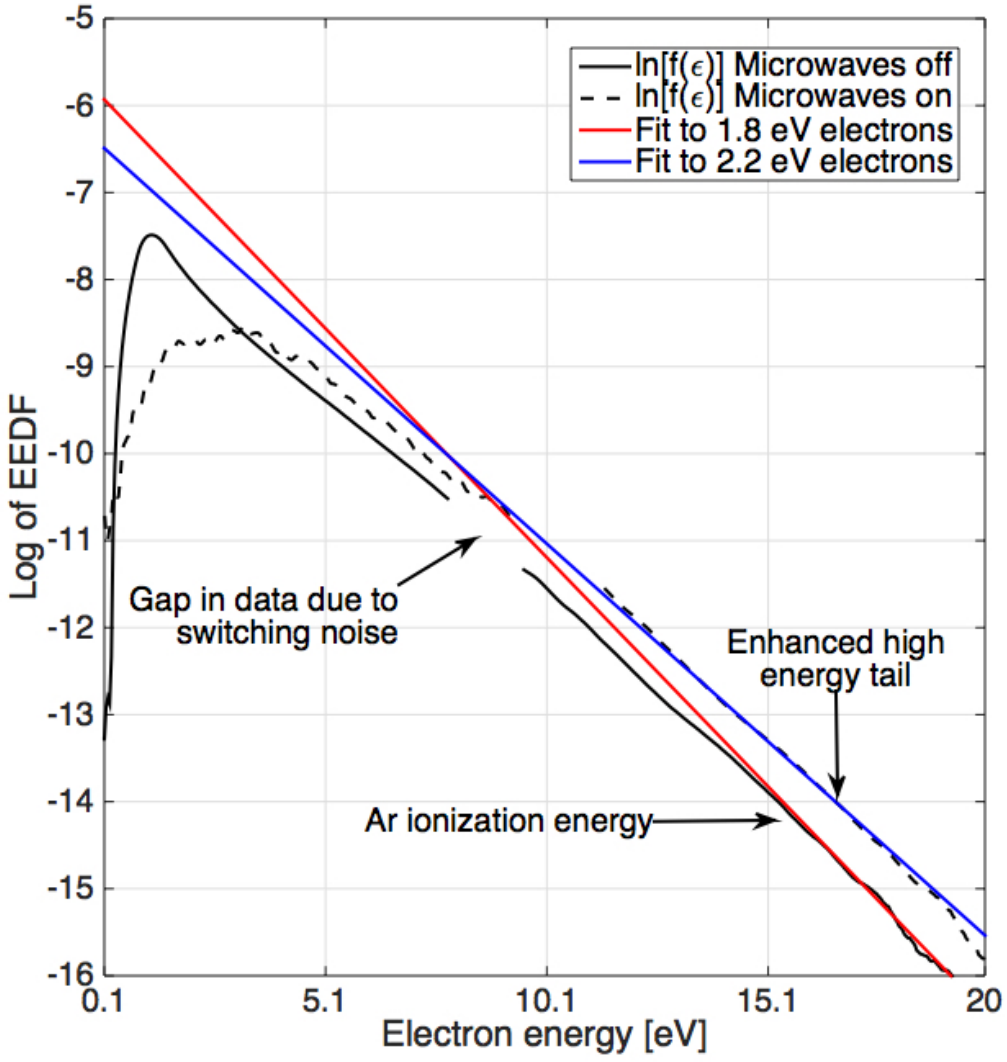

FIGURE 4.3: Representative natural logs of EEDFs taken in Ar (dashed black line) with and (solid black line) without microwave injection. Measurements were taken at an RF power of 400W and 970G magnetic field strength. Solid red and blue lines are Gaussian temperature fits to the tails of the distributions.

where $v_e \sim \sqrt{T_e/m_e}$ and $|\alpha|$ is given by

$$|\alpha| = \frac{1}{B_{ECR}} \frac{\partial B}{\partial z}\bigg|_{z_{res}} \tag{4.7}$$

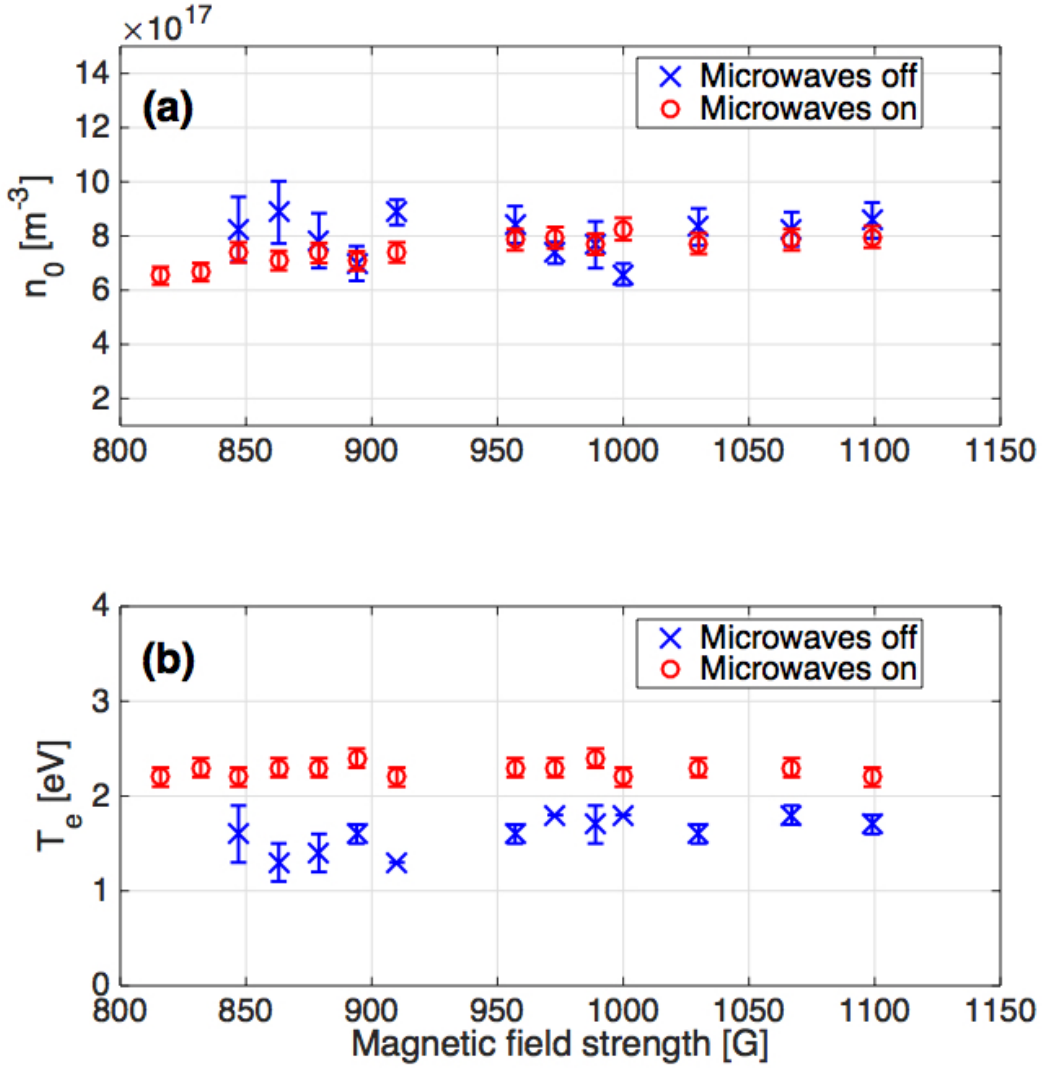

FIGURE 4.4: (a)Plasma density and (b) electron temperaturein Ar versus magnetic field strength. Field strength is recorded for 0 cm radius and 2.5 cm axially in Fig. 4.1 for an RF power of 400W

for $B_{ECR} = 876$ Gauss[50]. z_{res} is the position of the ECR location in the plasma. The average energy per electron is given by

$$\bar{\epsilon} = \frac{1}{n_e} \int_0^\infty \epsilon f(\epsilon) d\epsilon \tag{4.8}$$

where $f(\epsilon)$ is the EEDF. V is given by $\pi R^2 v_e \Delta t$, where R is the radius of the plasma column (in this case $\approx$ 2 cm). Since the density does not change before and after microwave input in

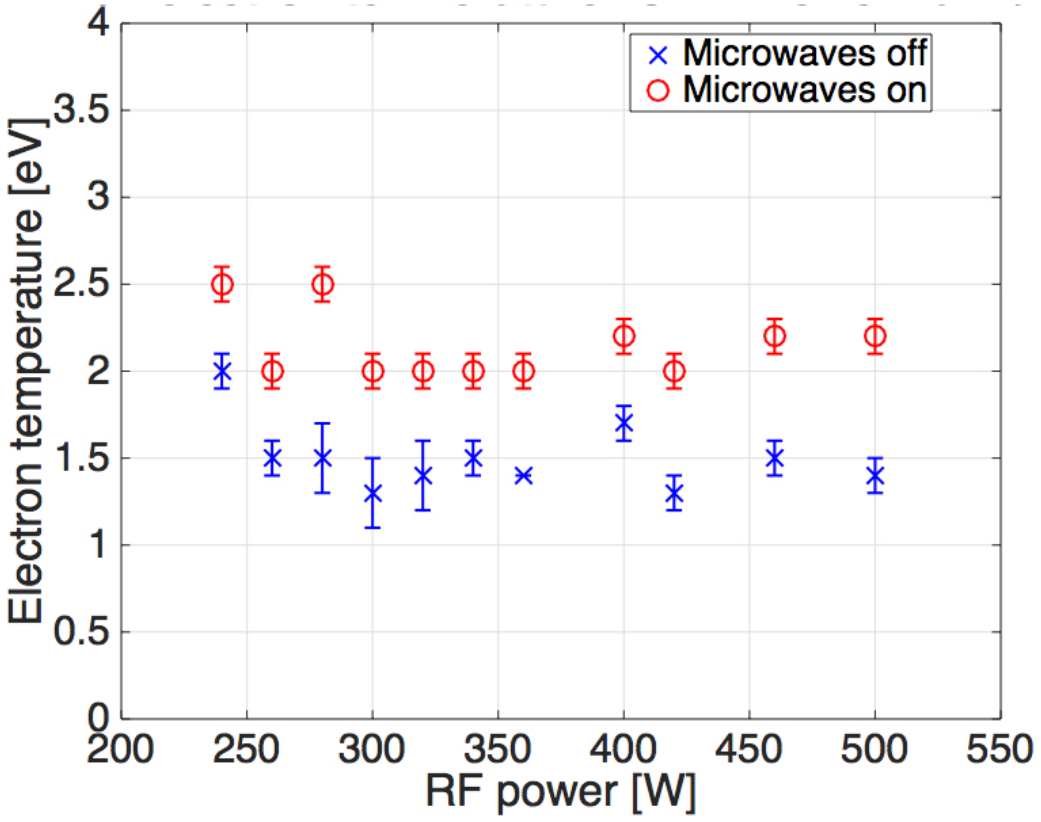

FIGURE 4.5: Electron temperature in the high-energy tail of the EEDF versus RF power in Ar at a magnetic field strength of 917 G at an axial location of 2.5 cm.

argon, from Eq. (4.5)

$$P_{abs} \approx \pi R^2 v_e \int_0^\infty \epsilon[f_{on}(\epsilon) - f_{off}(\epsilon)]d\epsilon \tag{4.9}$$

In this simple estimation, the predicted absorbed power from the change in EEDFs is seen to be independent of the electron confinement time. To evaluate Eq. (4.9) for comparison to the predicted 5 mW transmitted to the ECR zone, functional forms for $f(\epsilon)$ are needed. To do this, the EEDFs from Figure 4.3 are plotted in linear space in Figure 4.6.

The EEDFs here are normalized to their own maxima in Fig. 4.6 and fit to bi-Maxwellian electron distribution functions given by

$$f_{fit}(\epsilon) = A\sqrt{\frac{m_e}{\pi}}\left(\frac{4}{T_1}\right)^{3/2} \epsilon \times \exp(-\epsilon/T_1) + B\sqrt{\frac{m_e}{\pi}}\left(\frac{4}{T_2}\right)^{3/2} \epsilon \times \exp(-\epsilon/T_2) \tag{4.10}$$

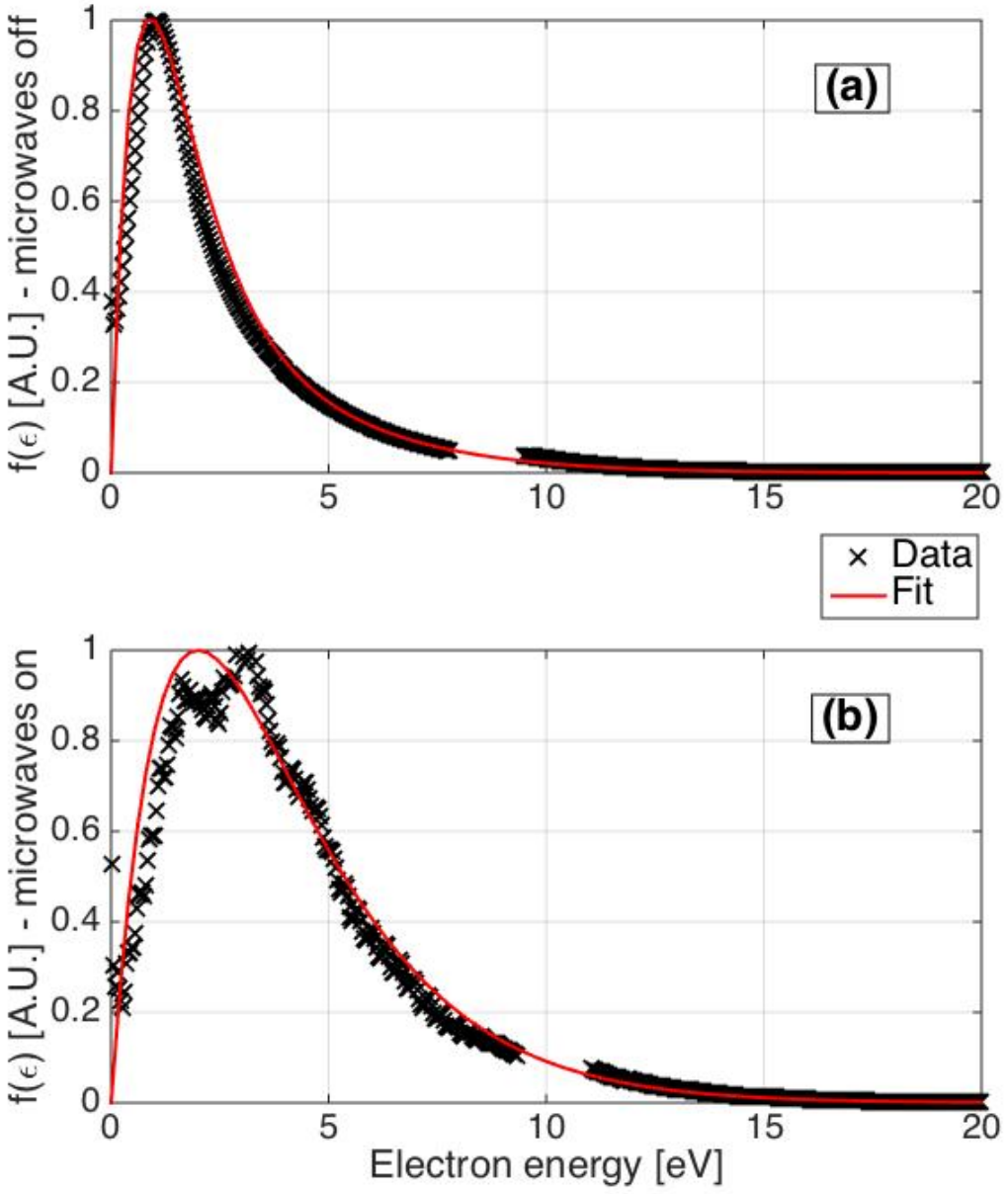

FIGURE 4.6: Normalized EEDFs without (a) and with (b) microwave injection (from Figure 4.3) in Ar as measured by a Langmuir probe. The solid lines are fits to the data using Eq. (4.10).

where A and B are fitting constants and $T_{1,2}$ are the temperatures of the Maxwellian populations that compose the EEDF. The bi-Maxwellian distribution accounts for colder low energy electrons measured by the Langmuir probe, which are not easily discernible in the log plots (Figure 4.3), but are apparent in Figure 4.6. The fitted functions are shown as red solid lines in Fig. 4.6. For the microwaves off measurements $A = 2.5$, $B = 1$, $T_1 = 0.8$ eV and $T_2 = 1.9$ eV. For the on case $A = 1$, $B = 0$, and $T_1 = 2$ eV. Using these forms for $f(\epsilon)$ we obtain $\epsilon_{off} = 2.6$ eV and $\epsilon_{on} = 4$ eV. Then evaluating the rest of Eq. (4.5) using a density of 8×10^{17} m^{-3} we obtain $P_{abs} \approx 100$ mW. The discrepancy between the predicted value of 5 mW and this calculated absorbed power value for argon implies that the density profile estimates are not correct. In other words, the plasma density near the microwave injection port is likely smaller than estimated. A lower density could potentially be due to the density decrease that would occur naturally in the presheath of the wall near the microwave injection window. Unfortunately, without better probe access to this region, the true density profile cannot be ascertained.

Using the analytic fit to the EEDF data it is possible to calculate the high energy tail densities for the microwaves on and off cases. High energy is defined as greater than the argon neutral ionization energy of 15.76 eV. The density of the high energy tail of the EEDF is

$$n_e(\epsilon > \epsilon_{iz}) = n_e \int_{\epsilon_{iz}}^{\infty} f(\epsilon) d\epsilon, \tag{4.11}$$

where ϵ_{iz} is the ionization energy. Using this and the functional fits to the EEDF data, $n_{on}(\epsilon > \epsilon_{iz}) = 0.026 n_e$ and $n_{off}(\epsilon > \epsilon_{iz}) = 0.006 n_e$. Thus, there is a more than fourfold increase in the high energy portion of the EEDF when the microwaves are on.

Figure 4.7 shows representative Langmuir probe traces before and after the ECR condition was achieved, with microwaves on in both cases. The no ECR traces in this figure were taken at a field strength of 800 G in Figure 4.4. At this solenoid coil current the ECR condition was

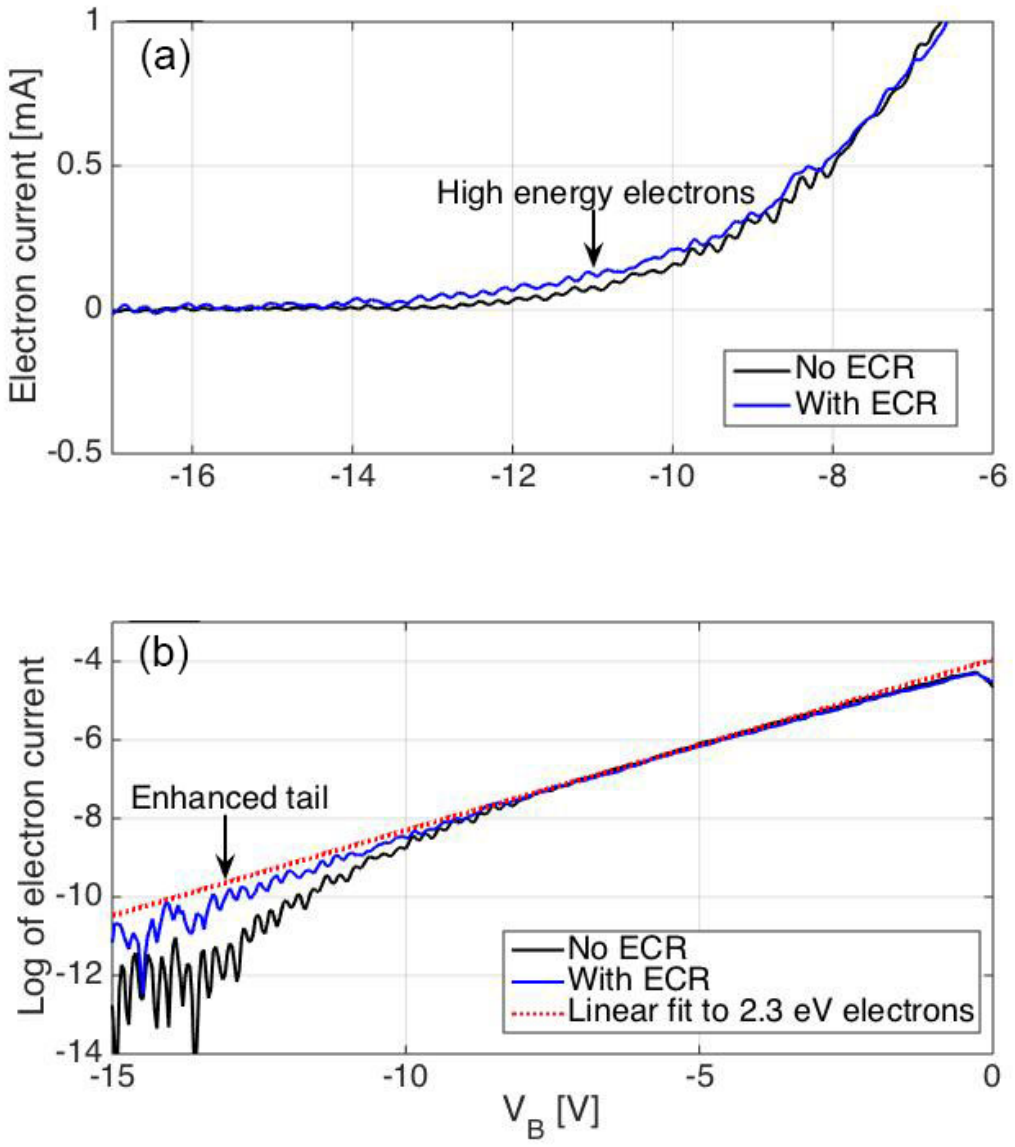

FIGURE 4.7: (a) Electron current and (b) natural log of electron current in Ar with (blue) and without (black) the presence of an ECR.

not achieved anywhere in the system, not even at the maximum field location at the radial center of the Pyrex discharge chamber. The log of the electron trace shows a bulk 2.3 eV electron population with a depleted high energy tail. When the field was increased to 917 G (the seventh microwave on data point from the left in Figure 4.4) the tail is replenished and fits the same 2.3 eV distribution. Thus, the effects of microwave heating were only observed in argon at fields where the ECR condition was achieved somewhere in the vacuum chamber.

This agrees with the long energy relaxation length (compared to the system size) calculated for this experiment in section 4.1. Figure 4.5 shows the electron temperature measured above the ionization energy for different magnetic field strengths with and without microwaves. For all tested parameters the tail was seen to be hotter with microwaves in the plasma. An increase in density (Figure 4.4(a)) was not observed. However a marked increased in argon ion emission lines was observed (Figure 4.8). The measured neutral argon emission levels did not change with the application of microwaves. The constancy of the measured ion density and neutral emission levels, along with the increase in argon ion emission indicates that the effect of replenishing the tail of the EEDF using microwaves populates the higher energy argon ion electronic states, without causing further ionization. The ion transitions observed here, at 663.82, 663.97, 664.37, 666.63, and 668.61 nm are due to relaxations of the 4p Ar (II) state. The neutral lines observed at 666.07, 666.4, and 667.73 nm are due to Ar (I) relaxations from the $6s \rightarrow 4p$, $4d \rightarrow 4p$, and $4p \rightarrow 4s$ states. The relative strength of a given OES line is given by the rate at which the higher state of the transition is pumped, assuming constant collisional and radiative loss rates. To estimate relative ion and neutral excited state pumping rates, only electron-impact excitation is considered here. Given this, the pumping rate from state 1 to 2 is

$$G_{1\rightarrow 2} = n_e n_{n,i} \int_{\epsilon_{1\rightarrow 2}}^{\infty} \sigma_{1\rightarrow 2}(\epsilon)\epsilon f(\epsilon) d\epsilon, \tag{4.12}$$

where $G_{1\rightarrow 2}$ is the pumping rate, $n_{n,i}$ is the density of the atom or ion getting pumped, $\sigma_{1\rightarrow 2}$ is the excitation cross section for that transition, and $\epsilon_{1\rightarrow 2}$ is the energy difference between states 1 and 2.

The upper ion states for the transitions observed can be directly pumped from the ground state argon ion. The cross section for this collision is given by *Strini et al.* to be $\leq 10^{-21}$ m^2.[63] To pump the upper states for the observed neutral transitions, the most efficient way

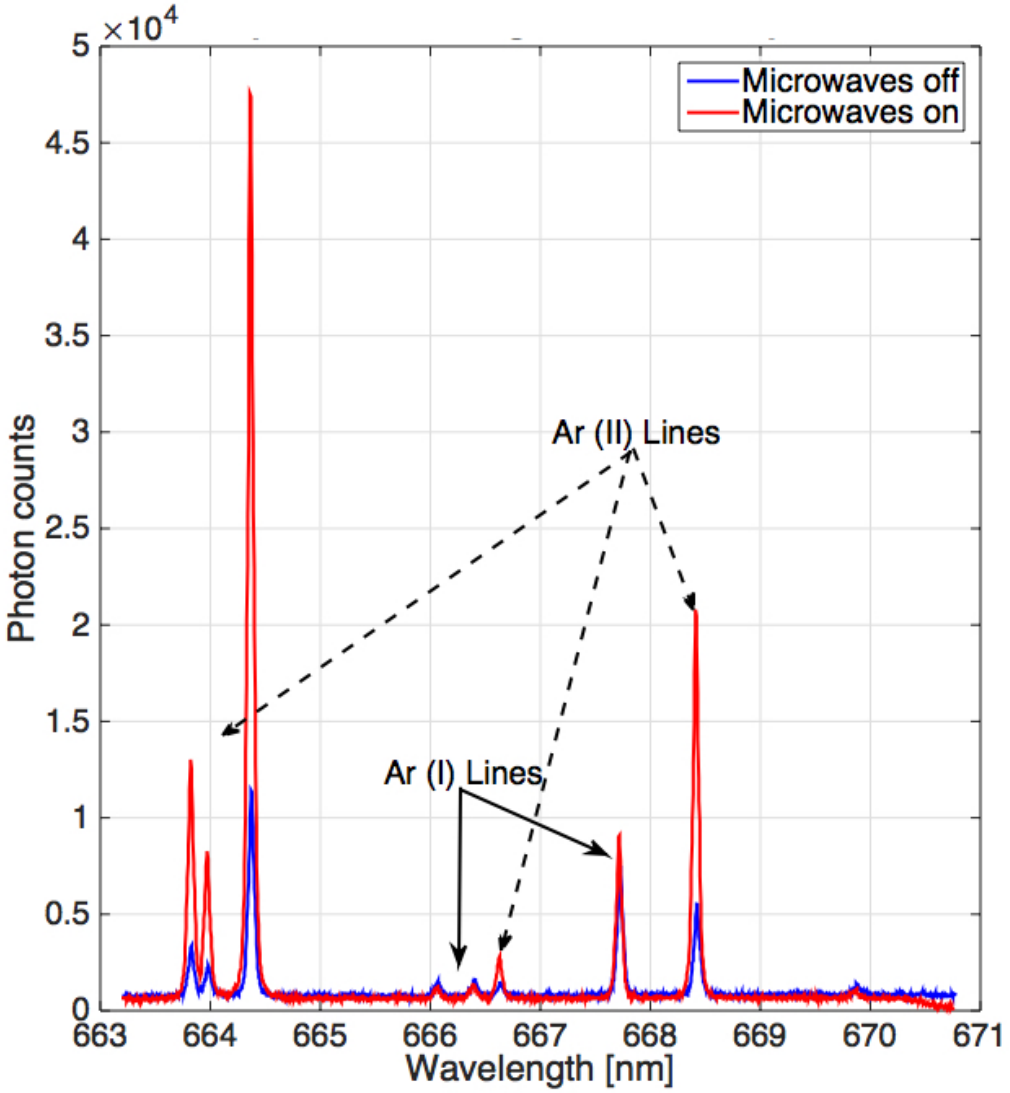

FIGURE 4.8: Ar neutral and ion transitions observed with (red) and without (blue) microwaves. RF power and magnetic field strength are identical to data shown in Figure 4.3

is to pump first to the $4p$ states, and from there to the upper level states. Pumping to the $4p$ state can occur via a single collision from the ground state ion, or via an electron collision with the $4s$ Ar (I) metastable state[64]. Thus, the neutral 666 nm emission lines observed here require at least two electron-neutral collisions to be observed. Though the 667 nm line can be pumped from the ground state Ar (I), the more likely scenario is that is it pumped from the $4s$ metastable state, as the $4s \rightarrow 4p$ excitation cross section is 10 times greater than the $3p \rightarrow 4p$ excitation cross section, and the $4s$ state is very long lived (with lifetimes up to 38 s

long)[64]. Because of this, the neutral excitation cross section from the ground state atom requires a full collisional-radiative model for the 666 nm lines (Ref.[65]) for example). In lieu of this, an effective collision cross section for populating the upper states of the argon atom from the ground state is estimated as no greater than the ground state to the $4p$ Ar (I) excitation cross section. That is, $\sigma^{Ar}_{eff} \leq \sigma^{Ar}_{3p\rightarrow 4p} \leq 5\times 10^{-22}$ m^2.[64] For a given time, the change in excited state population due to a change in EEDF because of microwaves, again for fixed loss rates of excited states, is given by

$$\Delta G_{1\rightarrow 2} = n_e n_{n,i} \int_{\epsilon_{1\rightarrow 2}}^{\infty} \sigma_{1\rightarrow 2}(\epsilon)\epsilon(f_{on}(\epsilon) - f_{off}(\epsilon))d\epsilon. \tag{4.13}$$

Comparing the change in pump rates between excited ions and neutrals for the relevant states we have

$$\frac{\Delta G^{Ar^+}_{3p\rightarrow 4p}}{\Delta G^{Ar}_{3p\rightarrow 4p}} \approx \frac{n_i \int_{\epsilon^{Ar^+}_{3p\rightarrow 4p}}^{\infty} \sigma^{Ar^+}_{3p\rightarrow 4p}\epsilon(f_{on} - f_{off})d\epsilon}{n_n \int_{\epsilon^{Ar}_{3p\rightarrow 4p}}^{\infty} \sigma^{Ar}_{eff}\epsilon(f_{on} - f_{off})d\epsilon} > 1. \tag{4.14}$$

Because $n_i \approx n_n$ in the core[66], and because $\sigma^{Ar^+}_{3p\rightarrow 4p} \gg \sigma^{Ar}_{eff}$, the change in the EEDF due to microwave heating has a disproportionately larger effect on the ion excitation rates than it does on the neutral rates, as is observed in the change in ion and neutral spectra in Figure 4.8.

It is true that the assumptions of constant loss rates and approximate equivalence of densities cannot be checked in these experiments and that a full collisional-radiative model is necessary to truly calculate the relative excited populations due to a change in the EEDF. However, these measurements are consistent with concluding that the ion excitation cross sections are much greater than the effective neutral excitation cross sections and are preferentially pumped after small changes in the tail of the EEDF. These observations have significant implications for microwave heating of RF plasmas as well as laser-plasma diagnostic development.

4.3 R-wave Effects In Helium

Because helium produces much lower density plasmas compared to argon for the same RF power, the highest solenoid coil current possible was used. This yielded a magnetic field profile in the expansion chamber as shown in Figure 4.1. Repeating the parameters scans used for argon plasmas, Figures 4.9 and 4.10 show measurements of the time-averaged electron density and temperature over scans of the magnetic field strength and rf power. While the time averaged electron density (Figure 4.9(a)) shows no significant changes with microwave injection, as in the case with argon, there is a significant increase in the time-averaged electron temperature when the microwaves are on. In both the magnetic field and RF power scans, the increase in time-averaged electron temperature is between 1 and 2 eV. To more fully understand the impact of the microwaves on the EEDF in these helium plasmas, additional time-resolved Langmuir probe measurements were performed. Figure 4.11 shows two representative Langmuir probe traces obtained in helium 3.9 ms into the microwave pulse. There is a clear increase in the electron and ion saturation currents (density) and a clear change in the electron temperature (curve shape) when the microwaves are on. Measurements of the time-resolved electron density show that the addition of microwaves to the helium helicon plasma yielded changes in ion density by more than a factor of two, as shown in Figure 4.12.

Because of the large time-dependent changes in the electron density when the microwaves were on, the time-averaged measurements with the Keithley sourcemeter showed strong oscillations. As a result, the sourcemeter was used to measure current at individual voltage steps while the microwave output was at its peak. From the microwave diode output (measuring refleced microwave power) in Figure 4.13 it is clear that initially, only 50% of the microwave power is being reflected by the plasma, the rest is either being absorbed or propagating through the ECR zone. Because the helium plasma was approximately 8 times less dense than the

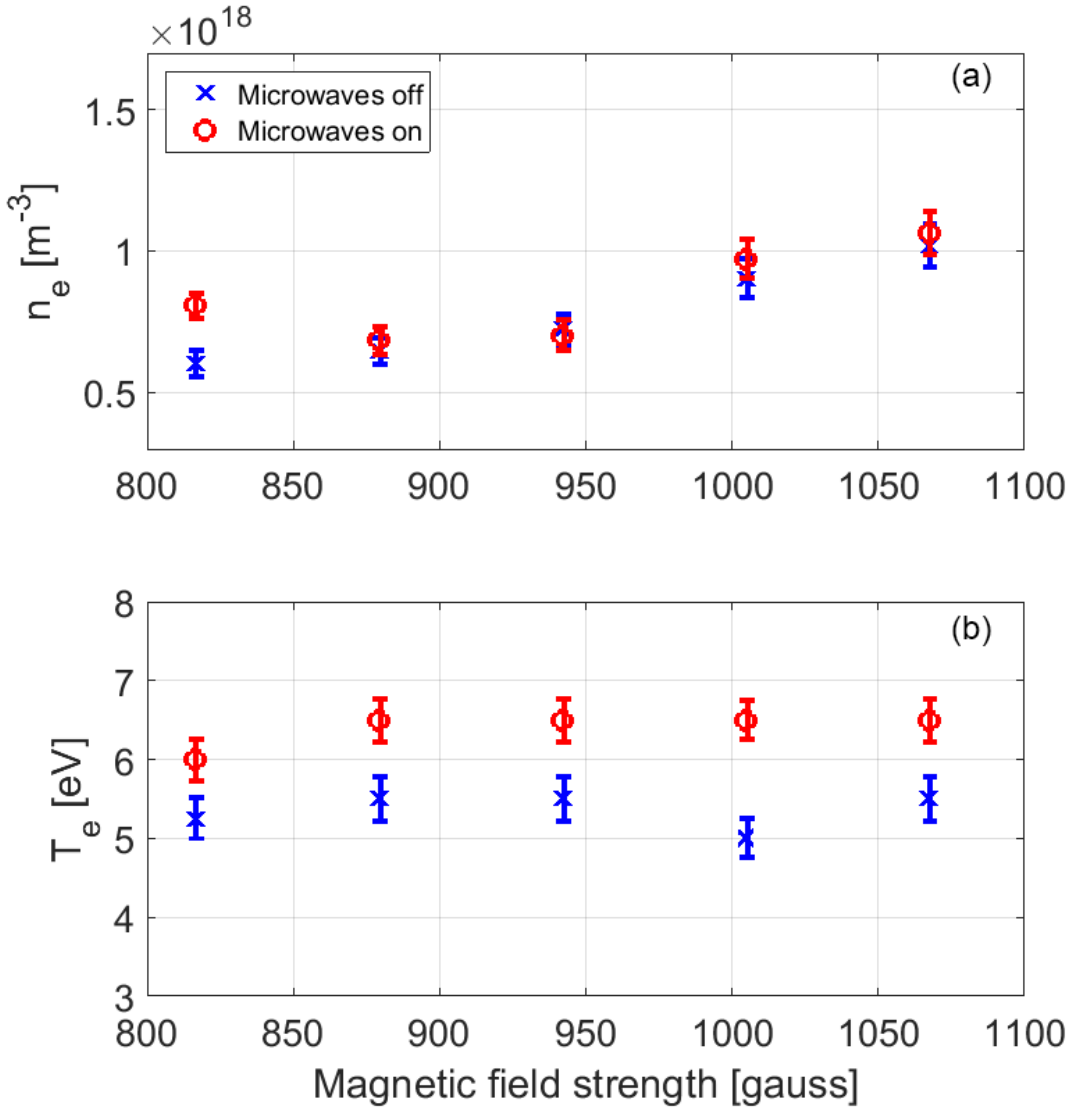

FIGURE 4.9: Langmuir probe traces in He of (a) electron density and (b) electron temperature for a scan of magnetic field strength for an RF power of 350 W for microwaves off (blue) and on (red).

argon plasma in the expansion chamber, the evanescent region for R waves was much smaller in helium than it was for argon discharges, as seen in Figure 4.2. Because of this more power was coupled to the plasma, contributing to a significant increase in helium ion density during the course of the microwave pulse. As the helium density increased in the expansion chamber, the R wave evanescent region grew in length (from Eq. (4.1)), and more power was reflected, as seen in Figure 4.13. The reverse power signal saturates at 1 kW in this figure as the diode can only measure up to 1 kW of power, though the microwave source outputs up to 1.2 kW.

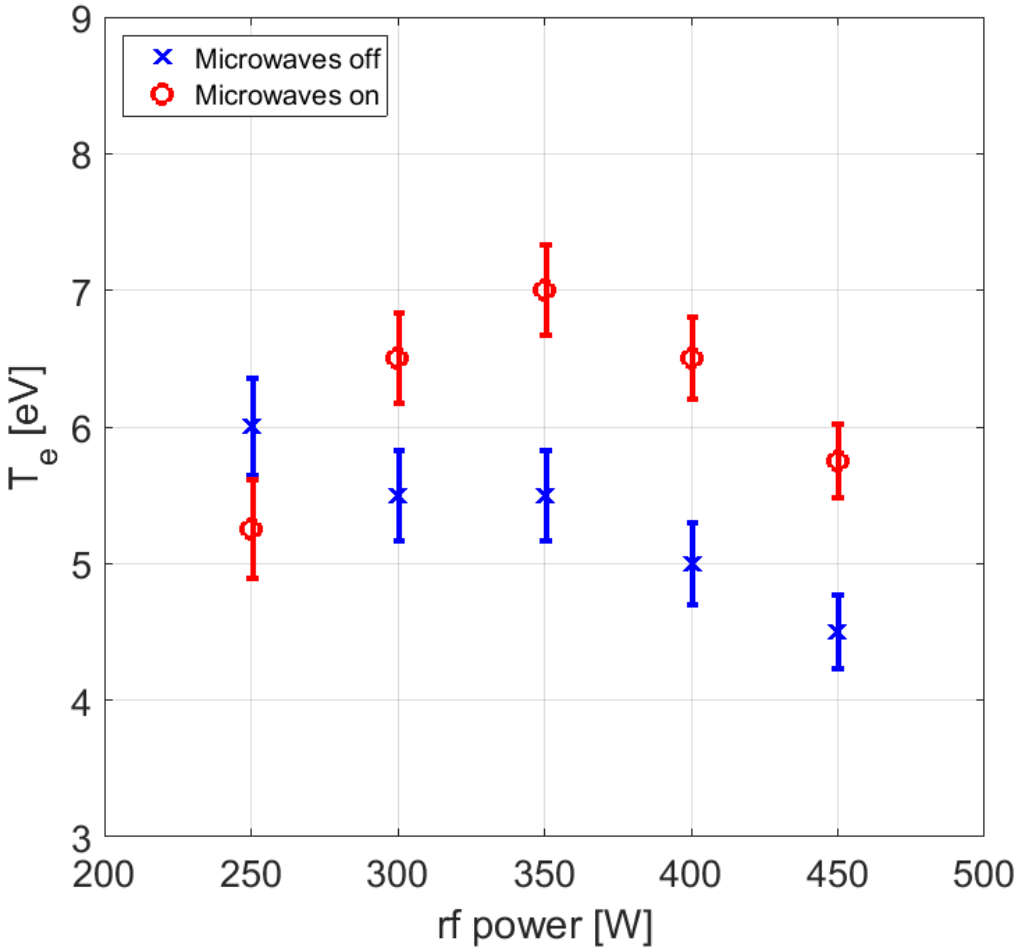

FIGURE 4.10: Langmuir probe traces in He of electron temperature over a scan of RF power for a magnetic field strength of 942 Gauss for microwaves off (blue) and on (red).

Unfortunately, an attentuator was not available to bring the reverse power signal fully in the range of the diode.

The increase in density observed in helium with the injection of microwave power can be understood both by the more power coupled to the ECR zone in helium versus argon, and by recognizing that unlike in argon, the helium electron impact ionization cross section, $\sigma_{iz}^{He} \sim 10^{-21}$ m^2, whereas the ground state to first excited state cross section $\sigma_{ex}^{1s\rightarrow 2s} \leq 10^{-22}$ m^2.[67,68] This is due to neutral helium having an ionization energy of approximately 25 eV, while the ground state He (II) requires 40.8 eV to be excited to a higher energy state. Thus, opposite to the ECR effects in argon, additional energy dumped into the electron tail first ionizes the neutrals

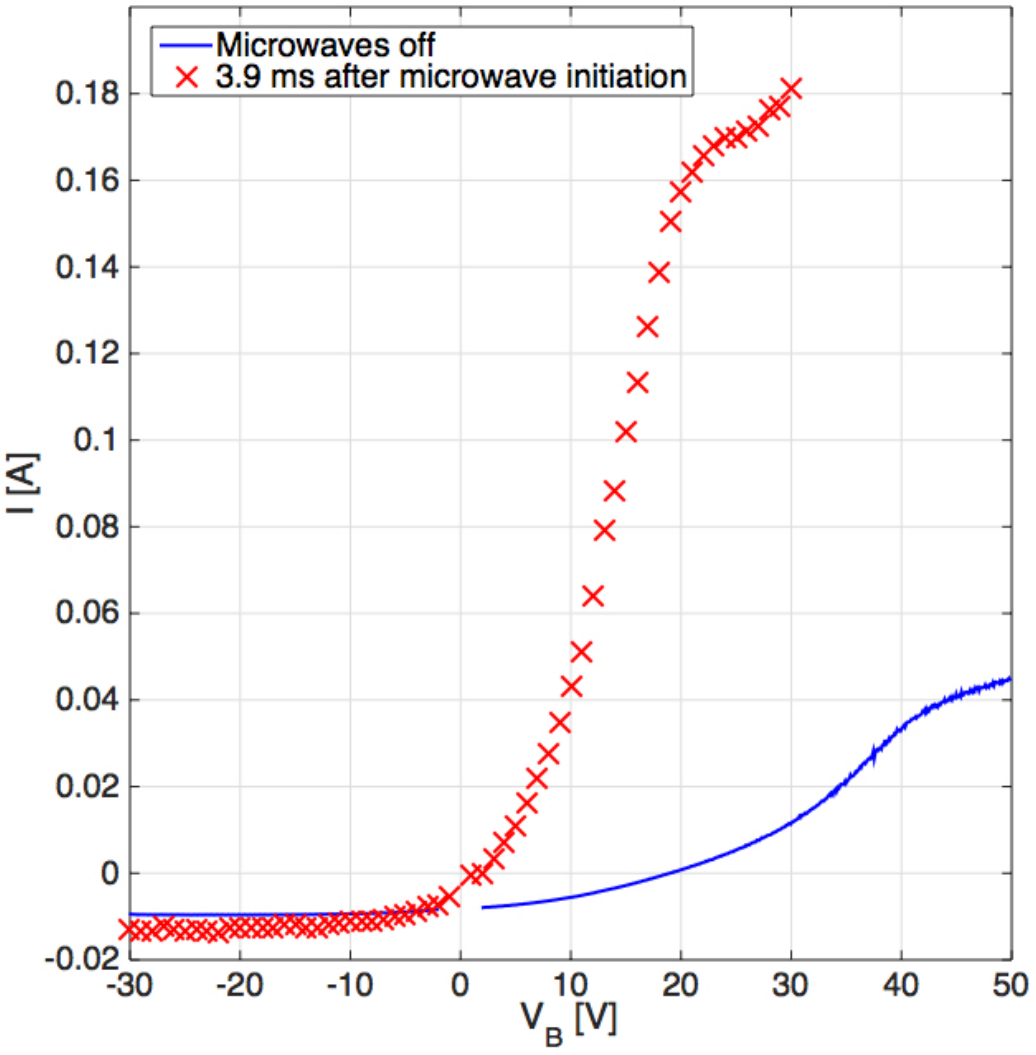

FIGURE 4.11: Representative Langmuir probe traces with (red) and without (blue) microwaves (3.9 ms into the microwave pulse) obtained in He for an electromagnet coil current of 375 A and an RF power of 350 W.

and then modestly increases the populations in excited electronic ion states. To understand the decay of the helium ion density back to the pre-microwave levels, the microwave forward power pulse shape must be known. The decay of the density occurs over a few ms. The shortest helium ion confinement time, τ_c, is controlled by helium ion losses to the walls intersecting the magnetic field lines. Thus, the confinement time is given by $\tau_c \approx L/v_i \approx L/\sqrt{T_i/M_i}$, where L is the length of the expansion chamber, T_i is the ion temperature, and M_i is the ion mass. T_i is unknown (because helium TALIF is not yet a working diagnostic) but typical ion temperatures are less

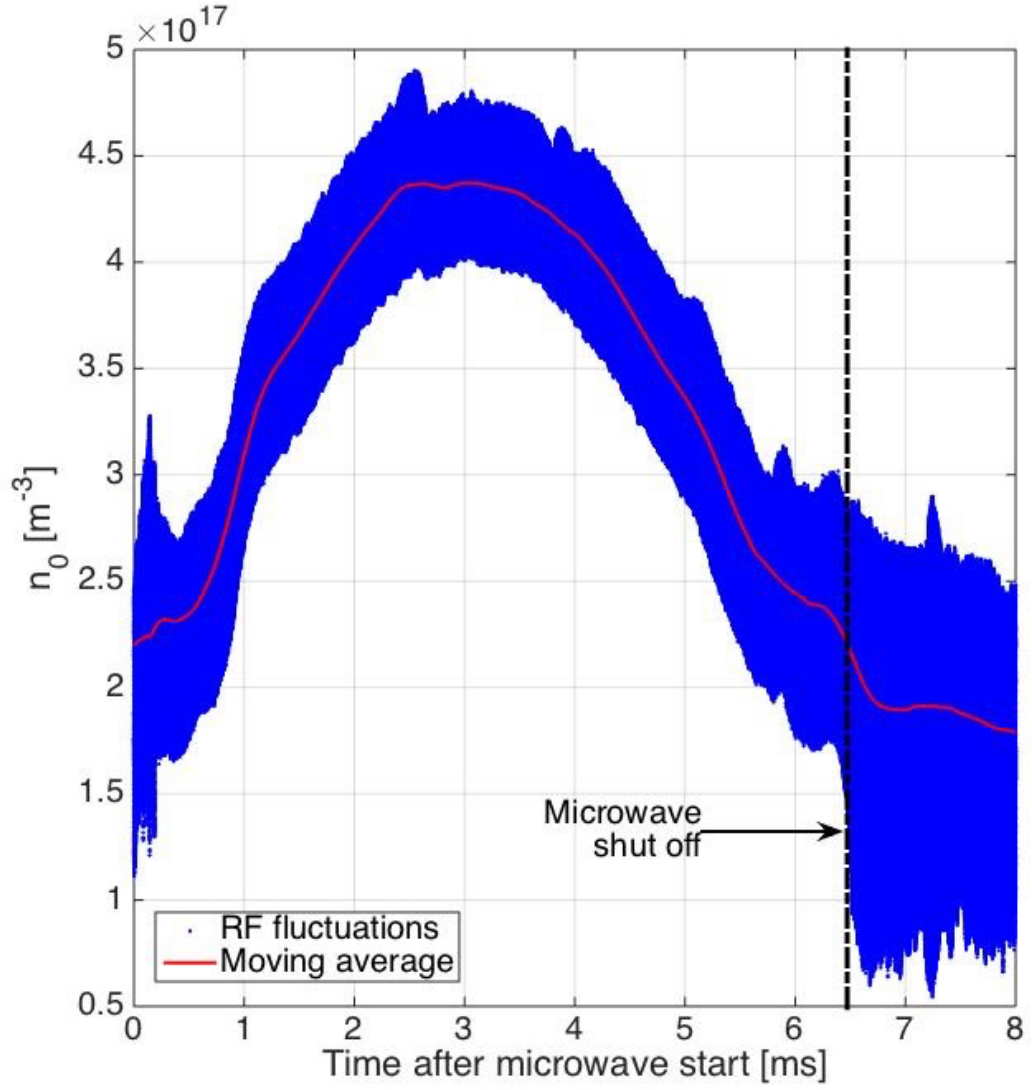

FIGURE 4.12: Time resolved He plasma density after microwave initiation for an electromagnet coil current of 375 A and an RF power of 350 W.

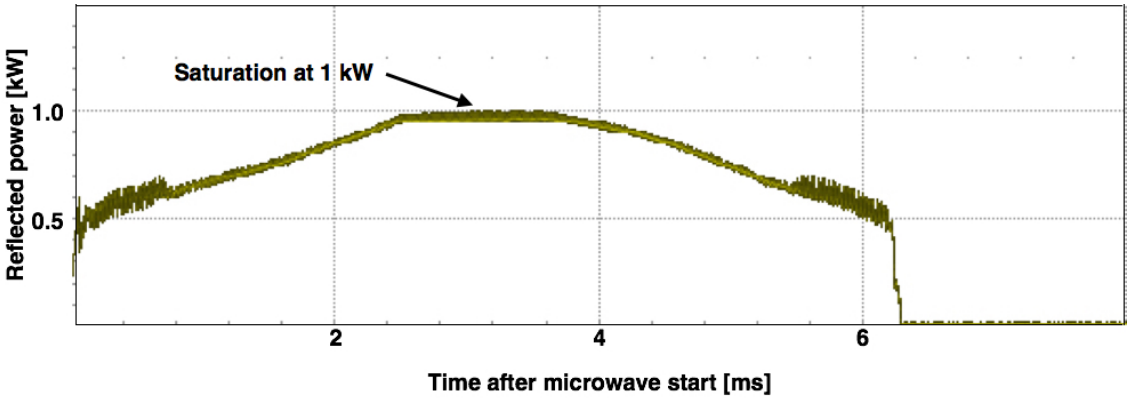

FIGURE 4.13: Reflected power signal in He plasma for an electromagnet coil current of 375 A and an RF power of 350 W.

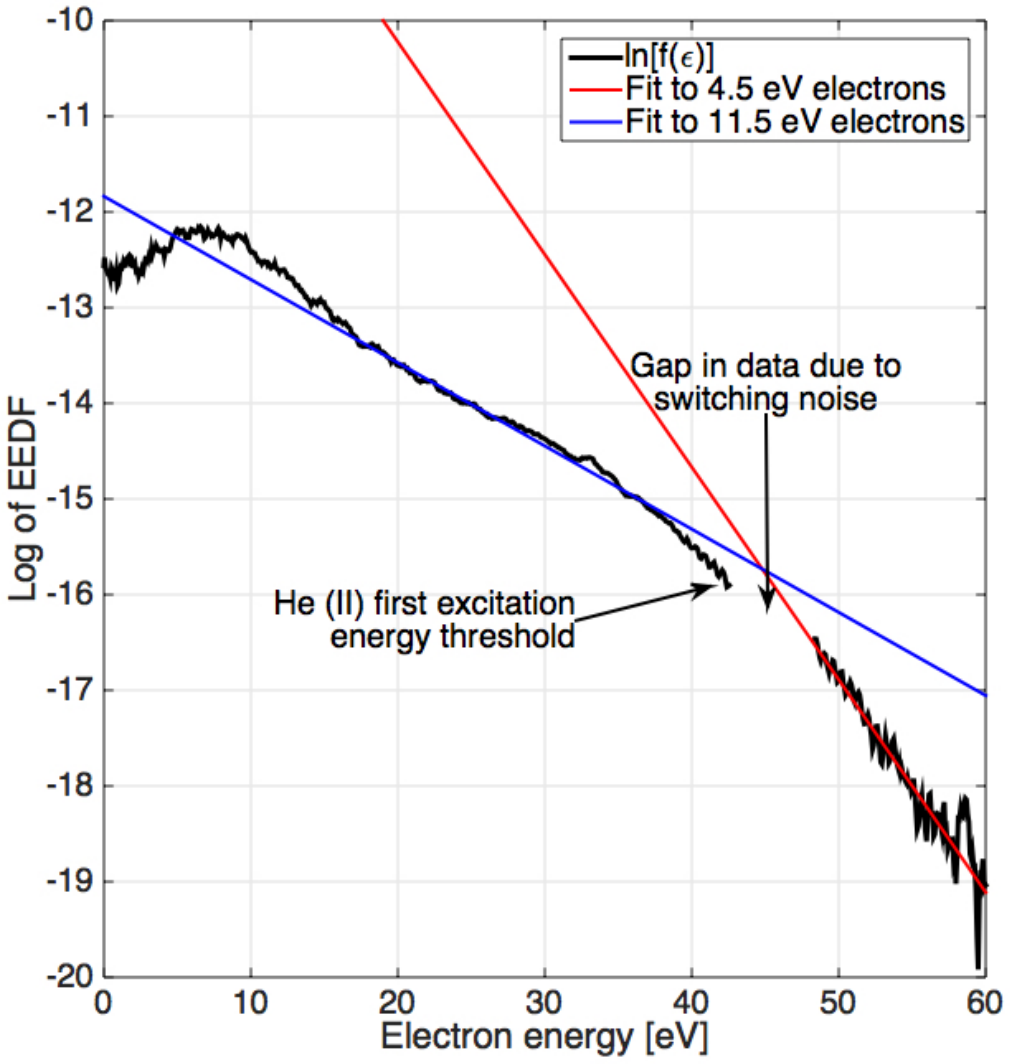

FIGURE 4.14: Log of EEDF measured by a Langmuir probe in He plasma without microwave injection.

than 1 eV in these systems.[26] Using an estimate of $T_i \approx 0.5$ eV, $\tau_c \approx 40\mu$s $\ll 1$ ms, meaning He ion diffusion cannot account for the observed rate of plasma density decay. Unfortunately, the microwave circulator did not allow for forward power monitoring, so we are unable to fully understand our helium density decay rates as the microwaves turn off. Ultimately, there is some microwave power injected during the entirety of the pulse. Simple confinement models are not sufficient to explain the decay and a full understanding of the full forward microwave power pulse shape is still needed.

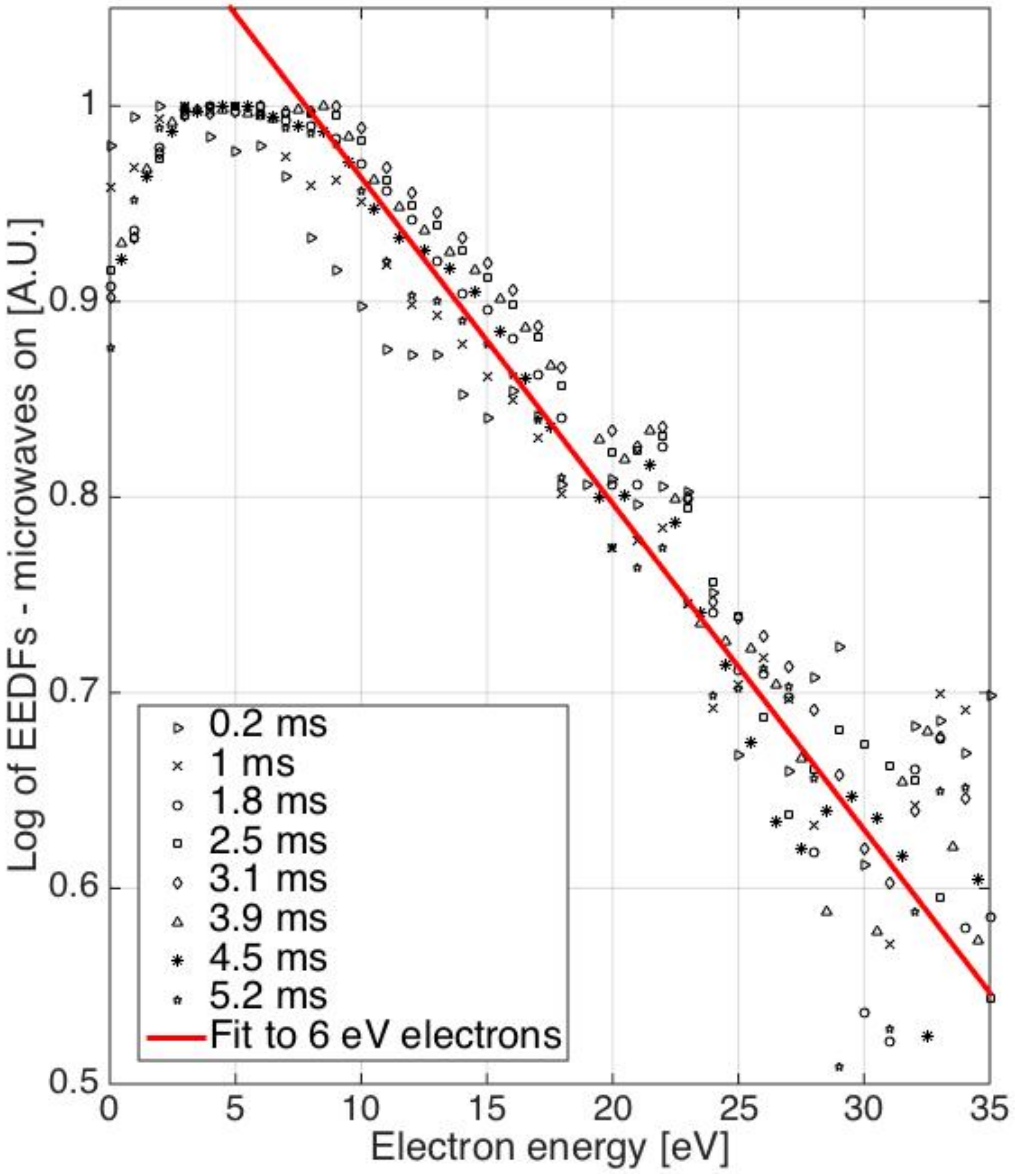

FIGURE 4.15: Log of EEDFs measured by a Langmuir probe in He plasma at different times after initiation of microwave injection for an electromagnet coil current of 375 A and an RF power of 350 W.

Figures 4.14 and 4.15 show the log of the EEDF amplitude obtained from the Langmuir probe traces with and without microwaves. Because of the low voltage resolution of the high-time resolution method for acquiring the Langmuir probe data during a microwave pulse, only the bulk energy population (10 to 30 eV) of electrons is resolvable for measurements during the microwave pulse. As a result, the energy range for Figure 4.15 ends at 35 eV (increasing noise levels are apparent from 30 to 35 eV in the measurements). For the case without microwaves, averaging over many high voltage resolution Keithley traces allowed EEDFs to be faithfully measured up to electron energies of 60 eV (Figure 4.14). The bulk of the electron population fits with a single Mawellian distribution with a temperature of 11.5 eV. Above 40 eV, the EEDF is noticeably depleted. The high-energy portion of the EEDF fits with a Maxwellian with a 4.5 eV temperature. Since the helium ions first excited state is 40.8 eV above its ground state, the high energy tail depletion is likely due to inelastic electron collisions with ground state helium ions.

To compare the estimated power absorbed in the resonance zone with the estimated power transmitted to the ECR location, the same analysis used for argon discharges is performed. First, the EEDFs with and without microwave injection are fit with the analytic expression of Eq. (4.10). For the microwaves off trace, the fitting constants were $A = 1$, $B = 0.23$, $T_1 = 4.7$ eV and $T_2 = 11.5$ eV. For the microwaves on trace, $A = 1$, $B = 0.73$, $T_1 = 4$ eV and $T_2 = 6$ eV. The latter trace was taken 3.9 ms after microwave initiation. The EEDFs plotted on a linear scale and their fits are shown in Figure 4.16. For helium, the density in the expansion chamber before and after the microwave input was significantly different. Therefore, Eq. (4.5) must be be revised to include the changing density term:

$$P_{abs} \approx \frac{(\overline{\epsilon}_{on} n_{on} - \overline{\epsilon}_{off} n_{off})V}{\Delta t}, \tag{4.15}$$

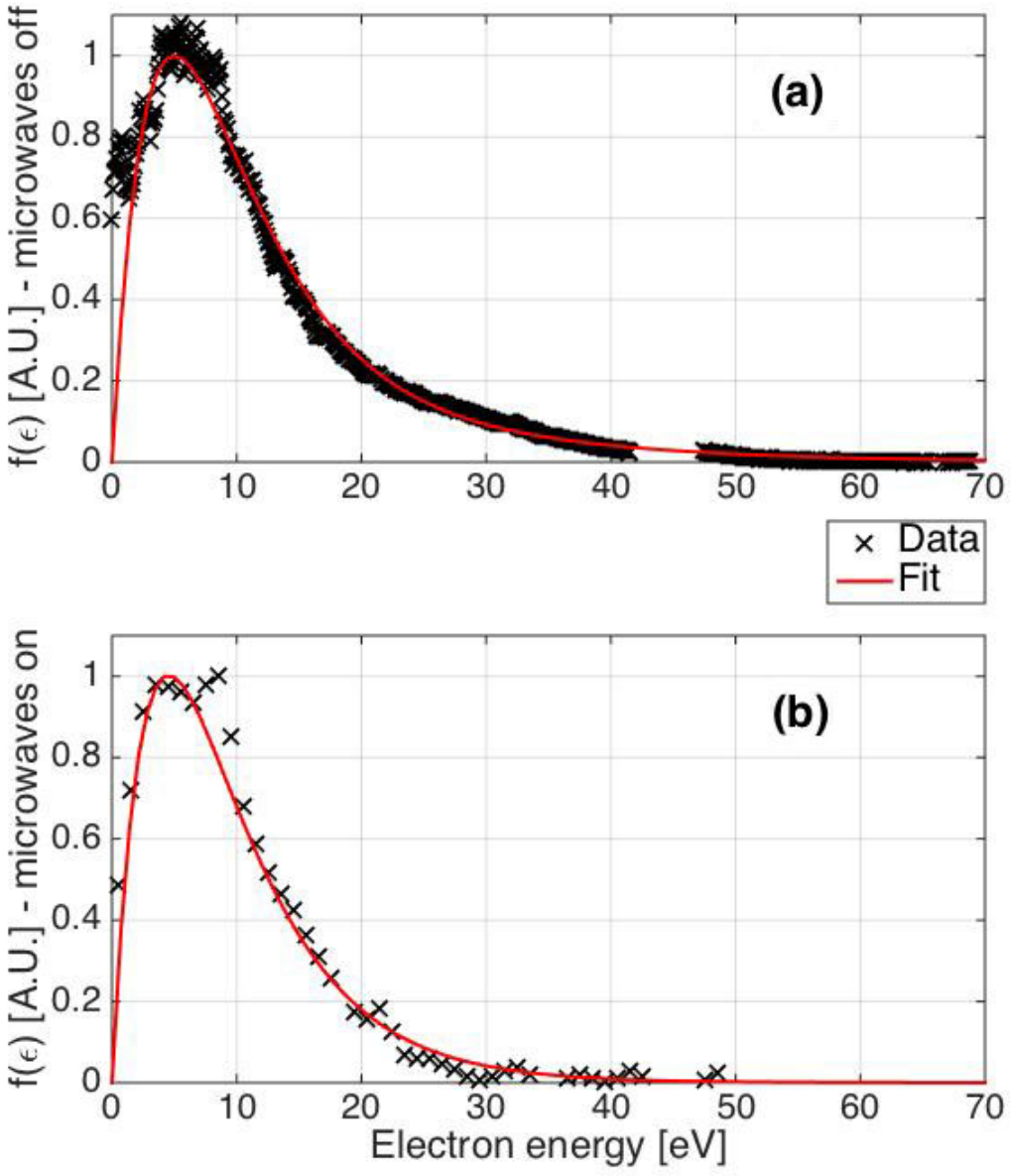

FIGURE 4.16: EEDFs measured by a Langmuir probe in a He plasma (a) without and (b) with microwaves 3.9 ms after microwave injection begins for an RF power of 350 W.

where n_{on} and n_{off} are the density in the expansion chamber with and without microwave injection. Then, following the same sequence of steps as for the previous calculation for argon and using the n_{on} data from the peak of the density versus the time profile, we calculate that the absorbed power is approximately 180 W. Comparing this with the estimated 150 W available to the plasma after tunneling through the evanescent region from section 4.2, the two results are in reasonable agreement. The agreement in values suggests that our assumed estimate for the helium density profile in Figure 4.2 yields the correct power injected into the ECR zone. With the addition of microwaves the bulk electrons cool to 6 eV. This cooling occurs rapidly compared to the microwave pulse period. Figure 4.15 shows EEDFs, normalized to their maxima plotted on a log scale, taken at seven different times after the microwave pulse initiation, overlaid on top of one another.

While the ion density increases in time during the course of a microwave pulse period (see Figure 4.12), the bulk population temperature remains at 6 eV for the entirety of the pulse. The temperature cools to 6 eV as quickly as 0.2 ms after the microwaves are applied. The observed cooling of the bulk population may be due to the creation of cold electrons from the electron impact ionization of He (I) by the energetic ECR electrons. The fast ECR electrons that have inelastically collided with neutrals and ions will also lose energy and contribute to the cooling of the bulk population. In general, changes to the EEDF due to ECR electrons will occur on the timescale $\Delta t \approx 10$ ns (from Eq. (3.6)) and the changes in density will occur on the timescale $\tau_{iz} = 1/\nu_{iz} \approx 1/(n_n \sigma_{iz} v_e) \approx 1\mu$s, where τ_{iz}/ν_{iz} is the ionization time/frequency in helium, and σ_{iz} is the helium electron impact ionization cross section.[68] From these estimates it is clear that changes in the EEDF occur more rapidly than the changes in density levels. However, the precise reasons for the shape of the EEDF requires knowledge of the shape of the forward microwave pulse power. The EEDF changes from the no-microwaves case shown in Figure 4.14 to the microwaves-on case shown in Figure 4.15 more quickly than the plasma

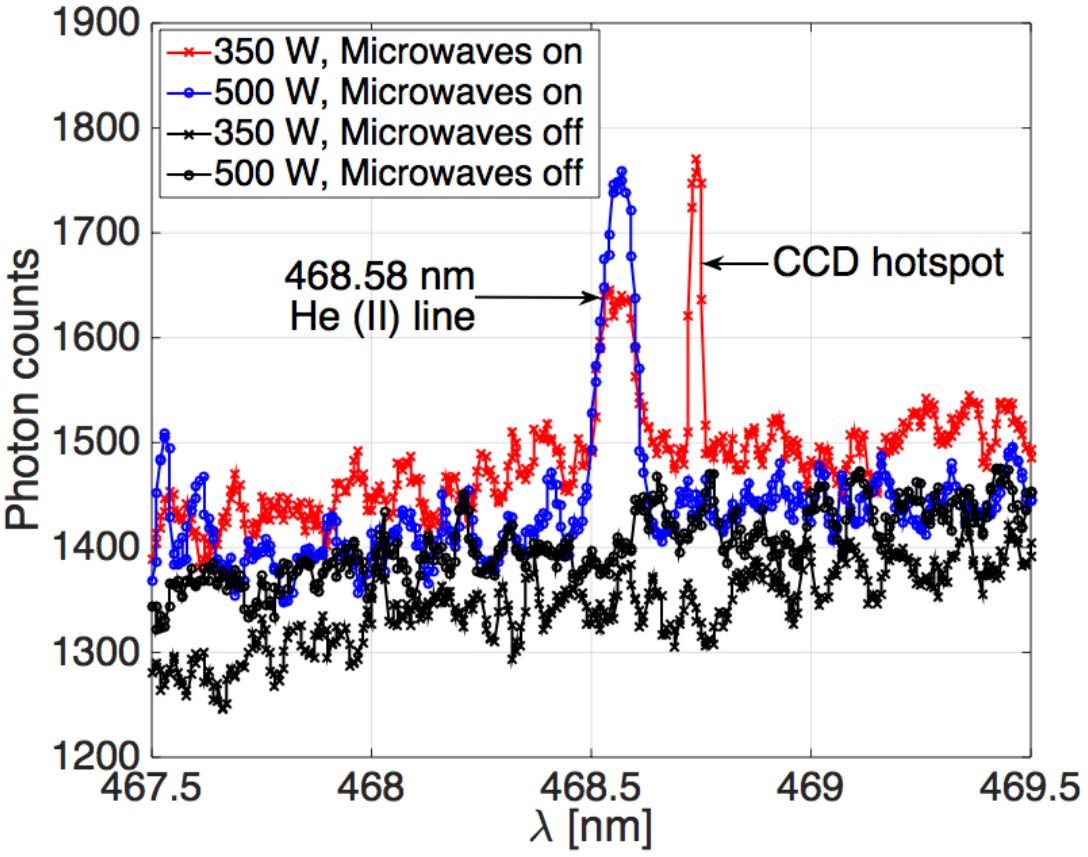

FIGURE 4.17: He emission spectra at 468 nm with and without microwaves for RF powers of 350 W and 500 W. Note the appearance of artificial peak in the emission spectrum that appears for the lower RF power case when the microwave source is on.

density changes. The changes in the EEDF are symmetric about the center of the microwave pulse indicating that the change in the EEDF shape and the change in density level, although coupled, are ultimately controlled by the amount of microwave power injected, which depends on the (unfortunately) unknown forward pulse shape.

Figures 4.17 and 4.18 show emission spectra collected around 468 nm and 656 nm in helium with and without microwave injection. Two helium ion lines are observed when microwaves are injected, the $n = 4 \rightarrow 3$, 468.58 nm line and the $n = 6 \rightarrow 4$, 656.02 nm line. These upper excited helium ion states require collisions with electrons at energies in excess of 40.8 eV and are therefore difficult to observe in low temperature plasmas. To improve signal-to-noise, a 5 min plasma on integration of the spectrometer CCD was performed, and then a 5 min dark

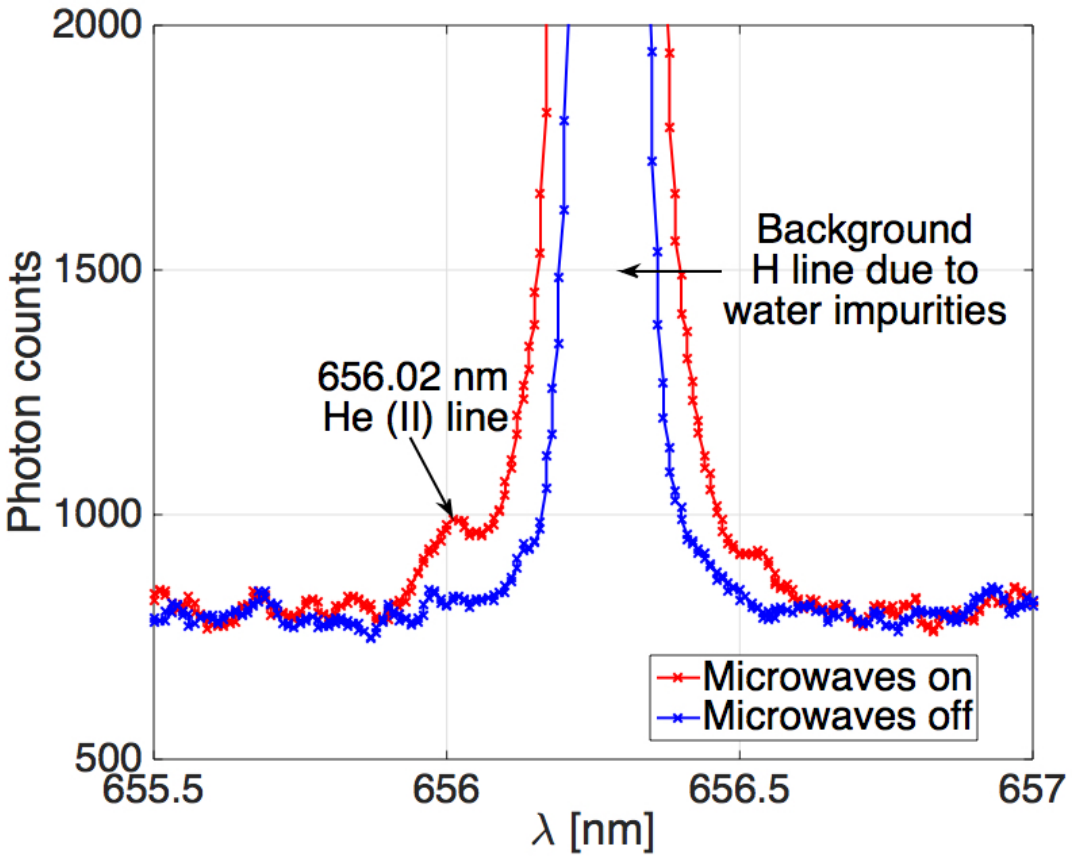

FIGURE 4.18: Helium emission spectra around 656 nm with and without microwaves for an RF power of 350 W. Note that the He line is the small bump to the left (at 656.02 nm) of the very large hydrogen line at 656.28 nm that appears when the microwaves are on.

exposure was subtracted. Still, only a few hundred counts of ion emission were recorded above the dark CCD and background noise level. Nevertheless, the mere presence of these lines is extremely important. To achieve TALIF in a helium plasma, electrons energetic enough to populate the $n = 2$ ion state must exist. Observing ion lines from excited states at energies above the $n = 2$ level suggests that the $n = 2$ state is also being populated. Figure 4.17 shows that the 468 nm line intensity increases with increasing RF power due to increase in overall ion density. However the line only appears with the injection of microwave power, suggesting the microwave heating mechanism more effectively energizes the high-energy electrons.

The very weak (in comparison to the intense hydrogen line at 656.28 nm) He ion line at 656.02 nm only appears when the microwave power is on. That $n = 6$ states are populated

at all in plasma with a bulk electron temperature of 6 eV is remarkable. Were it possible to perform time-resolved EEDF measurements with high enough voltage resolution to observe the EEDF at energies above 30 eV, it is likely that the depleted portion of the EEDF seen in the microwave off measurements would be enhanced when the microwaves are on.

Chapter 5

X-wave Injection

5.1 X-wave Apparatus and Diagnostics

In these experiments, X-wave microwave injection into a helicon plasma was performed to increase the total power coupled into the plasma (compared to R-wave injection) and to take advantage of the spatial localization of X-wave absorption to target specific regions of the plasma for later spectroscopic study. The R-wave microwave injection experiments demonstrated that microwave heating of helicon plasmas enhanced the high energy tail of the EEDF in argon plasmas while keeping other parameters, like the total particle density, constant. Other helicon source groups have also demonstrated electron heating in argon helicon plasmas with the addition of up to 5.5 kW of R-wave microwaves. In very low pressure argon helicon plasmas, < 0.2 mTorr, *Zalach et al.* report less than a 1 eV increase in the electron temperature with addition of microwave power until the R-wave power was increased to 5.5 kW. For 5.5 kW of R-wave power, they observed a roughly 1 eV jump in electron temperature.[69] However, for our lower power R-wave injection experiments in helium plasmas, there was little change in the population of the excited helium ion states that are needed for TALIF measurements.

In these X-wave studies, the argon experiments were performed at an operating pressure of 6.5 mTorr and the helium experiments were performed at an operation pressure of 20 mTorr (the higher helium pressure is required to initiate breakdown with the helicon antenna). Microwaves were again injected through the vacuum sealed quartz microwave window but this time the window was placed on the side of the expansion chamber. In addition to Langmuir probe measurements of the electron temperature, in these experiments the electron temperature in argon plasmas was also determined spectroscopically from the intensity ratio of two closely spaced emission lines (to avoid the need to perform a calibration of wavelength dependent efficiency of the spectrometer). These specific lines were selected because their ratio depends strongly on electron temperature but is relatively insensitive to the plasma density.

The intensity ratio as a function of electron temperature is calculated from a collisional radiative model that employs line strengths obtained from the Atomic Data and Analysis Structure (ADAS) suite of codes.[70] ADAS is an open source set of codes and data sets for modelling ion and atom radiation in plasmas. Shown in Fig. 5.1 is the line intensity ratio for the 750.593 nm and 751.672 nm lines of neutral argon as a function of electron temperature. Note that the curve shown in Fig. 5.1 is an overlay of the ratios calculated for plasma densities ranging from 2.5 to 3.5 $\times 10^{12}$ cm^{-3} but only the top plot is visible with the rest obscured behind it. Based on the line ratio predicted by the model, a measured line ratio of 1.14 corresponds to an electron temperature of 1.14 eV. The equality of ratio value to T_e is coincidental, and not usually 1-to-1.

As in the R-wave studies, OES measurements are also used to verify the existence of excited argon and helium ion electronic states. The intensity of emission from different energetic electronic states provides evidence that modifications to the EEDF result in populations of excited and metastable ion states that could be investigated with LIF or TALIF techniques.

The Langmuir probe was inserted with the tip at 13.5 cm from the glass to expansion

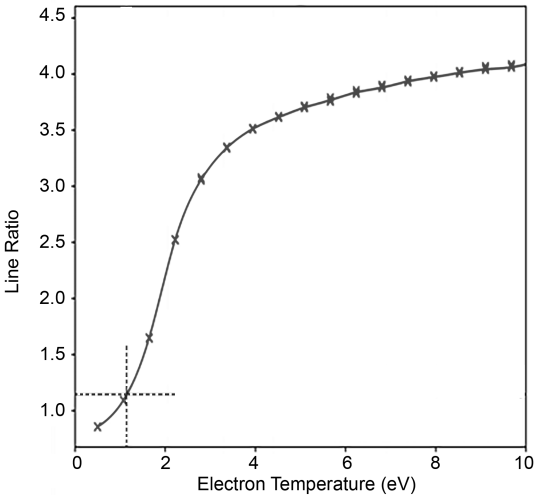

FIGURE 5.1: The predicted line intensity ratio for the 750.593 nm and 751.672 nm lines of neutral argon as a function of electron temperature according to a collisional radiative model based on the ADAS line intensity calculations. Line ratio curves are shown for multiple plasma densities ranging from $2.5 - 3.5$ x 10^{12} cm^{-3}.

chamber interface (see Figure 2.2). As in the R-wave studies, the Druyvesteyn method of probe trace derivatives was used to obtain the electron temperature and the EEDF.[46]

5.2 X-wave Microwave Injection

The injection waveguide is oriented such that the microwaves propagate perpendicular to the background magnetic field with the wave electric field polarized perpendicular to the background magnetic field, i.e., extraordinary, X, mode waves. The cold plasma dispersion relation for X mode waves is

$$n^2 = \frac{k^2c^2}{\omega^2} = \frac{\left(\omega^2 + \omega\omega_{ce} - \omega_{pe}^2\right)\left(\omega^2 - \omega\omega_{ce} - \omega_{pe}^2\right)}{\omega^2\left(\omega^2 - \omega_{ce}^2 - \omega_{pe}^2\right)} \tag{5.1}$$

with a resonance at

$$\omega_h = \sqrt{\omega_{ce}^2 + \omega_{pe}^2} \tag{5.2}$$

and cutoffs at

$$\omega_L = \frac{1}{2}\left[-\omega_{ce} + \left(\omega_{ce}^2 + 4\omega_{pe}^2\right)^{\frac{1}{2}}\right] \tag{5.3}$$

and

$$\omega_R = \frac{1}{2}\left[\omega_{ce} + \left(\omega_{ce}^2 + 4\omega_{pe}^2\right)^{\frac{1}{2}}\right], \tag{5.4}$$

where n is the index of refraction, k is the wavenumber of the wave, c is the speed of light, ω is the wave frequency, $\omega_{ce} = eB/m_e$ is the electron cyclotron frequency for a magnetic field strength B, and the plasma frequency is $\omega_{pe}^2 = 4\pi n_e e^2/m_e$. The resonant frequency is the upper hybrid frequency, ω_h, and the cutoffs ω_R and ω_L are for left and right circularly polarized waves, respectively. For a microwave frequency of 2.45 GHz and the argon and helium plasma densities used in this study, the electron-electron and electron-ion collision frequencies are orders of magnitude smaller than the microwave frequency. Therefore, collisions have been ignored in the dispersion relation.

The calculated squared index of refraction is shown in Fig. 5.2b for the measured plasma density profile shown in Fig. 5.2a and the magnetic field at the axial position of the waveguide. The helicon source tube has a radius of 2.5 cm, so any plasma that appears beyond 2.5 cm arises from cross field transport in the expansion region. Measurements end at $r \sim 6$ cm because beyond that the density is too small for reliable Langmuir probe measurements. There are two clear regions of negative squared index of refraction (evanescent propagation) and a resonance around a radial location of 2.5 cm. Therefore, for X-mode microwaves to reach the resonance layer in a plasma with a peak density of 2×10^{12} cm^{-3}, they would have to tunnel through a narrow evanescent region. The measured plasma density profiles for argon plasmas in CHEWIE as function of RF power are shown in Fig. 5.2c. In all cases, the simple cold plasma dispersion relation (Fig. 5.2d) predicts that X-mode waves will never reach a resonant layer because the plasma is overdense for the given microwave frequency and local magnetic field strength. For argon plasmas, we should not expect to see significant electron heating for X-wave injection. Note that in our previous studies in which microwaves were injected along the magnetic field (as

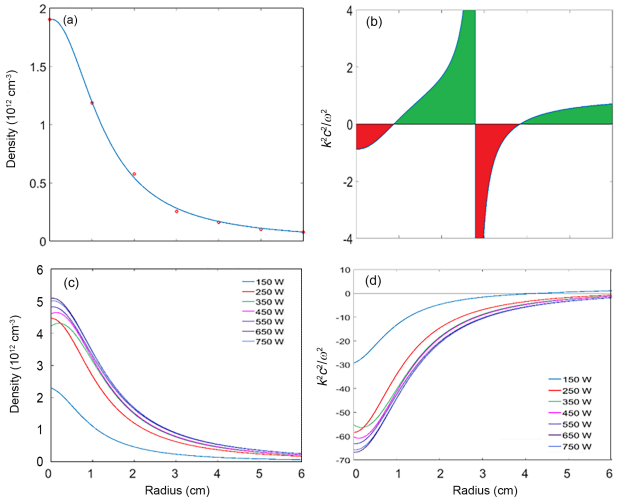

FIGURE 5.2: For a source magnetic field of 850 G (a) a typical helium plasma density profile in the expansion chamber. (b) The squared index of refraction ($n^2 = k^2c^2/\omega^2$) in helium plasma. The X-wave propagates in the green region and is evanescent ($n^2 < 0$) in the red region. (c) Argon density profiles for different RF powers. (d) The squared index of refraction (n^2) for different RF powers based on the measured density profiles. There is no region of propagation for X-waves ($n^2 < 0$ everywhere).

R-waves), significant, but not large, electron heating at the cyclotron resonance was observed for argon plasmas and very weak heating was observed in helium plasmas.[71] Since electron heating in helium plasmas was desired, the experiment was reconfigured to permit X-mode injection.

The calculated squared index of refraction for helium plasmas in CHEWIE plasmas is shown in Fig. 5.3 for different helicon source RF powers. Because of the lower overall density of helium helicon plasmas, a resonance appears in the plasma at the upper frequency and if the X-mode microwaves are able to tunnel through the thin evanescent region, some microwave energy should be deposited in the plasma. The predicted location for the resonance moves radially outward with increasing RF power.

5.3 X-wave Effects in Argon

Langmuir probe measurements of the electron temperature radial profiles are shown in Fig. 5.4 for three different RF powers. Measurements with and without the microwave system turned

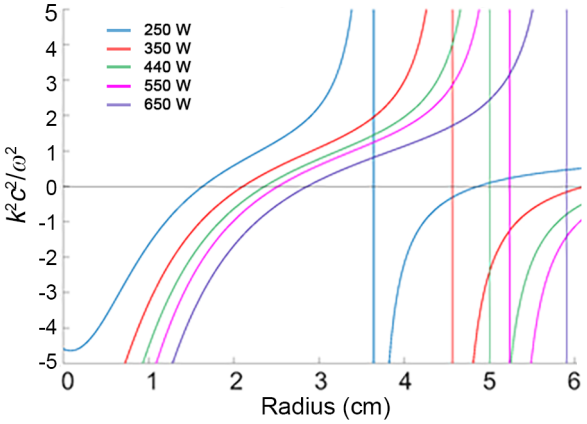

FIGURE 5.3: For a source magnetic field of 850 G, the calculated squared index of refraction ($n^2 = k^2c^2/\omega^2$) for helium plasma as a function of helicon source RF power as a function of radial location. There are clear regions of X-wave propagation ($n^2 > 0$) and an upper hybrid resonance for all RF powers.

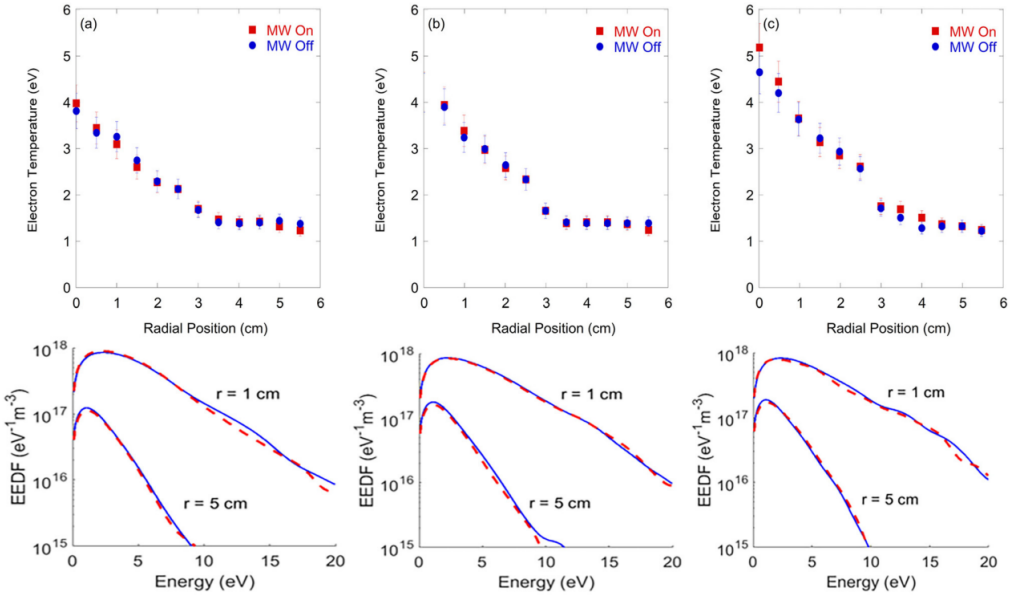

FIGURE 5.4: Electron temperature in argon plasma (from Langmuir probe measurements) versus radial location for three different RF powers (a) 250 W, (b) 450 W, and (c) 650 W with (red squares) and without (blue circles) microwaves. Below each radial profile, the electron energy distribution function (EEDF) obtained from a Druyvesteyn analysis for the same RF powers with (red dashed lines) and without (blue solid lines) microwaves are shown for two different radial positions.

on are shown. Also shown are EEDF measurements for all three RF powers (250, 450, and 650 Watts) and both microwave powers (on and off) for two different radial locations (1 cm and 5 cm). The electron temperature profile peaks at 4 eV on axis and drops rapidly to 1 eV by $r =$ 3.5 cm. Outside of 3.5 cm, the electron temperature is constant at roughly 1 eV. Near the axis

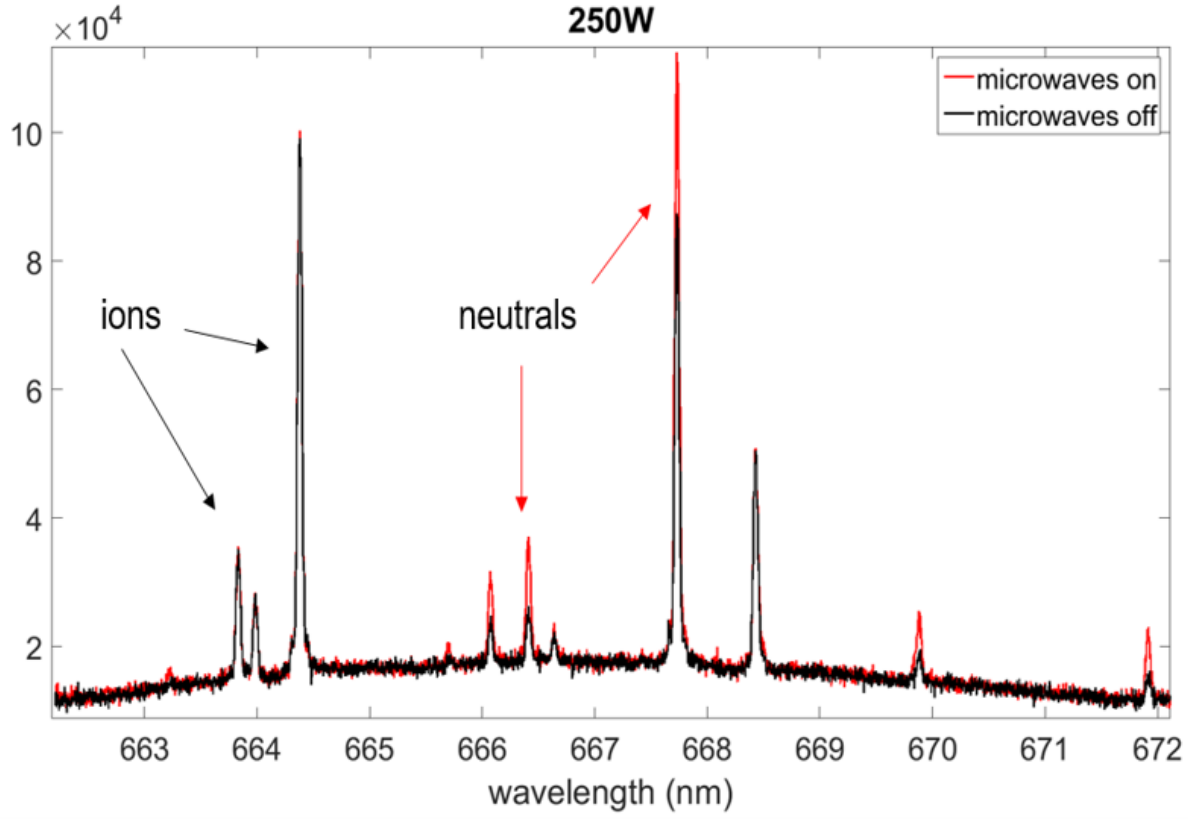

FIGURE 5.5: The argon emission spectrum for an RF power of 250 W with (red) and without (black) microwave injection. The spectrum includes emission from both neutral argon and argon ions.

(r = 1 cm), the log of the EEDF is linear from 5 to 20 eV, indicative of a single Maxwellian velocity distribution. Further out (r = 5 cm), the EEDF remains Maxwellian but reaches the noise floor in the measurement by 9 eV consistent with a much colder electron population. The key feature in all the measurements is the clear lack of any electron heating or enhancement of the EEDF at any energy when the microwaves are injected into the argon plasma.

OES measurements of neutral argon and argon ion emission paint a similar picture of the effects of microwave injection. Shown in Fig. 5.5 is the emission spectrum around 667 nm for an RF power of 250 Watts. The neutral lines show a clear increase in intensity with the microwave injection, while the ion lines are unchanged with the injection of microwaves. The OES measurements are line integrated and therefore contributions from the edge of the plasma, where neutrals dominate, are added to the contributions from the ions, which are largest near

the center of the plasma. It is likely that the increase in neutral line emission reflects deposition of microwave energy at the periphery of the plasma consistent with the lack of observed electron heating for $r < 6$ cm.

Corroborating the probe measurements which show no change in electron temperature with microwave injection are electron temperatures determined from the argon neutral line ratio per Fig. 5.1. Shown in Fig. 5.6a are measurements of the electron temperature from the ratio of the line-of-sight integrated intensities of the neutral argon 750.593 nm and 751.672 nm lines. As expected, the neutral line intensity ratio method yields electron temperatures consistent with the Langmuir probe derived electron temperatures in the outer region of the plasma for the same RF power (roughly 1.5 eV). For most RF powers, there is no change in the electron temperature with and without the microwaves. The line ratio method is extremely sensitive to the highest energy portion of the EEDF and there might be a statistically significant increase in the electron temperature for the lowest RF power case shown in Fig. 5.6a. This is consistent with Fig. 5.5, which showed some increase in neural argon line emission at low RF powers most likely limited to the periphery of the plasma.

5.4 X-wave Effects in Helium

The electron heating results are very different for helium plasmas. Shown in Fig. 5.7 are Langmuir probe measurements of the electron temperature radial profiles in helium plasmas for three different RF powers. Measurements with and without the microwave system turned on are shown. Also shown are EEDF measurements for all three RF powers (250, 450, and 650 Watts) and both microwave powers (on and off) for two different radial locations (1 cm and 5 cm). For all three RF powers, there is a nearly 1 eV increase in the electron temperature around $r = 2.5$ cm.

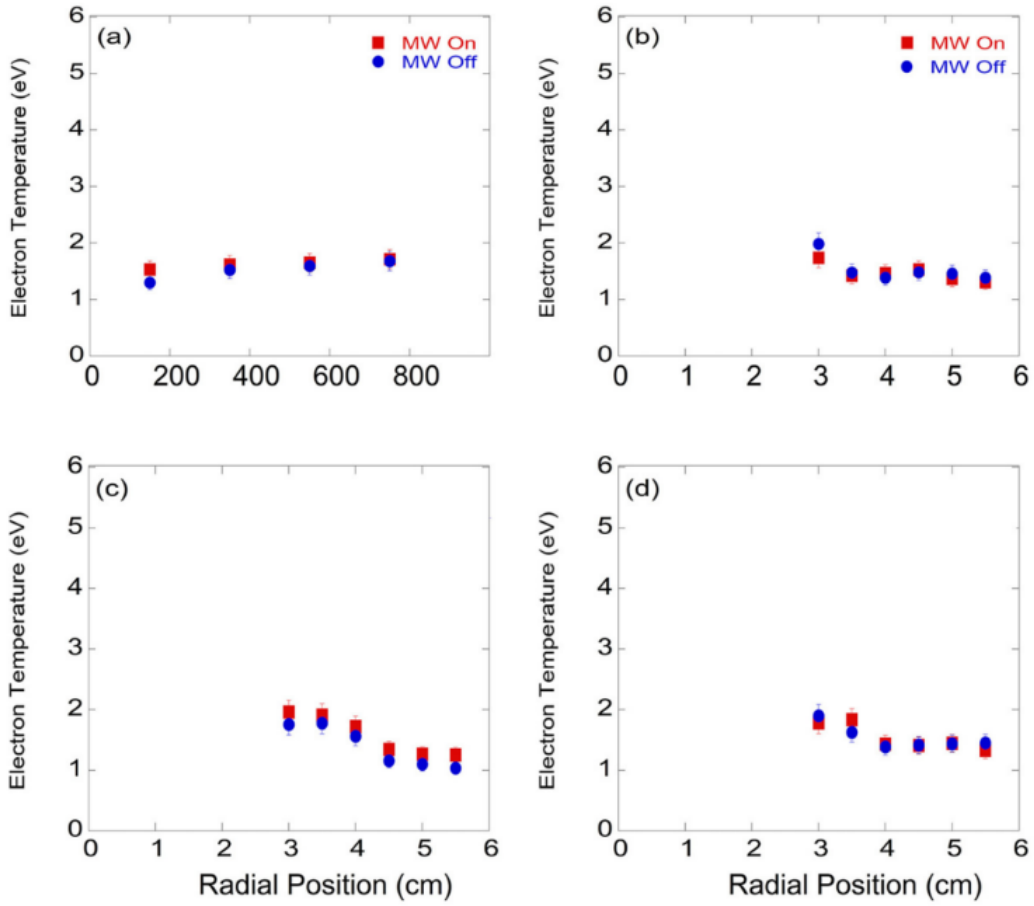

FIGURE 5.6: (a) Argon electron temperature determined from neutral line emission ratio for four different RF powers with (red) and without (blue) microwaves. (b) The Langmuir probe measured electron temperature for an RF power of 350 Watts as a function of radial location. (c) The Langmuir probe measured electron temperature for an RF power of 550 Watts as a function of radial location. (d) The Langmuir probe measured electron temperature for an RF power of 750 Watts as a function of radial location. The emission based electron temperatures are generally consistent with the probe measurements around $r \sim 3.5$ cm.

The EEDFS at both locations shown ($r = 1$ cm and $r = 5$ cm) are clearly not describable with a single Maxwellian energy distribution. Enhancement of the high energy tail of the EEDF is typical in helicon sources.[14] As the RF power increases, a discontinuity in the EEDF shifts from roughly 12 eV at an RF power of 250 W to roughly 7 eV for an RF power of 650 W. The portion of the EEDF above this breakpoint energy decreases in amplitude with the introduction of X-wave microwaves. Further out from the CHEWIE axis ($r = 5$ cm) the changes in the EEDF are dramatic. For nearly all energies, there is significant increase in the EEDF amplitude and the slope of the EEDF decreases (electron temperature increases). The EEDF at $r = 3$ cm for an

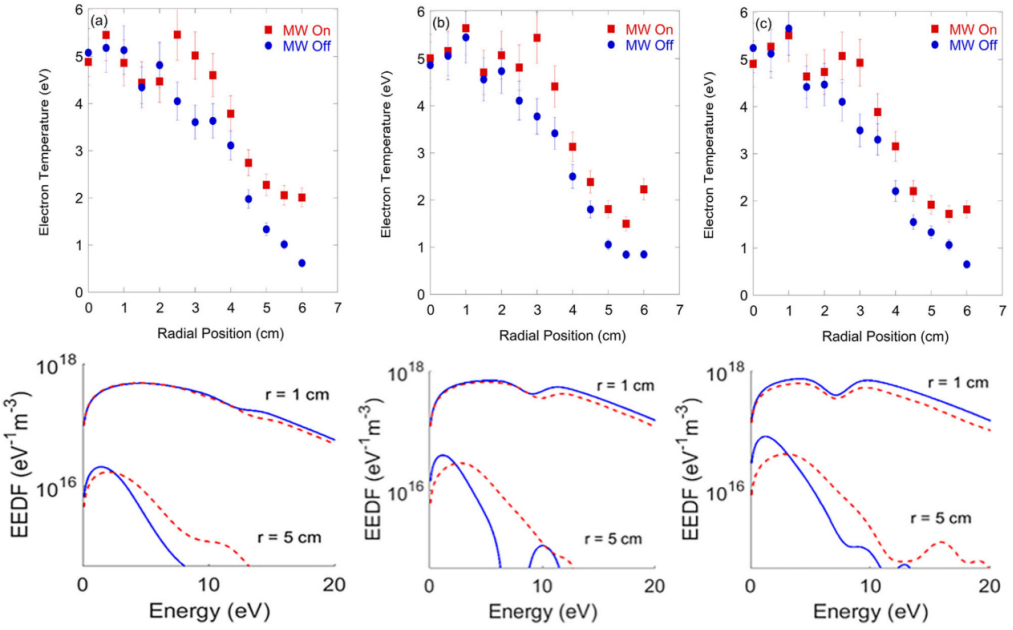

FIGURE 5.7: Helium electron temperature (from Langmuir probe measurements) versus radial location for three different RF powers (a) 250 W, (b) 450 W, and (c) 650 W with (red squares) and without (blue circles) microwaves. Below each radial profile, the electron energy distribution function (EEDF) obtained from a Druyvesteyn analysis for the same RF powers with (red dashed lines) and without (blue solid lines) microwaves is shown for two different radial positions. The electron heating is well outside of the 10% error bars shown.

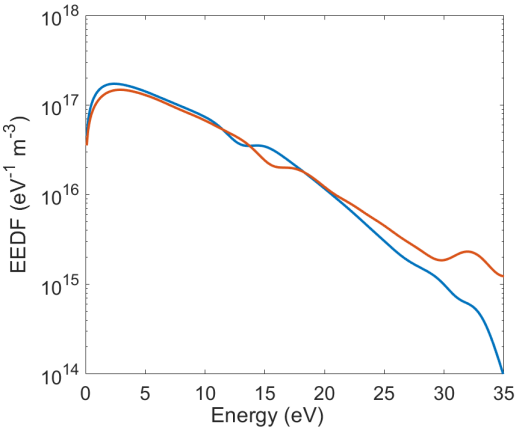

FIGURE 5.8: The EEDF at $r = 3$ cm for an RF power of 650 W with (red) and without (blue) microwave injection. The high energy portion of the EEDF exhibits significant enhancement with the addition of the microwaves.

RF power of 650 W is shown in Fig. 5.8 with and without microwaves. The electron temperature in this helium plasma jumps nearly 1.5 eV with the addition of the X-wave microwaves. The amplitude of the EEDF for all energies above 20 eV increases significantly when the microwaves are injected. By 35 eV, the increase in EEDF amplitude is nearly an order of magnitude. The

X-mode microwaves clearly enhance the energetic electron population at the location of the upper hybrid resonance.

OES measurements of helium ion emission paint a similar picture of the effects of microwave injection. Shown in Fig. 5.9 is the emission spectrum around 468.6 nm and 656.0 nm for an RF power of 250 Watts, a neutral pressure of 20 mTorr, and without microwave injection. Also shown is the emission spectrum for the same RF power and for two different operating pressures (20 mTorr and 7 mTorr) with injection of microwaves. The 656.0 nm transition arises from decay of the $n = 6$ level of the helium ion to the $n = 4$ level whereas the 468.6 nm line arises from decay of the $n = 4$ level to the $n = 3$ level. For both transitions the OES measurements show no evidence of emission without microwave injection and clear evidence of emission with microwave injection. The increase in emission is much greater for the 7 mTorr case compared to the 20 mTorr case. The observed increase in helium ion emission for these X-wave injection experiments was much larger than what was observed in the earlier R-wave injection studies.[71] We note that the strong line at 656.3 nm is a hydrogen line due to residual water in the system.

The Langmuir probe and OES measurements both confirm coupling of microwave power into the electrons and the Langmuir probe measurements localize the heating to roughly $r = 2.5$ cm, exactly where the upper hybrid resonance is expected for these plasma conditions.

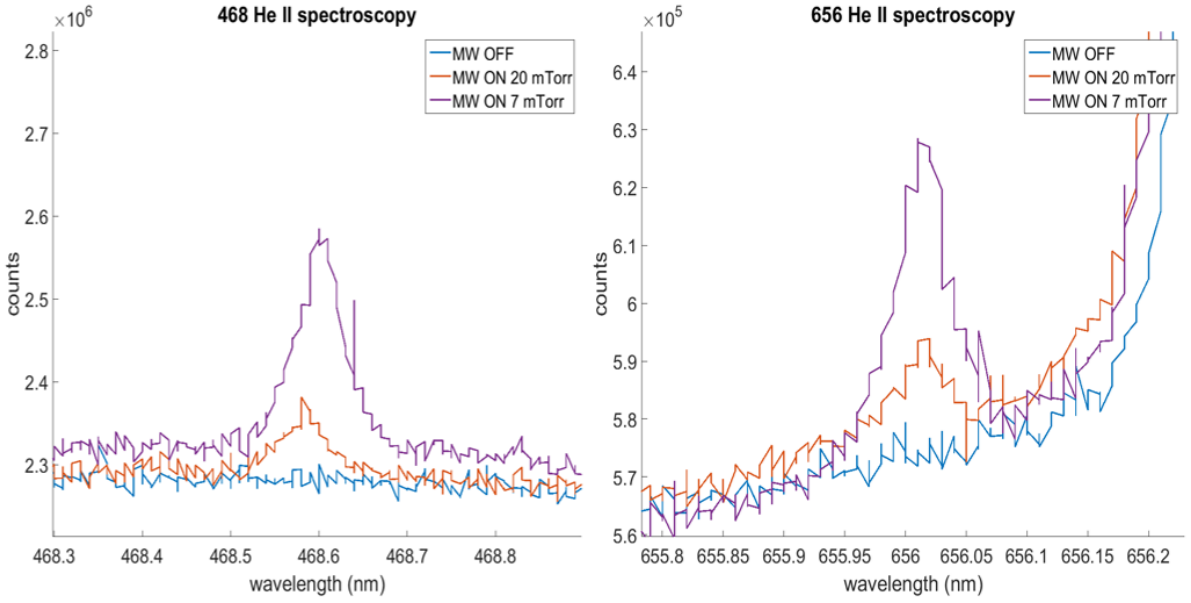

FIGURE 5.9: (a) Emission around the 468 nm He II transition for two different pressures (20 mTorr and 7 mTorr) with microwaves and without (blue line). (b) Emission around the 656 nm He II transition for two different pressures (20 mTorr and 7 mTorr) with microwaves and without (blue line). The magnetic field strength was 850 G and the RF power was 250 kW. The operating pressure was 20 mTorr for the no microwave case.

Chapter 6

Discussion and Future Work

6.1 Discussion of R-wave Injection Studies

With R-wave injection, enhancement of the population of excited ion states was achieved in both argon and helium gases. In argon, the high energy electrons (>15 eV) were observed to increase in number and temperature until the temperature of the tail matched the temperature of the bulk. This was due specifically to microwave energy deposition in the tail at the ECR condition, and was not replicated through other RF heating mechanisms when the RF power was adjusted. The replenishing of the high energy tail of the EEDF was only observed when the ECR condition was achieved somewhere in the system, not just when the microwaves were on. Ion emission lines were also observed to increase in strength when microwaves were injected, indicating an increase in excited state populations.

In helium, the observation of ion emission with the application of microwaves indicated the presence of populated excited helium ion states necessary for novel laser-induced fluorescence techniques. The population of these states is through electron impact excitation. The high energy electrons were created through direct energy input into the EEDF tail via microwaves.

This effect is not observed when RF power was increased within the limits of the power supply. Again, the ECR condition was necessary for sufficiently populating the high energy tail of the EEDF.

6.2 Discussion of X-wave Injection Studies

The X-wave injection studies demonstrated spatially localized heating of electrons at the upper hybrid resonance in helium helicon plasmas. No heating was observed in argon helicon plasmas, as expected given the lack of an upper hybrid resonance in argon plasmas for a microwave frequency of 2.45 GHz. Because the long-term objective of these experiments is to enhance the fraction of helium ions in the very energetic (40.8 eV above the ground state) metastable $2s$ state, it is important to consider the impact of the increased electron temperature on the population of $2s$ state. As shown in Fig. 5.9, the gain in electron energy due to the microwave injection is clearly sufficient to drive helium ions into the $n = 6$ state, 52.9 eV above the ground state. Shown in Fig. 6.1 is the relative population, relative to the ground state density, of the $2s$ metastable state as a function of electron temperature for four different plasma densities. The curves shown in Fig. 6.1 are again from on a collisional radiative model of helium that uses the rate coefficients for helium neutral and helium ion transitions from the ADAS suite of codes. Based on the model shown in Fig. 6.1, the observed 3.5 to 5.0 eV change in electron temperature in the 650 W helium plasma at $r = 3$ cm should result in at least a twenty fold increase in the helium $2s$ metastable ion population. With such a change in excited state population, it may then be possible to deploy LIF and TALIF techniques in helium helicon plasmas for direct measurements of the helium ion velocity distribution function. Note that it is possible that microwave injection has the potential to alter the original ion velocity distribution

through collisional heating of the ions by hotter electrons, an effect that should be considered if this technique proves successful in creating the appropriate metastable population for TALIF.

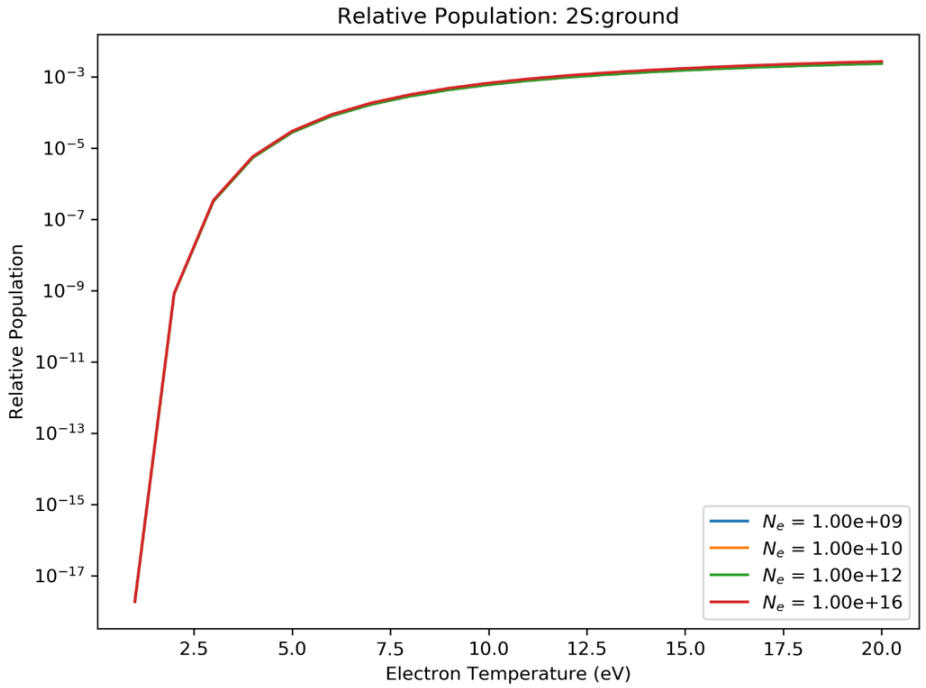

FIGURE 6.1: The predicted population in the 2S state of He II relative to the ground state as a function of electron temperature for four different electron densities. The predicted ratio is insensitive to density over seven orders of magnitude.

6.3 Future Work

Over the past decade, helium ion TALIF experiments at West Virginia University have been unsuccessful. No detectable TALIF emission has ever been observed. A possible explanation could come from a combination of the atomic physics and the sensitivity threshold of the TALIF diagnostic. In work by *Galante*[72], hydrogen TALIF measurements had a calculated minimum resolvable density of 10^{13} cm^{-3}. In these experiments, the helium ion density is of the order 10^{12} cm^{-3} or less and the electron temperature is less than 10 eV. Given this ion density and electron tempeature, the fraction of helium ions in the 2s metastable state relative to the ground

state is on the order of 10^{-3}. This means, the available helium ions excited will at most be one thousandth of the ground state density (Fig.6.1). Furthermore, even if every ion in the population fraction of the $2s$ metastable state were to be pumped to the $n = 6$ level, what fraction of those would decay to $n = 4$? Using the Einstein A coefficients provided by the NIST Atomic Spectra Database[73] the probability of decay between two atomic levels is calculable. Table 6.1 lists the likelihood of the possible decay paths for every l state out of the $n = 6$ level. As TALIF is a two-photon absorption process, selection rules dictate an electron pumped from the $2s$ state must go a $6s$ or a $6d$ state which can then decay to the $4p$ state or, in the case of the $6d$ state, also the $4f$ state. From the table, the $6d \rightarrow 4p$ transition will occur 9.5% of the time while the $6d \rightarrow 4f$ transition will occur 0.21% of the time.

TABLE 6.1: Decay probabilities from He II $n = 6$ atomic levels

Initial State	**Final State**	**Likelihood of Decay**
6s	5p	13.83%
6s	4p	19.29%
6s	3p	27.31%
6s	2p	39.57%
6p	5s	0.99%
6p	5d	0.39%
6p	4s	1.82%
6p	4d	0.33%
6p	3s	3.9%
6p	3d	3.2%
6p	2s	11.67%

6p	1s	80.57%
6d	5p	5.4%
6d	5f	0.47%
6d	4p	9.5%
6d	4f	0.21%
6d	3p	22.55%
6d	2p	61.82%
6f	5d	17.35%
6f	5g	0.27%
6f	4d	30.88%
6f	3d	51.49%
6g	5f	44.61%
6g	5f	55.39%
6h	5g	100%

So, to achieve a measurable signal the He ion density must be at least 10^4 times larger than the TALIF measurement's lower resolution limit. Fig. 5.3 shows that increasing He ion density shifts the damping regions for the X-wave outward towards the chamber edge. Not only would the high density needed to achieve TALIF signal push these damping regions outside of the chamber, they are beyond the capabilities of CHEWIE or most helicon source experiments. Using the most likely decay transition of $6d \rightarrow 2p$ with a wavelength 102.5 nm only increases the population of emitting ions by a factor of six. Therefore, for ECR heating to provide a

means of creating a target population of helium ions for TALIF studies, the overall ion density of helium plasmas in a helicon source must be increased significantly.

Bibliography

[1]M. A. Lindon and E. E. Scime, "Co2 dissociation using the versatile atmospheric dielectric barrier discharge experiment (vader)", Frontiers in Physics **2** (2014) 10.3389/fphy.2014.00055.

[2]T. Gans, J Schulze, D Oconnell, U Czarnetzki, R Faulkner, A. Ellingboe, and M. Turner, "Frequency coupling in dual frequency capacitively coupled radio-frequency plasmas", Applied physics letters **89**, 261502 (2006).

[3]J Schulze, E Schüngel, U Czarnetzki, and Z Donkó, "Optimization of the electrical asymmetry effect in dual-frequency capacitively coupled radio frequency discharges: experiment, simulation, and model", Journal of Applied Physics **106**, 063307 (2009).

[4]E Schüngel, J Schulze, Z Donkó, and U Czarnetzki, "Power absorption in electrically asymmetric dual frequency capacitive radio frequency discharges", Physics of Plasmas **18**, 013503 (2011).

[5]B. Sahu and J. G. Han, "Electron heating mode transition induced by mixing radio frequency and ultrahigh frequency dual frequency powers in capacitive discharges", Physics of Plasmas **23**, 053514 (2016).

[6]M. Lee, H. Lee, and C. Chung, "Observation of collisionless heating of low energy electrons in low pressure inductively coupled argon plasmas", App. Phys. Lett. **93**, 231503 (2008).

[7]H. Lee and C. Chung, "Control of electron energy distribution by adding a pulse inductive field in capacitive discharge", Plasma Sources Science and Technology **23**, 062002 (2014).

[8]N. J. Fisch, "Theory of current drive in plasmas", *Reviews of Modern Physics* **59**, 175 (1987).

[9]R. Boswell, "Very efficient plasma generation by whistler waves near the lower hybrid frequency", Plasma Physics and Controlled Fusion **26**, 1147 (1984).

[10]M. Balkey, R Boivin, J. Kline, and E. Scime, "Ion heating and density production in helicon sources near the lower hybrid frequency", Plasma Sources Science and Technology **10**, 284 (2001).

[11]R. Chen and N. Hershkowitz, "Multiple electron beams generated by a helicon plasma discharge", Phys. Rev. Lett. **80**, 4677–4680 (1998).

[12]J. Kline, E. Scime, R. Boivin, A. Keesee, X Sun, and V. Mikhailenko, "Rf absorption and ion heating in helicon sources", Physical review letters **88**, 195002 (2002).

[13]E. Aguirre, E. Scime, D. Thompson, and T. Good, "Spatial structure of ion beams in an expanding plasma", Physics of Plasmas **24**, 123510 (2017).

[14]E. M. Aguirre, R. Bodin, N. Yin, T. N. Good, and E. E. Scime, "Evidence for electron energization accompanying spontaneous formation of ion acceleration regions in expanding plasmas", Physics of Plasmas **27**, 123501 (2020).

[15]E. J. Spence, K. Reuter, and C. B. Forest, "A spherical dynamo experiment", The AstroPhys. Journal **700**, 470–478 (2009).

[16]I. Biloiu and E. Scime, "Ion acceleration in ar–xe and ar–he plasmas. ii. ion velocity distribution functions", Physics of Plasmas **17**, 113509 (2010).

[17]I. Furno, T. Intrator, E. Torbert, C. Carey, M. D. Cash, J. K. Campbell, W. J. Fienup, C. A. Werley, G. A. Wurden, and G. Fiksel, "Reconnection scaling experiment: a new device for three-dimensional magnetic reconnection studies", Rev. Sci. Instrum. **74**, 2324–2331 (2003).

[18]S. Houshmandyar and E. E. Scime, "Ducted kinetic alfvn waves in plasma with steep density gradients", Phys. Plasmas **18**, 112111 (2011).

[19]J Winter, J. S. Sousa, N Sadeghi, A Schmidt-Bleker, S Reuter, and V Puech, "The spatio-temporal distribution of he (23s1) metastable atoms in a mhz-driven helium plasma jet is influenced by the oxygen/nitrogen ratio of the surrounding atmosphere", *Plasma Sources Sci. Technol.* **24**, 025015 (2015).

[20]E. E. Scime, P. A. Keiter, M. M. Balkey, J. L. Kline, X Sun, A. M. Keesee, R. A. Hardin, I. Biloiu, S Houshmandyar, S. C. Thakur, et al., "The hot helicon experiment (helix) and the large experiment on instabilities and anisotropy (leia)", Journal of Plasma Physics **81** (2015) 10.1017/S0022377814000890.

[21]I. Biloiu and E. Scime, "Temporal evolution of double layers in pulsed helicon plasmas", Applied Physics Letters **95**, 051504 (2009).

[22]M. Galante, R. Magee, and E. Scime, "Two photon absorption laser induced fluorescence measurements of neutral density in a helicon plasma", Physics of Plasmas **21**, 055704 (2014).

[23]D. W. McCarrin, "Continuous wave ring-down spectroscopy for velocity distribution measurements in plasma", PhD thesis (West Virginia University).

[24]S. C. Thakur, "Understanding plasmas through ion velocity distribution function measurements", PhD thesis (West Virginia University).

[25]F. F. Chen, *UCLA Internal Report*, PPG–1401 (1992).

[26]L. E. Feher, *Energy efficient microwave systems: materials processing technologies for avionic, mobility, and environmental applications* (Springer-Verlag, Berlin, 2009).

[27]L. E. Feher, *Microwave engineering* (John Wiley Sons Inc, Hoboken, 2012).

[28]H. M. Mott-Smith and I. Langmuir, "The theory of collectors in gaseous discharges", Physical review **28**, 727 (1926).

[29]A. M. Keesee, "Neutral density profiles in argon helicon plasmas", PhD thesis (West Virginia University).

[30]P. A. Keiter, "Experimental investigation of ion temperature anisotropy driven instabilities in a high beta plasma", PhD thesis (West Virginia University).

[31]Y. Yardley and C. B. Moore, "Laserexcited vibrational fluorescence and energy transfer in methane", *Journal of Chemical Physics* **45**, 1066 (1966).

[32]R. A. Stern and J. A. Johnson, "Plasma ion diagnostics using resonant fluorescence", *Phys. Rev. Lett.* **34**, 1548 (1975).

[33]H. C. Meng and H. J. Kunze, "Investigation of the diffusion of impurity atoms in plasmas by laser fluorescence", *Phys. Fluids* **22**, 1082–1088 (1979).

[34]D. N. Hill, S. Fornaca, and M. G. Wikham, "Single frequency scanning laser as a plasma diagnostic", *Rev. Sci. Instrum.* **54**, 309–314 (1983).

[35]J. Carr Jr., "Laser induced fluorescence studies of electrostatic double layers in an expanding helicon plasma", PhD thesis (West Virginia University).

[36]J. L. Kline, "Slow wave ion heating and parametric instabilities in the helix helicon source", PhD thesis (West Virginia University).

[37]G. D. Severn, D. A. Edrich, and R. McWilliams, "Argon ion laser-induced fluorescence with diode lasers", *Rev. Sci. Instrum.* **69**, 10–15 (1998).

[38]R. F. Boivin and E. E. Scime, *Rev. Sci. Instrum.* **74**, 4352–4360 (2003).

[39]R. F. Boivin, *Study of the different line broadening mechanisms for the laser induced fluorescence diagnostic of the helix and leia plasmas*, tech. rep. 39 (West Virginia University, 1998).

[40]M. J. Goeckner, J. Goree, and T. E. Sheridan, "Measurements of ion velocity and density in the plasma sheath", *Phys. Fluids B* **4**, 1663–1670 (1992).

[41]H. N, "How langmuir probes work", in *Plasma diagnostics: discharge parameters and chemistry, volume 1*, edited by D. L. F. Orlando Auciello (Academic Press, Inc., Boston, 1989) Chap. 3.

[42]F. F. Chen, "Langmuir probe diagnostics", in Mini-course on plasma diagnostics, ieeeicops meeting, jeju, korea (2003), pp. 20–111.

[43]F. F. Chen, "Langmuir probes in rf plasma: surprising validity of oml theory", Plasma Sources Science and Technology **18**, 035012 (2009).

[44]F. F. Chen, J. D. Evans, and D. Arnush, "A floating potential method for measuring ion density", Physics of Plasmas **9**, 1449–1455 (2002).

[45]S. Houshmandyar and E. E. Scime, "Ducted kinetic alfvén waves in plasma with steep density gradients", *Phys. Plasmas* **18**, 112111 (2011).

[46]V. Godyak and V. Demidov, "Probe measurements of electron-energy distributions in plasmas: what can we measure and how can we achieve reliable results?", Journal of Physics D: Applied Physics **44**, 233001 (2011).

[47]V. Demidov, S. V. Ratynskaia, and K Rypdal, "Electric probes for plasmas: the link between theory and instrument", Review of scientific instruments **73**, 3409–3439 (2002).

[48]V. Godyak and B. Alexandrovich, "Comparative analyses of plasma probe diagnostics techniques", Journal of Applied Physics **118**, 233302 (2015).

[49]V. Godyak and B. Alexandrovich, "Langmuir paradox revisited", Plasma Sources Science and Technology **24**, 052001 (2015).

[50]M. A. Liebermann and A. J. Lichtenberg, *Principles of plasma discharges and materials processing* (Wiley, Hoboken NJ, 2005).

[51]C. J. Foot, *Atomic physics* (Oxford University Press, New York, 2005).

[52]*Operating manual for stf-8300 series cameras* ().

[53]M OMullane, "Background to adas", in Adas course at iter, 13 december 2010 (2009 [Online].).

[54]R. Boivin, J. Kline, and E. Scime, "Electron temperature measurement by a helium line intensity ratio method in helicon plasmas", Physics of Plasmas **8**, 5303–5314 (2001).

[55]N. I. Arnold, "An investigation into the role of metastable states on excited populations of weakly ionized argon plasmas, with applications for optical diagnostics", PhD thesis (Auburn University).

[56]*Instruction manuel model 209 scanning monochromator* ().

[57]*Model 209 czerny-turner monochromator for high resolution spectroscopy*, https://mcphersoninc.com/dwg/209dwg.png.

[58]T. H. Stix, *Waves in plasmas* (AIP, New York, 1992).

[59]K. G. Budden, *Radio waves in the ionosphere* (Cambridge University Press, New York, 1961).

[60]D. G. Swanson, *Plasma waves* (IOPP, Philadelphia, 2003).

[61]C. Charles and R. Boswell, *Appl. Phys. Lett.* **82**, 1356–1358 (2003).

[62]F. F. Chen, "Helicon discharges and sources: a review", *Plasma Sources Sci. Technol.* **24**, 014001 (2015).

[63]A. I. Strini, G. N. Malovi, Z. L. Petrovi, and N Sadeghi, "Electron excitation coefficients and cross sections for excited levels of argon and xenon ions", *Plasma Sources Sci. Technol.* **13**, 333 (2004).

[64]J. Boffard, G. A. Piech, M. F. Gehrke, L. W. Anderson, and C. C. Lin, *Phys. Rev. A* **59**, 2749 (1999).

[65]A. M. Keesee, E. E. Scime, and R. F. Boivin, "Laser-induced fluorescence measurements of three plasma species with a tunable diode laser", *Ref. Sci. Instrum.* **75**, 4091–4093 (2004).

[66]R. M. Magee, M. E. Galante, J. Carr, G. Lusk, D. W. McCarren, and E. E. Scime, "Neutral depletion and the helicon density limit", *Phys. Plasmas* **20**, 123511 (2013).

[67]D. F. Dance, M. F. A. Harrison, and A. C. H. Smith, "A measurement of the cross section for production of he+(2s) ions by electron impact excitation of ground state helium ions", *Proc. R. Soc. Lond. A* **290**, 7493 (1966).

[68]A. A. Sorokin, I. L. Beigman, S. V. Bobashev, M. Richter, and L. A. Vainshtein, "Total electron-impact ionization cross sections of helium", *J. Phys. B: At. Mol. Opt. Phys.* **37**, 3215 (2004).

[69]J. Zalach, O. Grulke, and T. Klinger, "Ecr heating in a helicon device", in Aip conference proceedings, Vol. 812, 1 (American Institute of Physics, 2006), pp. 219–222.

[70]H. Summers, M. OMullane, A. Whiteford, N. Badnell, and S. Loch, "Adas: atomic data, modelling and analysis for fusion", in Aip conference proceedings, Vol. 901, 1 (American Institute of Physics, 2007), pp. 239–248.

[71]M. U. Siddiqui, J. S. McKee, J. McIlvain, Z. D. Short, D. B. Elliott, G. Lusk, and E. E. Scime, "Electron heating and density production in microwave-assisted helicon plasmas", Plasma Sources Science and Technology **24**, 034016 (2015).

[72]M. Galante, "Two-photon absorption laser induced fluorescence measurements of neutral density in helicon plasma", PhD thesis (West Virginia University).

[73]*Nist atomic spectra database lines form*, `https://physics.nist.gov/cgi-bin/ASD/lines,`.